universität
wien

# MASTERARBEIT / MASTER’S THESIS

Titel der Masterarbeit / Title of the Master‘s Thesis

## „MICROSCOPY BASED METHODS FOR STUDYING TUMOR-MICROBE INTERACTION IN MURINE COLON CANCER ALLOGRAFT TISSUE AND SPHEROIDS“

verfasst von / submitted by

Hanan Raheb

angestrebter akademischer Grad / in partial fulfilment of the requirements for the degree of

Magistra pharmaciae (Mag.pharm.)

Wien, 2020 / Vienna, 2020

| | |
|---|---|
| Studienkennzahl lt. Studienblatt / degree programme code as it appears on the student record sheet: | UA 066 605 |
| Studienrichtung lt. Studienblatt / degree programme as it appears on the student record sheet: | Masterstudium Pharmazie |
| Betreut von / Supervisor: | Uni. Prof. Dipl. Ing. Dr. Manfred Ogris |
| Mitbetreut von / Co-Supervisor: | Dr. Haider Sami |

# Acknowledgement

I would like to thank my supervisors, Dr. Prof. Manfred Ogris, who was more than generous with his expertise and for providing me the opportunity to work in the Laboratory of Macromolecular Cancer Therapeutics, and Dr. Haider Sami for his supervision and patient guidance.

A unique feeling of gratitude to my loving family; my father Naim Raheb, my mother Fahima Raheb, and my brothers Tony and Mina, I would have never been able to achieve anything without their indescribable love, care and for believing in my choices and supporting them. To my lovely cousin Bernadet Biruhs my supportive fiancé Jubran Dahdal, to Adrijana Sarenac, Tini Le and many other friends, I’ll never forget your support.

# Abbreviations

ROS Reactive oxygen species

ABCB1 ATP binding cassette subfamily B member 1

MDR Multidrug resistance

MCTS Multicellular Tumor Spheroids

FACS Fluorescence activated cell sorting

CLSM Confocal Laser Scanning Microscopy

IBD Inflammatory Bowel Disease

SM Supernatant Metabolites

CVD Cardiovascular Disease

DSB Double Strands Breaks

HBV Hepatitis B Virus

HCV Hepatitis C Virus

HPV Human Papillomavirus

EBV Epstein-Barr Virus

CRISPRi CRISPR interference

PPS Periplasmic Space

APCs Antigen presenting cells

IM Inner membrane

GFP Green fluorescent protein

VCGs V. cholerae Ghosts

EGFP Enhanced green fluorescent protein

PCR Polymerase chain reaction

MHC-II Major histocompatibility complex class II

CRC Composite complete remission

CRC Colorectal carcinoma

ICD Immunogenic cell death

ATP Adenosine Triphosphate

HMGB1 High-Mobility-Group-Protein B1

CRT Calreticulin

# Table of content

**Abstract** ........................................................................................................ 1

**Zusammenfassung** ........................................................................................... 2

**Introduction** ...................................................................................................... 3

Bacterial Ghosts ....................................................................................................... 3

Bacterial vectors in cancer gene therapy ........................................................ 4

Production of bacterial ghosts ........................................................................ 4

Pharmaceutical applications of bacterial ghosts ............................................. 5

Features, challenges and future applications of bacterial ghosts .................. 11

Archaea .................................................................................................................... 12

Gut microbiota and host's cancer relationship ............................................. 12

Role of gut microbiota in cancer treatment ................................................... 13

Archaea in human gut ..................................................................................... 15

Tumor-targeted drug delivery system and the complexity of tumor microenvironment . 24

Multicellular tumor spheroids (MCTS) ......................................................... 25

**Aim of Thesis** .................................................................................................. 34

**Materials and Methods** .................................................................................. 35

Bacterial Ghosts' biodistribution ......................................................................... 35

Archaea infiltration ............................................................................................... 44

**Results and Discussions** ................................................................................. 55

**References** ....................................................................................................... 95

# Abstract

This work is based on employing fluorescence microscopy (FLM) for studying the distribution of fluorescently labeled microbes within colorectal cancer models based on the murine cell line CT26.The first project investigates the biodistribution of bacterial ghosts (BGs) in CT26 tumor bearing mice, while the second one studies the infiltration of archaea within CT26 derived multicellular tumor spheroids (MCTS). Both, organs from CT26 tumor bearing mice and spheroids derived from CT26 cells, were cryo-sectioned and imaged for the desired fluorescence.

The first part of this thesis presents bacterial ghosts' project, where BGs were labeled with AF750 dye and detected by near infrared fluorescence emission and also by immunostaining for ice nucleation protein (INP). Out of the organs harvested from CT26 tumor bearing mice (2 hours after injecting AF750-BGs), pancreas and pancreatic tumor nodules were selected and cryo-sectioned, and were then subjected to FLM for detecting a) BGs via direct AF750 emission (Cy7 channel) and via the presence of INP (FITC channel) and b) tumor cells via DAPI emission. The association of BGs with tumor cells had been imaged and investigated through three imaging aims: 1. Overlap between AF750 and INP emission at different magnifications; 2. ability to observe the AF750-BGs through Cy7 filter at 10X magnification and exposure time between 1.5-2 s; 3. imaging the intact BGs at 60X magnification.

Similarly, the second part of thesis employed fluorescence microscopy techniques to observe archaea infiltration in CT26-based 3D MCTS. These spheroids were inoculated with the nonpathogenic, strictly anaerobic archaea, *Methanococcus maripaludis* S0001, and the localization of archaea was tracked at three timepoints after inoculation, i.e.; 24, 120 and 168 hours, in order to observe if they are able to infiltrate into the tumor spheroids. Fluorescent imaging for the DAPI stained spheroids' cryosections illustrated the localization of archaea labeled with the dye AF488 (emission in the FITC channel) on the surface of spheroids inoculated with archaea for 24h, and the tendency of this microbe to move toward the center after 120 hours of inoculating the spheroids. Finally, DAPI and FITC merged channels for the cryosections of spheroids inoculated with "AF488 labeled" archaea for 168 hours could proof the localization of anaerobic archaea near and within the hypoxic areas of these spheroids, which could predict in turn the selectivity of these microorganisms for *in vivo* targeting the hypoxic centers of cancerous tissues.

# Zusammenfassung

Diese Arbeit basiert auf dem Einsatz der Fluoreszenzmikroskopie (FLM) zur Untersuchung der Verteilung fluoreszenzmarkierter Mikroben in Darmkrebsmodellen auf der Basis der murinen Tumorzelllinie CT26. Das erste Projekt untersucht die Bioverteilung von leeren Bakterienhüllen (Bacterial Ghosts, BGs) in CT26-tumortragenden Mäusen, während das zweite Projekt die Infiltration von Archaeen in aus CT26 Zellen gebildeten mehrzelligen Tumorsphäroiden (MCTS) untersucht. Sowohl von den Organen der CT26-tumortragenden Mäuse als auch von den CT26-Sphäroiden wurden Gefrierschnitte angefertigt und die entsprechenden Fluoreszenzsignale abgebildet.

Der erste Teil dieser Arbeit stellt das Projekt der BGs vor, bei dem diese mit dem Nahe-infrarot Fluoreszenzfarbstoff AF750 kovalent markiert sind und durch Fluoreszenzemission im nahen Infrarotbereich sowie durch Immunfärbung gegen das Eisnukleationsprotein (INP) nachgewiesen wurden. Von den Organen, die den CT26-tumortragenden Mäusen (2 Stunden nach Injektion von AF750-BGs) entnommen wurden, wurde der Pankreas und im CT26 Tumorlesionen im Pankreas ausgewählt und davon Gefrierschnitte angefertigt. Diese wurden dann einer FLM unterzogen, um a) die BGs über die AF750-Emission (Cy7-Kanal) und über das INP (FITC-Kanal, nach Immunfluoreszenzfärbung mit den Fluoreszenzfarbstoff AF488) nachzuweisen und b) die Tumorzellen über DAPI-Emission nachzuweisen. Die Assoziation der BGs mit den Tumorzellen wurde anhand von drei Bildgebungszielen untersucht und dargestellt: 1. Überlappung der AF750- und AF488-Emission bei unterschiedlichen Vergrößerungen, 2. Möglichkeit der Betrachtung der AF750-BGs durch den Cy7-Filter bei 10-facher Vergrößerung und einer Belichtungszeit zwischen 1,5 und 2 Sekunden und 3. Abbildung der intakten BGs bei 60-facher Vergrößerung.

Im zweiten Teil der Arbeit wurden auf ähnliche Weise fluoreszenzmikroskopische Techniken eingesetzt, um die Infiltration von Archaeen in 3D-MCTS auf CT26-Basis zu beobachten. Diese Sphäroide wurden mit nicht pathogenen, streng anaeroben Archaea des Stammes *Methanococcus maripaludis* S0001 beimpft. Die Lokalisation der Archaea wurde zu drei Zeitpunkten (24, 120 und 168 Stunden) verfolgt, um zu beobachten, ob die Archaea in die Tumorsphäroide eindringen können. Die Fluoreszenzbilder der DAPI-gefärbten Gefrierschnitte der Sphäroide veranschaulichen die Lokalisierung der AF488-markierten Archaeen auf der Oberfläche von Sphäroiden, die 24 Stunden lang mit Archaeen kultiviert wurden, und die Tendenz dieser Mikrobe, sich nach 120-stündiger Kultivierung in Richtung Zentrum des Sphäroids zu bewegen. Schließlich erbrachten die überlagerten Messkanäle DAPI und FITC der Gefrierschnitte der Sphäroide, die 168 Stunden lang mit AF488-markierten Archaeen kultiviert worden waren, den Nachweis für die Lokalisierung anaerober Archaeen nahe und innerhalb der hypoxischen Bereiche dieser Sphäroide, was wiederum die Selektivität dieser Mikroorganismen voraussagt auch *in vivo* auf die hypoxischen Zentren von Krebsgewebe abzuzielen.

# Introduction

## 1. Bacterial Ghosts

Two of the most critical challenges in the pharmaceutical domain are drug targeting and drug delivery. By developing bacterial ghosts, scientists have created an effective drug delivery platform for many pharmaceuticals, as well as, for antigens, proteins, vaccines and nucleic acids. For example, modern vaccination using recombinant proteins or DNA is facing a lot of problems such as the poor immunogenicity and the absence of proper response, because of the degradation of these compounds through many components of biological fluids. Although synthetic drugs could overcome this problem, the diverse distribution of synthetic pharmaceuticals in the body could lower the maintained sufficient concentration at the targeted organ, therefore it is increasingly important to develop such an effective carrier system which is able to efficiently deliver these compounds with reduced yet effective and safe dose (Sesardic & Dobbelaer, 2004).

The inactivated whole bacteria or live attenuated bacterial cells are contributed as useful carriers for biological and pharmaceutical compounds (Kang & Curtiss, 2003). Bacterial ghosts which are considered as non-denatured, empty gram-negative bacteria, generated by protein-E-mediated cell lysis, still retain the principal structural, morphological, and immunogenic properties on their intact envelopes which still have the bio-adhesive characters that make them interact with the host cells and make them ideal carriers to deliver and protect immunogenic biologicals and synthetic pharmaceuticals (Huter et al., 1999; Witte et al, 1990).

The reasons that make some ghosts candidates, such as *Pasteurella haemolyrica*, *Salmonella enteritidis*, *Vibrio cholera* and *Helicobacter pylori*, special drug delivery carriers and useful tools for immunization, are their immunogenic potential and ability to elicit specific cellular and humoral immune responses after the application of recombinant ghosts orally or parenterally (Medina & Guzman, 2001). BGs are classified to be nonliving carriers which protect, target and deliver proteins, vaccines, DNA and pharmaceuticals, furthermore, they have also the ability to be recognized und effectively uptaken by antigen presenting cells APCs, such as dendritic cells and macrophages, which increases their selectivity in drug delivering (Tabrizi et al., 2004).

### 1.1. Bacterial vectors in cancer gene therapy

Because of the complex pathology of cancer, it is important to combine different therapeutics in order to achieve synergistic and desirable effects. An example on that, is combining the clinically approved chemotherapy, radiation therapy, and thermal radiofrequency with oncolytic bacteria and other preclinically examined strategies that potentiate the hypoxic level of tumor environment, in order potentiate both bacterial attraction toward these tissues, and bacterial colonization. However, targeting and optimizing the delivery of these bacteria as live delivery systems beside the limitation of serious adverse effects are critical challenges while introducing the recombinant bacteria into human body. Furthermore, scientific strategies should be planned in order to limit both lateral, unfavorable gene transfer to other bacterial populations and also the biological contamination. Limiting the environmental spread of these vectors could be achievable by engineering these vectors in a way that allows their survival inside the host, depending on specific nutrients which are limited in the external environment (Tangney & Gahan, 2010).

Another advantages in using live bacterial vectors in gene therapy are the practical and low cost of their manufacturing in comparison with viral vectors, as well as, the post-administration safety, because of their sensitivity to the clinically approved antibiotics. The positive clinical outcomes from developing live bacterial vectors for the purpose of drug targeting and delivering, increases their acceptance by clinicians, researchers, and sponsor. However, the safety of these therapeutics must always be considered, besides the infrastructure, expertise and the costs required in manufacturing liposomes, cationic polymers and other chemical vectors in comparison to the traditional naked DNA plasmid (Li et al., 2008).

### 1.2. Production of bacterial ghosts

Bacterial ghosts are produced from the lysis of gram-negative bacteria after the expression of bacteriophage’s PhiX174 cloned gene E, which encodes a membrane protein composed of 91 amino acids. This protein leads to the fusion of the inner and outer membrane of gram-negative bacteria and in turn to the `lysis` of these bacteria and thus expelling their cytoplasmic contents. This production process could be done in different experimental conditions. For example, by mutating EpR promoter/operator site, and insuring a stable E gene expression which could be achieved at a temperature of 37°C (Jechlinger, Szostak & Lubitz, 1998).

Generating bacterial ghosts using the general lysis of microbes is considered to be the easiest way in preparing an `intact` cellular envelope, without altering its physical and chemical properties. This achieved by protein E expression and association with the IM of the bacteria, followed by protein's conformational changes and oligomerization, which cause altering the location of its C-terminal domain from the cytoplasm into the PPS, and in turn, to the development of a `transmembrane tunnel structure` between the outer and the inner membrane prior to the E-mediated lysis of gram-negative bacteria. The difference in osmotic pressure between the cytoplasm and the surrounding environment leads to the expulsion of protoplasm in to the surrounding environment, and formation of BGs with an intact and rigid peptidoglycan (Witte, Wanner & Lubitz, 1998; Schön et al., 1995).

The production of bacterial ghosts is relatively fast, and the whole process takes around one day. The produced BGs pretend exactly like a living bacteria, because of the same basic organizational cell structure including the membrane surface proteins, pili and adhesins. They are generated using batch fermentation process followed by deactivating the residual DNA, after that the whole cytoplasmic material is released, by treatment with β-propiolactone or Staphylococcal nuclease A (Szostak et al., 1997).

### 1.3. Pharmaceutical applications of Bacterial ghosts

Due to the non-pathogenic properties of intestinal microbiota and their growing pharmaceutical application as probiotics, these bacteria were designed to be live vectors that help inhibiting tumor growth after delivering and promoting the expression of therapeutic genes. Bifidobacteria are example on intestinal microbiota, which could be used for this purpose as they are obligate anaerobic bacteria. The only obstacle that restricted the number of the bifidobacteria strains used as delivery vectors is the resistance of these bacteria to genetic modifications (Hu et al., 2009). In order to overcome this problem, another sorts of gram-positive bacteria were implemented in tumor targeting studies, such as the spore-forming, strictly anaerobic bacteria, *Clostridium sporogenes*. Because of their restricted and incomplete oncolytic effect in the hypoxic centers of large tumors and the high death rate of experimental animals, these strains were attenuated or had been substituted with the non-pathogenic ones (Van Mellaert, Barbé & Anné, 2006; Wei et al., 2008).

Another strategy in overriding the pathogenicity of *Clostridium sporogenes* is substituting the usage of the whole bacterium, as gene delivery vector, with only the spores of these bacteria, which are immunologically inert and germinates selectively in tumor and vegetative tissues. The safety of intravenous administration of *Clostridium novyi-NT* spores had been tested in phase I clinical trial. The percentage of tumor regression and recurrence were also detected in another experiments on animal models (Diaz et al., 2005).

Further studies of genetic manipulations were done on different anaerobic bacterial species to improve the selectivity, localization, and survival of these strains in hypoxic tumor tissues and not the healthy, more oxygenated ones, and also to generate recombinant strains of lower violence and pathogenicity.

### 1.3.1. Bacterial ghosts and drug delivery

Through targeting *Actinobacillus* ghosts toward APCs, such as macrophages and dendritic cells, and after the internalization and processing of BGs, T cell-specific immune response against BGs antigens could be induced (Felnerova et al., 2004). These BGs could also be *in vitro* targeted toward macrophage mannose receptors, expressed on dermal microvascular endothelial cells (Gröger et al., 2000). Kudela et al (2011) concluded the possibility of using BGs as antigen and drug delivery carriers to cure ocular surface diseases, because of the possibility of targeting human conjunctival epithelial cells using BGs and their effective and safe internalization into corneal cells).

The ability of binding and phagocytosing BGs were investigated in different melanoma cell lines in Kudela et al (2008) experiment. The eight melanoma cell lines were able to bind and take up BGs derived from *Mannheimia haemolytica* as well as from *Escherichia coli.* Furthermore, 82% transfection efficiency were observed *in vitro* after measuring the level of GFP in Bowes cell transfected with BGs loaded with DNA.

Besides curing diseases, BGs could also be incorporated in cancer therapy to increase the selectivity and potentiate the effectiveness of anticancer therapeutics and also to reduce cytotoxic side effects. Loading doxorubicin, for example, on BGs derived from *Mannheimia haemolytica* and targeting them toward human colorectal adenocarcinoma cells had increased the antiproliferative effect in comparison to the treatment with doxorubicin alone, because of the efficient adherence of BGs on mammalian cells and the slow release of drug inside cancerous cells (Kudela, Koller & Lubitz, 2010).

### 1.3.2. Bacterial ghosts as carriers for proteins and peptides

Jechlinger et al (2005) proved the efficiency of *Escherichia coli* ghosts to be considered as an excellent antigen delivery system. After anchoring the hepatitis B virus (HBcAg-149) core 149 protein on the inner as well as the outer membrane of the empty Escherichia coli's envelope, a subcutaneous immunization on female BALB/c mice was done. As a result, a comparable immunogenic response in both models had been observed and the efficient BGs' immunogenic effect against foreign targeted antigens had been proved.

Reducing the morbidity and mortality rates caused by *V. cholerae* have been always a challenge. In order to achieve that, we need an effective broad-spectrum vaccine, rather than the current oral vaccine formulations, containing whole-cell cholera and toxoid, which demonstrate a transient protection. The adjuvant immunogenic properties from the orally administered *V. cholerae* ghosts, in different doses formulations, were tested in diarrhea models of reversible intestinal tie adult rabbits, and the results had showed the importance of VCGs in developing an effective vaccine delivery vehicle, because of the higher levels of serum vibriocidal titers compared to indicator strains and the mediated complement-dependent killing in the serum of *V. cholerae* ghosts- immunized rabbits, which was an evidence on the induced dose-dependent cross protection in inhibiting the colonization, which lasts for thirty days after primary immunization (Eko et al., 2003).

### 1.3.3. Bacterial ghosts as carriers for nucleic acids

Because of the demand for DNA delivery vehicles, which could effectively and safely mediate gene transfer and expression, Paukner et al (2005) presented BGs as a novel carrier for DNA targeting and delivering to macrophages. Linear, double-stranded DNA and plasmid DNA were loaded on *E. coli* ghosts (up to 6000 plasmids per single ghost) by suspending lyophilized BGs in DNA solution, followed by a washing step to remove DNA residues. The localization of the DNA to the inner lumen and not the outer surface of BGs were confirmed using immunocytochemical staining and flow cytometry, which detect the green fluorescence, and which had also shown the expression of EGFP by approximately 60% of the targeted and efficiently transfected murine macrophages.

In another study, Mayrhofer et al (2005) described a new technology to improve DNA vaccine efficiency, by immobilizing DNA plasmid (self-immobilizing plasmid) into the cytoplasmic membrane of BGs. During the production of BGs (during and after cell lysis) a specific protein/DNA interaction retains pSIP in the host envelope complex and the resulted BGs could be analyzed using real time PCR assays. Whereas using plasmids lacking this self-immobilization properties will failed to be incorporated in the cytoplasmic membrane of BGs and will be expelled in the culture broth, the thing which prove the importance of combining BGs technology with the plasmid immobilization procedure to produce a non-living, `self-loading` DNA carrier vehicle.

The transformation of dendritic cells (DCs) from immature state, in which they are only capable on capturing antigens, into specialized mature cells capable of stimulating T cells, requires variety of stimuli. The key step in this transformation process is the generalized activation of lysosomal function, which requires formation and accumulation of MHC-II (major histocompatibility complex class II) inefficiently from the internalized and slowly degraded antigens. However, efficient formation of MHC-II is mediated by enhancing lysosomal acidification and in turn antigen proteolysis which is mediated by activation of vacuolar proton pump. Trombetta et al (2003) approved the capacity of BGs loaded with specific antigens to target tumor cells and APCs and in turn inducing a selective immune response against these cells by activating CD4+ and CD8+ T cells.

### 1.3.4. Specific immunization using bacterial ghosts

Although modern medicine focuses always on developing advanced and effective recombinant proteins and DNAs as new-generation vaccines, these new vaccines are less immunogenic than the traditional ones, therefore it is important to develop an adjuvant to increase vaccines' immunogenicity. One of the potent, newly introduced vaccine's carrier and immune-stimulator is Bacterial ghost. The retained morphological and antigenic structures on BGs' surface increase their immunogenicity against gram-negative bacteria. Monophosphoryl lipid A, as well as, lipopolysaccharides and peptidoglycans on the surface of bacterial ghosts are responsible on triggering an immune response after interacting with other cellular components (Riedmann et al., 2007). Besides the retained intact surface components of bacterial ghosts, some enzymatic reactions are also maintained as an action of intact membrane-bound enzyme such as chloramphenicol acetyl transferase and β-galactosidase (Buckley & Hayashi, 1986).

These properties of *V. cholerae* ghosts were investigated pre-clinically, and the results showed the efficiency of the administered BGs in the evocation of specific immune response and providing maximum protection (Walcher et al., 2004).

The innate immunostimulators on BGs activate potentially both innate and adaptive immunity and prove the effectiveness of BGs-based vaccines in animal models, because of their ability in inducing several cell types to produce pro-inflammatory cytokines, which in turn, trigger the activation of T and B lymphocytes to encounter the cognate antigen (the envelope-bound foreign antigens on BGs). This immunogenicity of DNA-based vaccines could be potentiated by transfecting dendritic cells with DNA-encoded antigens (Hajam et al., 2017).

### 1.3.5. Bacterial ghosts' applications in cancer therapy

One of the most commonly diagnosed cancer is colorectal carcinoma. The common feature of this kind of cancer is the metastasis in the peritoneal cavity which decreases the prognosis and makes it resistant to many systemic chemotherapeutics. Despite the commonly use of Oxaliplatin –because of its immunogenicity and DNA damage properties- in the advanced stages of the disease, unsuccessful treatment is usually a challenge, due to the insufficient drug delivery to the site of action. Groza, et al (2018) have demonstrated the synergistic, immunostimulating and anticancer properties of BGs in combination with Oxaliplatin against CT26-Luc allografts. The activation of specific T cells and the induction of immunogenic cell death in murine models led to of CRC, prolonged survival, and as a result, long-term anti-tumor memory.

Based on the high immune competence of the peritoneal cavity and the dependence of Oxaliplatin activity on a strong and active immune system, arises the idea of combining Oxaliplatin with locally administered BGs (Melichar & Freedman, 2002).

William Coley (1891) suggested the idea of investing anti-bacterial immune response in the treatment of cancer, and succeeded treating different solid tumors using bacteria. Based on this idea, many experiments using live, attenuated or genetically manipulated bacteria were done to test their anti-cancer potential in human (Dzutsev et al., 2017), till the first line immunotherapy, Bacillus Calmette-Guérin, has being used locally against superficial bladder carcinoma (Fuge et al., 2015).

The most effective strategy in the treatment of stage III CRC is FOLFOX regimen (a combination from 5-fluorouracil, leucovorin and Oxaliplatin), which includes Oxaliplatin as a safer, next generation platinum derivate. The higher immunogenicity of Oxaliplatin in comparison to other platinum derivatives increases its dependence on the patient's immune state to show a better anti-cancer effect (Tesniere et al., 2010). The theory behind this immunogenicity is probably because of a tumor neo-antigens formation (adducts from platinum-DNA, or platinum-protein), which targets the immune system against platinum-labeled tumor-cells, and induces in turn immunogenic cell-death (ICD) after releasing ATP and HMGB1 (Kroemer et al., 2013).

The anti-cancer activity of oxaliplatin against CRC is strongly dependent on intestinal flora and the high immune competence of peritoneal cavity. The fact that explains the weak response in patients undergoing antibiotic treatment (Iida et al., 2013), and also the importance of combining oxaliplatin containing regimen with immunogenic adjuvants like bacterial ghosts (Iida et al., 2013).

In a collaborative project conducted in the MMCT lab, the research groups of Prof Petra Heffeter (Institute for Cancer Research, MedUni Wien) and Prof Werner Lubitz (BIRD-C, Vienna, Austria) on multiple peritoneal CT26 tumors in BALB/c mice, which had the tendency to be localized in the pancreatic region, an enhancement in oxaliplatin efficacy has been observed as a result on its combination with BGs. Although monotherapy using just oxaliplatin has resulted in a visible reduction in tumor burden, yet non-significant in comparison to the tumor-free case that resulted from the combination of oxaliplatin with BGs. That might be a response to enhanced surface CRT levels, and both ATP and HMGB1 release which in turn lead to enhance ICD, according to in vitro analysis. By repeating the experiment and detecting the results after 13 days from the first treatment cycle, small tumor nodules (but less number of nodules) where able to be detected as a result of transient nature of the response (Groza et al., 2018).

However, the immunogenicity of BGs was observed in both experiments through the enlargement of spleen, which reflects the activation of the immune system. Furthermore, an anti-tumor vaccination is possible, because of the absence of relapse for more than 80 days after multiple cycles from the combination treatment. After this period, a suspension of CT26 cells has been intraperitoneally injected, however, the rejection of these cells was a proof on the immunogenicity and the possible vaccination against CT26, as they were not be able to form any tumor again for 185 days after injecting them (Groza et al., 2018).

To prove the role of tumor-specific $CD8^+$ cytotoxic T-lymphocytes in the induced immune response as a result from the combination treatment, α-CD8 antibodies were applied one day before starting the combination therapy to mask this anti-cancer effect. Both the depletion in the number of $CD8^+$ cells and the enhanced tumor weight were evidences on the selected $CD8^+$

cytotoxic T cells mediated immune response, as a result from the combination treatment, against tumor cells (Groza et al., 2018).

### 1.3.6. Summary of bacterial ghosts' applications in biomedicines

Although the plasmid encodes for E lysis protein is essential in the production of bacterial ghost, an important difference between bacterial ghosts and other inactivated vaccines using chemical, heat, radiation or pressure, which usually combined with artificial adjuvants to increase their immunogenicity, is that Bacterial ghosts –which are non-living and free from genetic information- are not genetically manipulated organisms. The final preparations of BGs' vaccination are freeze dried products and their stability could last for several years at ambient temperature. Besides vaccination, BGs are used as drug carriers and targeted vehicles which deliver, in a high specificity, active substances to the tumor cells and allow, at the same time, the reduction in the required dose and simultaneously reduce the side effects. Lastly, the preference of the enzymatic activity of BGs -in converting the substrates in the environment where they found to active compounds - to the intestinal tract, presents them as novel probiotics (Lubitz et al., 2009).

## 1.4. Features, challenges and future applications for Bacterial ghosts

A number of studies demonstrate the importance of bacterial ghosts as drug delivery vehicles, vaccination adjuvants, and mammalian bio-therapeutics and prove their effectiveness. The main focus lies on their role as adjuvants in vaccination either alone or in combination with another vaccine's subunits. The vaccination using BGs could be either prophylactic or in some cases therapeutic, in the treatment of infectious as well as non-infectious diseases (Lubitz, 2001).

In the common production of bacterial ghosts, dextran can be used as a matrix to fill their internal lumen. For targeting purposes, these matrixes could be substituted with various ligands which has the ability to bind to specific targets. Another advantage of ghosts in vaccination is that they retain the immunogenic determinants as there is not any inactivation step during recombinant ghosts production, which gives them a superiority over traditional inactivated vaccines. The limitation in the capacity of antigens carriers is always a problem in the production processes. Using BGs as vaccines carrier eliminate this obstruction by their abilities to unlimited size of foreign antigens in their internal lumen, periplasmic space and cytoplasmic membrane (Eko et al., 1999).

Antigenicity of BGs is sometimes a challenge in their therapeutic applications. Therefore, safety issues should be considered especially for immunocompromised patients. Besides, the instability and BGs targeting must be controlled, optimized and validated during the production steps. Another challenges that should be considered are the required drug concentration at the site of action, and the localization on the superficial layers and poor penetration in the cells (Lubitz, 2001).

Bacterial ghost has a promising future in many immunological and genetic applications and in the field of biotechnology and bacteriology as in vitro/ in vivo carrier vehicle for many drugs and bio-therapeutics (Lubitz, 2001).

## 2. Archaea

### 2.1. Gut microbiota and host's cancer relationship

'Gut microbiota' is a term includes different kinds of commensal microorganisms such as bacteria, archaea, fungi and some viruses that populate mainly the large intestine of human intestinal tract. Numerous studies had proved the essential influence of the microbiota that cover body surfaces, especially the gut microbiota, on host's homeostasis and different vital functions such as controlling the expansion of intestinal pathogens and inhibiting their systemic infiltration, vitamins production, and metabolizing some dietary compounds (Lynch & Pedersen, 2016). The imbalance in the composition and ratios of these microorganisms could lead to a status called 'dysbiosis', which could be a leading cause for cancer and other pathologies (Carding et al., 2015).

Many metabolomic and metagenomic studies on gut microbiota were designed to illustrate the composition and functions of these microorganisms, and in turn, their impact on host's health and pathologies (Rothschild et al., 2018). Especially, the link between gut microbiota and tumorigenesis, cancer prevention and anti-cancer mechanisms, both locally in gastrointestinal tract and in other distal tissues (Fulbright, Ellermann & Arthur, 2017). The relationship between microbiome and cancer is bidirectional, as the microbiome composition could be altered as a consequence of cancer development, and also the changes in microbiome could affect the progression of cancer (Zitvogel et al., 2017).

### 2.2. Role of gut microbiota in cancer treatment

The main goal of anti-cancer therapies is the targeted eradication of malignant cells. However, the toxicity of these agents is not restricted on cancerous tissues, their serious side effects extended to affect healthy tissues (Bhang et al., 2015). The necessity in using these toxic agents arises from the complex construction of tumors, their abilities to adapt and progress within their hosting environment, and their tendency to accumulate mutations, which have the ability of transforming normal cells into malignant form by controlling the genes mainly responsible on DNA duplication and repair. The accumulation of these genetic and epigenetic mutations lead to the formation of multiple clones of cancerous cells, each with different response to anti-cancer therapeutics, and could in turn be the reason behind tumor relapses (Thorsson et al., 2018; Dagogo & Shaw, 2018). Integrated and personalized therapies are promising to overcome this resistance, based on enhancing the immune system activity to fight and eliminate these genetically unstable malignant cells (Thorsson et al., 2018).

“Targeted immunotherapy” is the new approach in cancer treatment. It has the potency, together with chemo- and radiotherapy, on boosting the patient’s immune activity against cancerous cells, as well as, overcoming the resistance against these therapeutics and prohibiting the relapse of cancer (Toh, 2018). An important strategy in reducing the toxicity and improving the effectiveness of anti-cancer therapies is modulating gut microbiome composition, which could be affected through radio-, chemo-, and immunotherapies. These microbiota have in turn a strong influence on patients’ response against anti-cancer therapeutics, and it is important to identify manipulate the factors that have an impact on their composition. Fighting dysbiosis after chemotherapy considered as an adjuvant to anti-cancer treatment and a potential strategy in enhancing the efficacy of chemo- and immunotherapy, and consequently reducing tumor mass and preventing its relapse (Fessler & Gajewski, 2017)

The idea of incorporating the bacteria in attempt to cure human malignancies goes back to 1890 after the first intratumorally injection of heat-inactivated Streptococci (Nauts, Swift & Coley, 1946). Later on, *Mycobacterium bovis* showed success in reducing the relapse of restricted bladder tumor, after injecting it into the bladder by triggering a local immune response. Orally administered *Lactobacillus casei* reduced also the recurrence of superficial bladder carcinoma

(Zbar et al., 1970; Aso & Akazan, 1992) through stimulating the host's macrophages and NK cells against cancerous cells. The success of intradermally injected *Mycobacterium obuense* in activating APCs and cytotoxic T cells against melanoma and pancreatic ductal carcinoma, along with the genetically modified *Salmonella typhimurium* in colonizing the tumor and triggering a direct cytotoxic effect against cancerous cells, had increased the research in this domain in order to manage the clinical outcomes associated with the prolonged activity, as well as, avoiding the bacteria-associated toxicity, while incorporating intra-tumor injected bacteria in cancer treatment (Felgner et al., 2016; Kramer et al., 2018).

### 2.2.1. Crosstalk between gut microbiota and host

The "gut-brain axis" is the bidirectional connector between the gut and the nervous system, which modulate the digestive and metabolic activities of gastrointestinal tract through the secreted hormones and neuropeptides on each side of GBA. The gut represents an interface that separates the gut microbiota from the rest of the body, and at the same time, it is an important communication gatekeeper, which insure a bidirectional crosstalk between them. Although gut microbiota could alter the digestive processes and gastrointestinal motility through inducing or inhibiting enteroendocrine cells of the gastrointestinal tract and also could modulate the host's immune system, the host's hormones alter in turn the composition of these microbiota (Sandrini et al., 2015).

### 2.2.2. Tumor suppressing role of gut microbiota

Based on the crosstalk between the gut microbiota and their host, the composition of these microbes and their products might have positive or negative impacts on tumor genesis and development. SCFAs, such as butyrate and propionate, are an example on these products that illustrate a positive, in vitro and in vivo, general anti-tumor effect, by inhibiting histone deacetylases in host's colorectal cancer and Lymphoma cells (Jan et al., 2002; Wei et al., 2016). Bacterial lipopolysaccharides (LPS) on the outer membrane of gram-negative bacteria, are an example on the probiotics' derived molecules that are able to indirectly modulate the host's immune system through activating toll-like receptor 4 (TLR4) on the surface of host's cells, and in turn triggering T cell-mediated, anti-cancer immune response (Paulos et al., 2007). Several studies had illustrated the importance of Lactobacilli in the elimination of precancerous, and in some cases, cancerous cells, through stimulating NK cells, dendritic cells and other host’s immune cells. Although it was not clearly identified, which bacterial bioproducts were responsible on these mechanisms, lactobacillus casei ferrichrome metabolite had been identified as an apoptosis trigger and antineoplastic agent in mice (Konidhi et al., 2016). Finally, anti-tumoral immunosurveillance could also be stimulated through bacterial derived pyridoxine (Aranda et al., 2015).

### 2.2.3. Tumor promoting role of gut microbiota

Preserving a constant composition of healthy microbiota in the gut is essential to promote normal physiological functions. However, alterations in this composition could lead to the development of certain pathogenic populations “gut dysbiosis”. Many pathologies could arise as a result to this dysbiosis, such as bowel inflammation, neurodegenerative diseases (Rea et al., 2018) and even triggering cancer growth, which could be locally in the intestine or in distal tissues, because of the altered metabolism and the impaired functions of the immune system, based on studies performed on pathogen-free mice to illustrate the different mechanisms of tumorigenesis and cancer progression (Bhatt, Redinbo & Bultman, 2017).

### 2.2.4. LGG as probiotic model in cancer treatment

Because of their potential role in the restoration gut microbial balance, Lactobacilli probiotics are proved to have supportive properties against gastrointestinal toxicity associated with chemotherapy, among these probiotics, *Lactobacillus rhamnosus GG* (LGG) had been closely studied and characterized, as a gut resident bacterium, because of its anti-inflammatory properties (Khailova et al., 2017). Studies on animal models illustrated the potential ability of orally administered LGG in the attenuation of gut epithelial injuries mediated by radiation effect and the administration of 5-FU, through restoring both physiological function of intestinal epithelial barrier and gut microbiota balance. Besides the profitable role of LGG in reducing the adverse effects related to anti-cancer therapy, many *in vitro* and *in vivo* studies illustrate LGG potency in modulating cancer development, which could either have a direct effect on cancerous cells or indirect effect through modulating the immune system (Riehl et al., 2018).

## 2.3. Archaea in Human Gut

The low oxygen concentration in the human colon insures a favorable medium for the growth of microbiota, especially for the strict anaerobes, which form over 90% of this population. The percentage of Archaea genes could be varied between different populations, ranging from 1-2% (Zhernakova et al., 2016). Methanogenic archaea are the main type of human colon archaea. Their abundance is highly heritable and remains stable. An exception on that is the detection of halophilic archaea in the colon of patients with inflammatory bowel disease (Goodrich et al., 2014; Oxley et al., 2010).

The fermentation end products derived from bacterial species that dominate the human colon are the main source of acetate, methanol and H2, which are main substrates in methanogenesis. The presence of numerous bacterial populations in the neighborhood from archaea is the reason behind the lateral gene acquisition in archaea (Lurie-Weinberger, Peeri & Gophna, 2012). This lateral gene transfer from bacteria is a sign of the adaptation and evolution properties of archaea. An evidence on that over 15% of the most abundant archaeon coding genes “Methanobrevibacter smithii” are originally bacterial genes. Encoding adhesin-like proteins, metal transporters, ABC transporters and glycosyl-transferases are examples on the essential participation of these acquired genes in the surface functionality of archaea and the adaptation with their environment (Lurie-Weinberger, Peeri & Gophna, 2012).

### 2.3.1. Gut methanogens and human health

*Methanobrevibacter stadtmanae* is another example on methanogens that colonize human colon. It has the ability to strongly induce the release of pro-inflammatory cytokines from monocyte-derived dendritic cells, which could be induced through both *M. stadtmanae* and *M. smithii* especially in patients suffering from inflammatory bowel disease (Bang et al., 2014). Many mice-based studies had suggested that human obesity could be referred to methanogens, because of the increased production of SCFAs with collaboration of bacteria. However, more recent evidences based on human studies illustrate the linkage between *M. smithii* and *leanness* (Goodrich et al., 2014). The relevance between chronic constipation and the presence of gut methanogens is another example on the association of these methanogens in human physiological functions, because of the methane, which is responsible on 59% reduction of intestinal transit time. In order to support these in vitro data, lower prevalence of methanogens had been associated with recurrent diarrhea episodes in patients with bowel inflammatory disease, in comparison with normal values from healthy individuals (Pimente et al., 2012).

Gut microbiota are the main producers of Trimethylamine as a metabolite for both choline and creatine. The host enzyme flavin monooxygenase is responsible on further Trimethylamine oxidation into N-oxide derivative (TMAO). Many mice-based studies had proved the tendency of plasma trimethylamine oxide (pTMAO) to promote atherosclerosis, and further to be considered as a potential biomarker for cardiovascular diseases. As a result, archaeal populations exhibit beneficial role in reducing methanol toxicity, preventing the accumulation of trimethylamine and in turn reducing the production of TMAO (Koeth et al., 2013). Based on these benefits, arises the possibility of utilizing these archaea, in archaebiotic form, in preventing trimethylaminuria and cardiovascular diseases. Experimental studies on *Methanomassiliicoccus luminyensis B10* showed the ability of these strains to reduce TMA through H2 in the purpose of methanogenesis, and suggested the possibility of utilizing members of this archaeal strain in the treatment of some metabolic diseases (Brugere et al., 2014).

### 2.3.2. *M. stadtmanae, M. smithii* and *M. luminyensis* as commensals in the human intestine

Despite the longtime of research on Methanoarchaea as commensals in human intestine, neither their abundance and diversity nor their role in modulating the human immune system is clearly examined. Yet the instant studies focus on the syntrophic interaction between Methanoarchaea and bacteria, their bioenergetic role, and demonstrate the large abundance of *M. smithii* in inhabiting human gut with 29% lower abundance of *M. stadtmanae* (Dridi et al., 2009; Scanlan, Shanahan & Marchesi, 2008). However, the abundance of M. stadtmanae was detected to be higher in patients with IBD. Besides their immunological properties on the immunized mice and rabbits (Blais-Lecours et al., 2014), methanoarchaea have the ability to interact with immune cells or intestinal mucosa, and as a result, modulating the composition of human gut microbiota (Dridi et al., 2009). Together with the results from Bang’s et al. (2014) experiment, which prove the strong ability of *M. stadtmanae* (DSM 3091) to activate moDCs, at least this strain might have a direct or indirect correlation with human gut inflammatory conditions. However, other gut methanoarchaea, such as *Methanomassilicoccus luminyensis*, the less commonly detected methanoarchaeon in human gut (Bridi et al., 2012), might act diversely when they are in contact with human epithelial or immune cells (Bang et al., 2014).

#### 2.3.2.1. Immunogenic properties of *M. stadtmanae* and *M. smithii*

Despite the indirect pathogenicity of methanoarchaea in promoting the growth of pathogenic microbes (Conway & Macario, 2009), evidences on the immunogenicity of archaea found in bioaerosols, as well as, increasing their prevalence in patients with inflammatory bowel syndrome, together with the diversity of archaea in human intestine and oral cavity and on the skin, powered the research toward proving the probability of recognizing methanoarchaea, as non-self-molecules, by the human innate cells. However, a particular archaeal-associated pattern recognition receptor is essential in proving the possibility of archaeal influence on the overall immune homeostasis of human body (Blais-Lecours et al., 2011; Blais-Lecours et al., 2014).

#### 2.3.2.2. Intestinal immune response toward Methanoarchaea

As inhabitants of human gut, the abilities of both *M. stadtmanae* and *M. smithii* in activating Caco-2/BBe intestinal epithelial cell line were detected, through monitoring the level of AMPs and proinflammatory cytokines expressed and released from these cells. No significant change was detected in the transcription of genes encoding for human beta defensin 1, HBD4 or HD6, IL-8, TNF-a or human cathelicidin LL37 in intestinal epithelial cells, as a response on stimulating these cells with with both Methanoarchaea strains,  and in turn, no change in the level of released IL-8 was reported (Bang et al., 2014). Because of the absence of epithelial recognition to these Methanoarchaea, and at the same time, the direct role of the innate immune cells in invading intestinal microorganisms was further studied on monocyte-derived dendritic cells (human moDCs) (Bang et al., 2014).

#### 2.3.2.3. Activation of moDCs through *M. stadtmanae* and *M. smithii*

After 20 h from stimulating moDCs with *M. stadtmanae* and *M. smithii*, the activation of dendritic cells was monitored through analyzing the released IL-Ib and TNF-a. Cell concentration-dependent manner detected the higher amount of both cytokines, released as response on the stimulation using *M. stadtmanae*, and in turn a stronger ability of this strain to activate immune response, in comparison to the lower cytokines released after the stimulation with *M. smithii*, and thus weaker immune cell activation (Bang et al., 2014). These results revealed a strong correlation with the outcomes of Blais-Lecours et al. previous study, that detected a higher rate of inducted plasma IgGs and accumulated myeloid dendritic cells in mice treated intranasally with *M. stadtmanae* than mice treated with *M. smithii,* together with the higher amount of TNF-a released after inducting peripheral blood mononuclear cells with *M. stadtmanae* in comparison to *M. smithii* (Blais-Lecours et al., 2011; Blais-Lecours et al., 2014).

#### 2.3.2.4. The essentiality of *M. stadtmanae* and *M. smithii* phagocytosis in activating moDCs

Based on the crucial role of some intestinal immune cells in the uptake of commensal microorganisms, and further, the activation of other types of immune cells through different bacterial species (Rescigno, 2010), this raised the necessity to detect the association of phagocytosis in activating moDCs through Methanoarchaea. Bang et al. 2014, indicated the rapid phagocytosis of M. stadtmanae which was essential for further cellular activation, by confocal microscopy visualization of the DAPI-prestained moDCs. However, after 4 hours from stimulating moDCs with *M. smithii*, no lysosome formation for these archaea was detected through Lyso Tracker, which displays lysosomes formation. TEM analysis also detected slower and less frequent phagocytosis of *M. smithii* by moDCs, which also revealed the dependence of cytokines release on phagocytosis (Bang et al., 2014).

#### 2.3.2.5. The role of *M. stadtmanae* and *M. smithii* in activating and modulating moDCs

Bang and colleagues (2014) illustrated somehow the higher potency of *M. stadtmanae*, in comparison with *M. smithii*, in activating moDCs, by, inducing the expression of CD197 surface receptors and CD86 co-stimulatory receptors, which are essential in further activation of adaptive immune response represented by T- and B-cells. These results are supported with earlier studies detected the development of specific IgG antibodies as a representors to adaptive immunity in patients with IBD (Blais-Lecours, 2014).

Bang and colleagues (2014) used qRT-PCR technique to monitor the expression of AMPs in human moDCs expressed to both *M. stadtmanae* and *M. smithii*. Up-regulation of HBD1 genes encoding for Antimicrobial peptides had been detected in moDCs, although DCs are not considered as essential producers of human AMPs. At the same time, 6-folds down-regulation in the expression level of cathelicidin LL37 had been observed in *M. stadtmanae* activated moDCs, in comparison to 3-folds in cells incubated with *M. smithii*. These results suggested to represent archaeal protective mechanism against human immune clearance, as the expression of LL37 genes was shown to be down-regulated in both monocytes and epithelial cells of patients with enteric infections (Dürr, Sudheendra & Ramamoorthy, 2006).

#### *2.3.2.6.* Human immune cells recognition of *M. stadtmanae* and *M. smithii*

Based on the confocal scanning microscopy results from Bang et al. study (2014), the ability of *M. stadtmanae* to rapidly activate moDCs could be a result to the specific recognition of this methanoarchaea strain, and not *M. smithii*, through moDCs. The mechanism, which these two strains use, in activating the immune cells appears to be different from bacterial MAMPs/ TLRs recognition mechanism (Bang et al., 2014; König, 2010). Although it is generally a pseudomurein layer that form the cell envelope of both methanoarchaea strains, *M. stadtmanae* and *M. smithii*, small structural differences in pseudomurein could alter the human immune cells recognition ability toward these methanoarchaea strains. This theory had been suggested since 1984 by Conway and colleagues, while studying the impact of monoclonal antibodies in inducing structural changes in the pseudomurein layer of methanoarchaea, and thus altering the immunological response toward them. Evidences on the genomic heterogeneity and metabolic adaptation of gut methanoarchaea, *M. smithii*, were also discussed by Samuel and colleagues (2007). As a result, the immunological responses toward *M. stadtmanae* and *M. smithii* depend strongly on pseudomurein configuration in the cell envelope of these methanoarchaea, and thus, inducing structural alterations on this layer could alter their immunogenic properties (Bang et al., 2014).

### 2.3.3. Immunogenic properties of *M. luminyensis*

The different mechanisms by which methanoarchaea strains, *M. stadtmanae* and *M. smithii*, activate human immune cells, had been studied by Bang and colleagues (2014), and the types of released cytokines were also reported (Bang et al., 2014; Bang et al., 2017). Unlike the strong activation to immune cells through *M. stadtmanae*, the activation of *M. luminyensis* to immune cells resembled the low ability of *M. smithii* to activate moDCs and inducing phagocytosis, besides releasing low amounts of TNF-α and IL-1β cytokines (Bang et al., 2014). Although it is not yet detected, which human receptor is responsible on recognizing archaeal molecular patterns, earlier studies suggested the linkage between pseudomurein and heteropolysaccharides conformational changes, in the cell envelope of *M. smithii* and *M. luminyensis*, and the varied illustrated immune responses, which could be also the reason behind decreasing the phagocytosis of these strains by moDCs (König, 2010; Gordon, 2002).

### 2.3.4. Anti-cancer properties of Halophilic Archaeal supernatant metabolites

The increasing tendency toward recruiting microorganisms in anti-cancer studies, goes back to their importance as reservoir for many natural compounds with anti-cancer properties. The reason behind the unique features of halophilic archaeal metabolites is the ability of this strain to produce them in extreme environmental conditions. An example on these compounds are halophilic archaeal carotenoids. These carotenoids' anti-cancer properties and abilities to induce apoptosis were investigated in many studies (Hou & Cui, 2018; Hegazy et al., 2020). Because of the increased interest to study the effect of halophilic archaea's metabolites in cancer treatment, Safarpour and colleagues (2019) screened the supernatant metabolites of different halophilic archaeal strains, and detected the potency of *Halobacterium salinarum* supernatant metabolites in selectively reduce prostate cancerous cells' viability, without altering the viability of normal cells.

#### 2.3.4.1. *In vitro* evaluating the Anti-cancer potential of halophilic Archaeal supernatant metabolites

In order to specify the *in vitro* anti-cancer mechanism of *Halobacterium salinarum's* supernatant metabolites, Safarpour and colleagues (2019) assessed the apoptotic rate in PC3 and DU145 cells treated with the supernatant metabolites. Although the results of this experiment revealed a significant enhancement level of CASP3 expression and late apoptosis in both cell lines, the abilities of archaeal carotenoids and different moderately halophilic bacterial supernatant metabolites in inducing apoptosis were reported in previous studies (Sarvari, 2015). However, the enhanced level of early apoptosis in androgen-dependent PC3 cells, treated with the supernatant metabolites, and the increased sensitivity of androgen-independent DU145 cells to chemical therapeutics (Jayakumar, 2014), support the possibility of combining the current anti-cancer therapeutics with *Halobacterium salinarum's* supernatant metabolites.

In the same study of Safarpour and colleagues (2019), *Halobacterium salinarum's* supernatant metabolites had the ability of reducing the size and number of prostate cancerous spheres, as a result from their effect on stem-like cells, which are responsible on spheres formation and tumor recurrence (Liu, et al., 2011; Lin et al., 2012). Based on these results and the down regulation of SOX2 genes expression, which is considered as an important marker in detecting prostate cancer progression, *Halobacterium salinarum's* supernatant metabolites could be used in preventing human prostate cancer progression.

#### 2.3.4.2. *In vivo* evaluating the Anti-cancer potential of halophilic Archaeal supernatant metabolites

Based on in vitro results, Safarpour and colleagues (2019), examined the effect of *Halobacterium salinarum's* supernatant metabolites (SM) *in vivo*. The results showed a strong reduction in the tumor size after treating the cells, and especially PC3, with SM. The same outcomes were also observed, by Haque and colleagues (2016), after reducing Ehrlich Ascites Carcinoma's growth in mice treated with ethyl acetate extract obtained from ANAM-5 and ALAH-10 (two *Streptomyces sp.* co-culture) Furthermore, the reduction in the proliferation rate of the cells treated with SM had also been observed through staining the cells with Ki67 antibodies, which facilitates their detection (Roomi et al., 2005).

### 2.3.5. Anticancer and antiviral properties of haloalkaliphilic archaeon *Natrialba* sp. M6

Because of the importance of halophilic archaea as a natural source of carotenoids, and at the same time, the deficiency in the resources that demonstrate the biological impact of their metabolites, Hegazy and colleagues (2020) isolated the carotenoids of *Natrialba* sp. M6 in order to identify their biological roles. *In vitro* studies were done for the first time on $C_{50}$ carotenoid bacterioruberin (the most abundant extracted carotenoid) in order to investigate its anti-cancer and anti-viral properties. In comparison with 5-fluorouracil in treating cancer, applications of $C_{50}$ carotenoid bacterioruberin revealed a higher caspase-mediated apoptotic effect and greater inhibition effect of matrix metalloproteinase 9. Besides, the antiviral effects of the tested compound (anti HCV and HBV) rely on its ability to strongly inhibit both DNA and RNA polymerases and thus suppressing the viral replication. Because of the greater potency of this compound to eliminate the viral infected cells in comparison to the currently available drugs, besides its anti-cancer properties, this compound could be a natural alternative in hepatitis and cancer treatment (Hegazy et al., 2020).

### 2.3.6. Archaeal and bacterial CRISPR/Cas9 system and its applications in cancer therapy

Despite the noticeable improvement in the exogenous genes' insertion techniques, the workers in the domain of gene therapy still facing a lot of technical challenges, especially in targeting the genetic material, limiting its expression of a dominant mutation within a desirable cell type or tissue without affecting the neighbor cells, the ability to control the unpredictable gene expression and increasing the transgenic size capacity and eliminating the undesirable effects of viral genomes and other impurities (Mollanoori & Teimourian, 2018).

Besides TALENs and ZFNs programmable nucleases, clustered regularly interspaced short palindromic repeats/CRISPR-associated nuclease 9 (CRISPR-Cas9), which had been isolated from bacterial and archaeal type II acquired immune system, has been widely used in accurately editing and correcting targeted genes, because of its efficient genome editing properties and DSBs introduction without the necessity of engineering novel proteins (Maeder & Gersbach, 2016; Teimourian & Abdollahzadeh, 2015).

CRISPR/Cas technology appears to have many cancer immunotherapeutic applications for the purpose of enhancing the affinity of T-cell receptors (TCRs), of the genetically modified T cells, toward specific tumor antigen. Besides, ex vivo applications of CRISPR/Cas system in genetically improving autologous T cells are widely accepted in order to induce the production of specific chimeric antigen receptor (CAR), and in turn, stimulating a personalized cancer immunotherapy by transferring the genetically manipulated T cells back into the patient (Zych, Bajor & Zagozdzon, 2018). CRISPR/Cas9 system could also help mediating miRNA knockout, in order to interrupt the role of these miRNAs in regulating many normal and pathological cellular events, and in turn, hampering the tumorigenic effect of some viral infections, such as HBV, HCV, HPV and EBV (Chang et al., 2015). Finally, epigenetic modifications through

CRISPR interference (CRISPRi) might also be applicable in cancer therapy, as they suppress the activities of DNA's transcription elements (Fineran & Dy, 2014).

## 2.4. Tumor-targeted drug delivery systems and the complexity of tumor microenvironment

The current cancer research is focusing on recruiting nanoscience in developing and targeting anti-cancer therapeutics. Prolongation in the circulation time, adjustment in the release of these therapeutics, and optimizing their pharmacokinetics could be achieved by using nano-carriers altering their surface characters. Paclitaxel micelles and paclitaxel albumin nanoparticles are examples on the FDA approved nanoparticles which exhibit higher effectiveness and lower side effects than the traditional treatment using Paclitaxel (Sagnella, McCarroll & Kavallaris, 2014).

Developing new anti-cancer therapeutics is a tough process consisting of many preclinical steps, through which the newly discovered or aimed to be developed drug is tested in vitro and in vivo on tumor culture models and animal models. According to preclinical results, the further performance of the tested molecules in clinical studies could be predicted. However, these results are not always accurate, because of the big difference between the characterizations of preclinical models and the physiology of the human body, which is the thing that minimizes the number of candidates that could be applied clinically (Fitzgerald et al., 2015). To optimize the clinical translation, monolayer cell cultures should be replaced by 3D screening models which resembles the physiological conditions of human body. These 3D cell cultures' properties mimic the physical barriers of tumors that interfere with the internalization of drug delivery systems into the tumor tissue. Besides, the heterogeneity of 3D cell models resembles cell-matrix interactions as well as cell-cell interactions which in turn has an impact on altering the active state of essential signaling pathways (Griffith & Swartz, 2006; DesRochers, Palma & Kaplan, 2014).

In order to minimize the gap between clinical and preclinical studies using 3D cell culture models, multicellular tumor spheroids (MCTS) have been used, as they resemble the 3D structure of tumor tissues and retain the properties of their physiological barriers in superiority to other 3D cell models such as scaffold-based models and tumor tissue explant models. These properties and other economic reasons demonstrate the superiority of MCTS in studying the efficacy of drug and gene delivery systems, their targeting and penetration potential, and their capacity in recruiting other cell types (Hutmacher et al., 2009).

Delivering an active molecule to a targeted tissue in the human body is a real challenge, because of the complexity of tumor microenvironment which includes cell-cell interactions, oxygen gradient, extracellular matrix, acid gradient and many other obstacles that impede the efficient delivery of administered anti-cancer therapeutics. Most importantly is the negative effect of extracellular matrix that surrounds tumor cells, which builds up of collagen, proteoglycans and many other fibrous proteins that adsorb the drug and accelerate its clearance. Besides the mechanical signals and the resulted biological responses mediated by integrins- that anchor tumor cells in ECM, - cell-cell interaction between tumor cells and other non-epithelial cells results in biological responses that lead to enhancement in its growth, metastasis and its ability to escape the immune response. Therefore it is important to test the efficacy of the targeted ligands on 3D cell models rather than single cell cultures (Young, 2013).

The hollow-heart sphere of tumor foci consists of a reproducible, highly perfused outer layer, and hypoxic and necrotic core, which is non-perfused and, as result, observes lower oxygen and nutrients exchange. One of the most important features of tumor microenvironment is the acidic pH of this hypoxic region as a result of the incomplete oxidation processes and accumulation of lactic acid which in turn leads to alterations in drug release profile. Induction of MDR-1 genes in the necrotic core could be a result of the hypo-oxygenation in this area, which leads to decrease cellular internalization of the administered therapeutics (Shin et al., 2013).

## 2.5. Multicellular tumor spheroids (MCTS)

### 2.5.1. Properties of multicellular tumor spheroids

MCTS are in vitro 3D models composed of aggregations of tumor cells alone or as scaffolds of these cells co-cultured with another, differently treated, suspended or embedded cells, such as immune cells, fibroblasts and endothelial cells, thus simulating in vivo cell-cell and cell-matrix interactions. These MCTS have been widely used as efficient in vitro tools to evaluate the impact of tumor cells' metabolism on drug delivery in a more convenient manner. With their 3D spherical geometry and ECM components, resemble the spheroids the human cells and tumor tissues, especially the big spheroids (diameter > 400-500µm), which distinctly composed of outer reproducible layer and inner hypoxic and necrotic core. Because of these similarities to human body, spheroids have the ability to express identical genes and proteins to those expressed in human tumor tissues for a long period of time, which could last for two weeks and in provides in turn the possibility to run long duration researchers. Subsequent in vitro studies could be applied on spheroids, such as using flow cytometry to analyse cells viability, and cryo-sectioning for further tissue analysis (LaBarbera, Reid & Yoo, 2012).

### 2.5.2. 3D spheroids as an *in vitro* alternative for tumor tissues

Because of the high metabolic activity in solid tumors and the insufficient vasculature of the core, these tissues are characterized with hypoxic and necrotic centers. In comparison to properly oxygenated tumor tissues, these areas are more resistant to conventional chemotherapies and radiations. In order to overcome this resistance, many studies had suggested alternative treatment strategies. One of them is directly expressing therapeutic genes in tumor tissues by delivering them using bacterial vectors, which selectively colonize cancerous tissues such as *Listeria monocytogenes* and *Escherichia coli* (Jiang et al., 2010). MCTS from different tumor cell lines are widely used as preclinical model systems, as they are constructed under appropriate conditions, and resemble solid tumors features in their physiological parameters and their oxygen gradient in all of their proliferating, apoptotic and necrotic areas (Hirschhaeuser et al., 2010).

In a study done by Osswald et al, HT-29 MCTS, with an intrinsic resistance to 5-fluorocytosine, were evaluated as in vitro models for investigating the anti-cancer therapy using gene delivery vectors constructed using anaerobic bacteria, such as *Bifidobacterium bifidum*, which tend to selectively localize and replicate inside the low oxygen gradient areas of MCTS (the hypoxic center). They proved the efficiency of HT-29 MCTS as a substituent to solid tumors in evaluating the efficiency of recruiting live bacteria expressing the secreted enzyme ‘chromate reductase’ to deliver the cytostatic prodrug CB1954 to the hypoxic core, and therefore, inhibiting the growth of the spheroids (Osswald et al., 2015).

### 2.5.3. Spheroids production methods

For an efficient construction of spheroids, a tendency toward cell-cell interaction must preferably dominate the cell-substrate interaction in non-adherent culture method from spheroids production as well as hanging drop culture and suspension culture methods (Zanoni et al., 2016).

The main concept in spheroids' production using 'Suspension culture method' is promoting the spontaneous aggregation of cells through retaining a constant cell- or media velocity and in turn reducing the gravity's negative effect on their aggregation. In order to simulate a dynamic and a long-term physiologic condition, NASA bioreactors and other methods such as spinner flask and roller tube could be enrolled in spheroids production. The customized equipment required to produce spheroids using this method, and difficulty in replacing the nutritive medium and the lack of sufficient control on spheroids uniformity are the main disadvantages in using 'Suspension culture method' in spheroids' production. Han et al developed a method which solves the problem of using specialized microfabrication tools, and instead, using PEG/DEX ATPs system, which is a density adjusted method and enables spheroids separation by only adding few fresh drops from growth medium, replacing with that the numerous pipetting steps (Han, Takayama & Park, 2015).

'Non-adherent surface culture' is another method for spheroids production which depends on promoting spheroids' formation on low or non-adherent substrates, such as agarose gel, the culture medium in 'liquid overlay' method which substitutes in that the use of ECM (Yuhas et al., 1977). The problem of agarose low biocompatibility had been solved by replacing it with several biomaterials, such as forming spheroids in a 96-well plate coated with poly-HEMA, which also increased the throughput (Ivascu & Kubbies, 2006). However, uniformity of spheroids size could be achieved by using reversed colloidal crystal scaffolds (Lee et al., 2009). Although it is easy and possible to produce spheroids and co-culturing different cell types using 'liquid overlay' method, the lack of uniformity in spheroids size and the possibility of arising some interactions between the scaffolds materials and the applied drugs and nanocarriers reduced the possibility of adopting it in the experiments that need higher accuracy (Mehta et al., 2012).

In order to control spheroids' size uniformity and ensure a high-throughput in anti-tumor therapeutics screening using spheroids produced from different lines of tumor cells, which could be also sometimes co-cultured with immune cells, cancer stem cells and many other cell types (Tung et al., 2011), ‘hanging drop method’ had been invented. This method of spheroids culture based on two principles; the surface tension of the cells suspension drops which are hold on to a lid, and the effect of gravity which promotes the aggregation of these cells into spheroids (Wu, Di Carlo & Lee, 2008). The longtime consumed in changing the medium of spheroids using ‘hanging drop method’ and at the same time the short duration of retaining the hanging drops, reduced the preferability of using this technique for long term experiments. To overcome these obstacles, Takayama et al took advantage of stereolithography technique to develop a micro-ring structure from 384 hanging drop wells, which prolonged the stability duration of this system (Hsiao et al., 2012).

The imperfections of traditional methods used in the formation of 3D spheroid models could be modified with the help of recent micro- and nanoscale biotechnology techniques. An example on that is combining microfluidic devices with spheroids formation in order to achieve desirable dynamic and perfusion conditions, resembling the physiologic environment of tumor tissues. In a research done by Cheung et al, the encapsulated spheroids, formed after few days of seeding alginate-encapsulated breast tumor cells within microchannels, were treated with doxorubicin in order to demonstrate the effect of this drug on altering the viability and proliferation abilities of treated cells (Chen, Gupta & Cheung, 2010).

### 2.5.4. Importance of MCTS in drug discovery and delivery

Developing tumor-targeting vehicles is the main challenge in current drug discovery and development. MCTS represents an efficient mean in studying the efficacy of targeted therapeutics and their ability to penetrate the physiological barriers. These spheroids are also useful in evaluating targeting strategies, such strategies include using exosomes and macrophages for targeting purposes.

#### 2.5.4.1. Evaluating drug efficacy

Proving drug efficacy is the most challenging and important step in drug discovery process. Taking anti-tumor therapeutics as an example, it is most important to evaluate drug cytotoxicity and ability to suppress the invasion of cancerous tissue as well as other properties of nanoparticles. The main limitation in the current studies, is using 2D culture models by which it is impossible to mimic the physiologic 3D context of human body. Using 3D MCTS has solved this problem and provided a suitable medium to evaluate tumor growth mechanisms, metastasis conditions, and to adequately detect the resistance behavior of these cells against cancer therapeutics (Heldin et al., 2004).

#### 2.5.4.1.1. Studying drug sensitivity

MCTS considered as a valid model to demonstrate the tumor cells' sensitivity toward the tested drug as they reserve the physiological barriers' properties which impede drug penetration, in contrast to 2D culture models which lack this property. Another important feature of tumor tissues which should also be considered during therapeutics evaluation is the high pressure of tumor interstitial fluid because of the uncontrolled vascularization, contractions of tumor interstitial matrix and the weak lymphatic accessibility to solid tumors. The increased rate of drug clearance due to the elevation of interstitial fluid pressure, in addition to the hypoxic regions in the core of tumor tissue are important features which lead to increased drug resistance (Heldin et al., 2004).

In order to demonstrate the differences between the abilities of 2D and 3D culture models to evaluate their sensitivity toward anti-tumor therapeutics, an experiment has been done by Shastri et al using 3D spheroids produced by hanging drop method. The enhancement in both ROS level and the expression of ABCB1 genes in 3D models was obviously higher than their concentrations in 2D culture models. In the same experiment, the resistance of spheroids against paclitaxel and gemcitabine was obviously stronger than 2D culture models. Based on the resistance of 3D MCTS to drug alone, further studies could evaluate drug-loaded nanoparticles' cytotoxicity using 3D models, in superiority to 2D culture models (Lamichhane et al., 2016).

In order to study the MDR of tumor cells against both doxorubicin and its better penetrable form -loaded nanoparticles of DOXA- , a novel 3D culture model, based on conventional liquid overlay method, was constructed by researchers at the University of Delaware. These spheroids were imbedded in acrylated and thiolated Hyaluronic acid (HA-AC/ HA-SH) scaffold. The enhancement in the level of apoptosis and MDR-associated proteins in 3D spheroids of prostate cancer cells was higher than 2D culture models. Another proof on the increased drug resistance in 3D spheroids is observing doxorubicin only in their cytoplasm using fluorescent microscope, at the time of detecting its presence in the nuclei of 2D culture models. Further experiments done by Torchilin et al proved the elevated expression of Bcl-2 as an indicator to the increased resistance in ovarian spheroids, and proved in turn the importance of these spheroids in evaluating the toxicity and accumulation level of PEGylated micelles loaded with doxorubicin. The results of these experiments reflect the importance of 3D culture models in assessing the resistance of tumor tissues against anti-cancer therapeutics and in turn determining the optimal dose and delivery system (Xu et al., 2014; Michel et al., 2016).

###### 2.5.4.1.2. Detecting tumor growth

Evaluating anti-tumor effect of currently developed drugs could be determined by their potency to inhibit tumor growth, which is complex to be determined using 2D culture models. Whether applying 3D spheroids for this purpose had simplified this complicated process by simply detecting spheroids’ diameter and volume with naked eyes using a microscope (He et al., 2011).

The well-known properties of retinoids as antiproliferative and differentiation-inducing compounds increased their clinical utilization in the prevention against some types of squamous-cell carcinoma. However, the toxicity of retinoids has limited their utilization. In order to reduce their toxic effects especially against human red blood cells and to investigate their abilities to be uptaken and retained in tumor cells, Mehta et al, studied the effect of different formulations from lipid encapsulated all-trans-retinoic acid (liposomes) on different MCTS constructed using liquid overlay method. The documented diameter of spheroids reflects their volumes which is a sign of the efficient uptake of retinoids and hence their tumor suppression properties. This study showed also that positively charged liposomes could be considered as efficient delivery systems for retinoic acid with a same effectiveness and less toxicity of the free drug (Parthasarathy et al., 1994).

###### 2.5.4.1.3. Detecting tumor metastasis

One of the most serious characters of cancerous tissues is their ability to spread to other organs, not just to neighbor organs but also to the distant ones. This metastasis process depends on the invasion capacity of malignant cells. For in vitro evaluation of tumor cells’ metastasis capacity, a gold-standard model based on transwell assay had been constructed in order to demonstrate the metastasis pattern in 3D context. An example on that is developing a 96-flat-bottomed well plate coated with ECM as an incubator for MCTS in order to test the anti-metastasis capacity of 17-N-Allylamino-17-demethoxygeldanamycin (Vinci et al., 2012).

Zhang et al had also tested the anti-metastasis properties of PTX-loaded liposomes on 4T1 cells-based spheroids. Although so many studies demonstrated the importance of MCTS models in evaluating the metastasis pattern of many cancerous tissues and the anti-invasive properties of nanoparticles-based anti-cancer therapeutics, the direct comparison of spheroids diameter before and after the treatment without considering tumor cells' growth and division, causes the lack of accuracy in the results based on this technique (Zhang et al., 2016).

#### 2.5.4.2. Evaluating drug penetration

The current anti-cancer researches aim to develop anti-cancer therapeutics based on nanoparticles. These nanoparticles-based new technology has succeeded in many domains and showed many advantages over the traditional therapy. However, a lot of challenges impede the effective use of these nanoparticles. For example, their low penetration level and potency to overcome the physiological barriers decrease their accumulation in hypoxic and necrotic areas and fail in reaching the desired, therapeutic concentration of these agents in the areas with low blood perfusion. Some animal models can help in the evaluation of distribution and penetration levels of drug molecules. However, the high costs and violent procedures had limited their usage and increased the necessity for developing in vitro evaluation models. Using MCTS as in vitro models for evaluation the penetration potency of anti-cancer nanoparticles (Basuki et al., 2013).

##### 2.5.4.2.1. Optimizing delivery systems' size and charge

Optimizing the size and surface charge of drug delivery systems is a critical step in developing *in vivo* effective nano-carriers for different anti-cancer therapeutics. MCTS models and confocal microscopy techniques help evaluating the penetration performance of fluorescent nano-carriers, and optimizing their pharmaceutical formulations. Optimizing the size of nanoparticles is critical to overcome the extracellular matrix barriers and allow the penetration through the small intercellular pores (Goodman, NG & Pun, 2008). In an experiment done by Chan et al, using microfluidic cultured MCTS, the penetration performance of PEGylated gold nanoparticles had been tracked after labeling them with a fluorescent dye. The results using confocal microscopy proved the tendency of small nanoparticles (smaller than 40 nm) to be accumulated inside the spheroids, and the larger ones (larger than 110 nm) to be rejected from spheroids. Not only the accumulation but also the retention ability of nanoparticles in MCTS models is crucial for evaluating their effectiveness. 50 nm had considered as the optimal size for in vivo penetration and accumulation of nanoparticles in tumor tissues (Tang et al., 2014).

Adjusting nanoparticles' size is not only important for their penetration and retention inside tumor tissues but also to prolong their circulation time. In order to optimize these two processes, a shrinkable gelatin-conjugated model of DOX-loaded gold nanoparticles had been designed by Gao's group. These nanoparticles were tested *in vitro* on different spheroids models to illustrate their penetration pattern. The, *in vivo,* long circulation time of this modified compound was maintained because of their large molecular size, and being substrates for metalloproteinase-2 enzyme, ensured the gradual degradation of their gelatin and enhanced their penetration into deeper tumor layers (Ruan et al., 2015).

Not only the particles' size but also their surface charge is critical while considering nanoparticles as therapeutic agents. It is essential in adjusting their blood protein binding capacity and their uptake by tumor cells. Although positively charged particles are highly uptaken through the cells, they are more likely to bind to serum proteins and less likely to penetrate tumor tissues. In contrast to negatively charged particles, which have lower tendency to be uptaken through the cells, but at the same time, they demonstrate a lower serum binding capacity and high potency to penetrate into deeper tumor spheroids layers (Huang et al., 2017).

In a study done by Huang et al, a spheroid-on-chip system was developed to study the effect of altering the charge of nanoparticles' surface, by surrounding it with protein corona, which converts the surface charge of NPs into negative charge, and also to demonstrate how their penetration and accumulation in the tumor could be affected through the fluid flow around it. The negative charge of polystyrene NPs gained through protein corona had increased their abilities to penetrate the spheroids and weakened their cells affinity. The NPs coated with protein corona were more likely to be affected with the exterior fluid flow, which was responsible on enhancing the penetration and at the same time stripping the NPs. As a result, it was ideal to optimize the penetration of NPs into spheroids by applying an external fluid flow to uncoated, negatively charged NPs (Huang et al., 2017).

###### 2.5.4.2.2. Evaluating the function of penetrating and targeting ligands

3D MCTS models had solved the problem of monolayer culture models, which lack the tendency of resembling *in vivo* cell-cell interaction, and provided the possibility of co-culturing it with another cell types such as immune cells, endothelial cells, and cancerous stem cells, in order to evaluate the ligated drug carriers efficacy in targeting these cells and inhibiting their crucial function in fostering the development and metastasis of tumor tissues (Perche, Patel & Torchili, 2012). Another important feature of these ligands, such as antibodies and cell-penetrating peptides, is their ability to deeply penetrate the cancerous tissues which promotes accumulating the therapeutic nanoparticles inside these tissues. The accumulation level could be tracked and quantitatively evaluated by with the help of fluorescent imaging techniques (VanDen Brand et al., 2017).

# Aim of Thesis

The present work is based on employing bacterial ghosts and archaea for *in vivo* studies with colorectal cancer models and *in vitro* three dimensional spheroids, respectively. Based on the importance of bacterial ghosts in boosting an immune response toward eradicating cancerous cells, near infrared (NIR) fluorescence microscopy techniques were used in the first project to study the biodistribution of AF750-labeled BGs within CT26 tumor bearing mice. In earlier work, BGs were studied in organs 24 hours after intraperitoneal injection. However, this work focuses on 2 hours after intraperitoneal administration of AF750-BGs and employs untreated tumor bearing animals as fluorescence imaging controls to avoid detection of autofluorescence. Importantly, this work also employed AF750-BGs spiked tissue sections (as artificial positive control) to optimize the exposure time for detecting NIR fluorescence, in order to avoid autofluorescence. Pancreas and pancreatic tumors were selected from CT26 tumor bearing mice and subjected to whole organs' sectioning, for detecting the presence or absence of specific NIR emission from AF750-BGs (Cy7 channel). The NIR signal from AF750-BGs was validated by co-staining the sections for ice nucleation protein (immunostaining and detection of FITC-labeled secondary antibodies) of BGs and checking the overlap of Cy7 channel with FITC channel.

The second project in this work, Archaea infiltration project, based on previous tumor targeting studies aimed to incorporate anaerobic bacteria in cancer treatment, because of the affinity of these bacteria to the hypoxic centers of cancerous tissues. Different types of anaerobic bacteria and bacterial spores showed the ability to colonize and germinate inside these hypoxic centers with the aid of 3D MCTS as an *in vivo* alternative to cancerous tissues. However, the pathogenicity of these bacteria had limited their clinical utilization in cancer treatment, hence arises the need for alternative, nonpathogenic targeting microorganisms. An example on these microorganisms are intestinal archaea. Because of the differential role of intestinal microbiota in affecting the formation, metastatic characters, cure and recurrence of colorectal carcinoma, this part aimed to study the *in vitro* localization of the nonpathogenic, strictly anaerobic, AF488-labeled archaea, Methanococcus maripaludis S0001, in 3D MCTS from CT26-Luc cells, in order to predict the *in vivo* behavior of these archaea in cancerous tissues. The localization of archaea in the DAPI stained spheroids' cryosections aimed to be imaged and tracked at 3 timepoints; 24, 120 and 168 hours after inoculating the spheroids with archaea, which could predict in turn the *in vivo* behavior of these archaea, in tumor tissues.

# Materials and methods

Bacterial Ghosts (BGs) used in this study were kindly provided by Prof Werner Lubitz (BIRD-C Biotech Innovation Research Development and Consulting GmbH, Vienna, Austria) within a scientific collaboration project. Achaea used in this study were kindly provided by the research group of Dr Simon Rittmann, Archaea Physiology & Biotechnology, Archaea Biology and Ecogenomics Unit, University of Vienna) within a scientific collaboration project.

## 1. Bacterial Ghosts biodistribution

### 1.1. Intraperitoneal administration of Bacterial Ghosts

All animal procedures were approved by local ethics committee and are in accordance with the Austrian law for the protection of animals and the EU directive 2010/63/EU and conducted by Hemma Schüffl (Institute of Cancer Research, Medical University of Vienna).

Six Balb/c female mice, purchased from Janvier Labs, were used for this experiment. The mice were housed, under standardized pathogen-free conditions, in two separated filter cages IVC racks, type II-Lang 530 $cm^2$ purchased from EHRET Life Science Solutions (control mice were in a separated cage from the treated mice), and they had a 12/12 dark/ light cycle under 22 ± 1.0°C room temperature and 50 ± 10% constant humidity.

The bedding was purchased from Abedd, and the mice were fed with autoclaved food from SSNIFF Spezialdiäten GmbH, and autoclaved tap water ad libitum. The mice were not put on low fluorescence diet as no in vivo fluorescence imaging was planned.

All procedures were done under a laminar airflow cabinet from EHRET Life Science Solutions. On day 0, all mice (control and treated) were injected intraperitoneally with $1*10^5$ CT26-Luc cells (CT26 cells stably transduced with Firefly Luciferase gene, see Groza et al (2018). These cells were generated from CT-26 murine colon carcinoma cells (CRL-2638 purchased from ATCC) through retroviral transduction. On day 3, only the four treated mice were intraperitoneally injected with 6 mg/kg of the cytostatic drug Oxaliplatin purchased from LC Laboratories. On day 6, the treated mice were intraperitoneally re-injected with 6 mg/kg Oxaliplatin plus $4*10^8$ AF750 labeled Bacterial ghosts in 250 µl of Glucose. After two hours from injecting BGs, mice organs were removed (pancreas, uterus, stomach, part of intestine, caecum, and the suspected tumor tissues), without being imaged, and embedded in pre-labeled cryomolds filled with Tissue Tek® O.C.T™ Compound, purchased from Sakura Finetek Europe B.V. Urine samples were also taken through bladder puncture **(Table 1)**.

| Mouse ID | Strain | Gender | Treatment |
|---|---|---|---|
| **L699 I R (Ctrl)** | Balb/c mice | female | **Day 0:**<br>IP injection of $1*10^5$ CT26-Luc cells<br>**Day 3:**<br>IP injection of 6 mg/kg oxaliplatin<br>**Day 6:**<br>IP injection of 6 mg/kg oxaliplatin<br>After 2 h:<br>Organs sectioning and embedding + taking urine samples |
| **L699 I U (Ctrl)** | | | |
| **L699 II U** | Balb/c mice | female | **Day 0:**<br>IP injection of $1*10^5$ CT26-Luc cells<br>**Day 3:**<br>IP injection of 6 mg/kg oxaliplatin<br>**Day 6:**<br>IP injection of 6 mg/kg oxaliplatin + $4*10^8$ AF750 labeled BGs in 5% Glucose<br>After 2 h:<br>Organs sectioning and embedding + taking urine samples |
| **L699 II L** | | | |
| **L699 II R** | | | |
| **L699 II L+R** | | | |

**Table 1**. Details of CT26 tumor bearing mice injected intraperitoneally with AF750-BGs at the Institute of Cancer Research, Medical University of Vienna.

### 1.2. Preparing BGs positive control for Immunofluorescence

In order to support the validity of staining, it was essential to prepare a bacterial ghosts' positive control. The desired dilution of $8*10^5$ BGs in 50 µl suspension had been prepared by diluting the stock solution of 1,6* $10^{10}$ BGs/ml with distilled water.

24*24 coverslips 24x24 mm from Carl Roth GmbH + Co. KG, were marked on one side with AF (for Alexa Fluor labeled BGs), circled in the middle (approx. 20 mm diameter) and placed into the wells of the 6-well-plate.

After re-suspending the BGs prepared dilution, a 50 µl drop from this dilution has been centrally applied on each coverslip. This well-plate is carefully placed into the oven (without the lid) for about one hour at max. 60 °C to let it dry. The dried cover slips were then taken carefully out of the wells and placed, facing away from the sponge, two by two into an empty cover slip box, in a diagonal position. The box has been then marked and placed at -20 °C for further procedures.

### 1.3. Cryosectioning of organs

Cryostat, model: MNT from SLEE Medical GmbH, has been used in sectioning the Tissue Tek® O.C.T™ embedded organs in order to obtain 6 µm thick, frozen sections, ready for further fixation and staining procedures. After switching on cryostat it was very important to adjust the temperature on **-20 °C** ( sometimes on -22 **°C** during the hot weather on summer time), to switch the blade ( moving the blade to unused spot was not effective), and to wait 4-5 hours before beginning the sectioning process to ensure homogenizing the atmosphere of sectioning area. The light must be turned off while working with light-sensitive materials, such as the organs of mice treated with Alexa fluor labeled BGs.

During this time a styrofoam box with dry ice has been prepared to preserve the cryomold, that contain the frozen embedded organ, after taking it out of the **-80 °C** freezer. The cryomold has been placed then on the storage shelf into the cryostat for about 30 minutes, so that the frozen block reaches **c**, and the block has been pressed then out of the cryomold and placed on the storage shelf again.

Tissue-Tek® O.C.T.™ compound were added to a pre-cooled stamp and frozen block was immediately placed onto the stamp, in a way that the surface is as even as possible for cutting regular and even sections. The stamp with the block were turned back, for few minutes, into the cryostat until the block was completely fixed.

Superfrost® plus microscope slides from Thermo Fisher Scientific Inc., were labeled in the meantime, with the number of the mouse, the name of the organ, and a number represents the order of sectioning. The stamp was inserted then into the specimen head. Using the hand wheel of cryostat, the frozen block has been moved manually until it reached the LPS Plasma blade low profile, with was purchased from SLEE Medical GmbH, so we could have been able to adjust the surface orientation of the block to the orientation of the blade in order to cut regular even sections. To simplify this step, it was possible to use the trim function in finding an even level, and taking up the first sections on normal slides to check approaching the beginning of the tissue, as soon as the tissue appeared, we have continued carefully grabbing and pulling the edge of the approached section using a thin brush and gently pressing a SuperFrost® plus slide onto the section to gather it up. Each slide, with two organ sections, has been transferred right away into the styrofoam box with dry ice. Sometimes it was possible to change the temperature and the cut settings in order to acquire better sections. While sectioning the uterus, which is surrounded by a lot of fat tissue, and the ovaries, it was possible to turn the temperature to -25 °C and the cut settings to 10 µm to avoid getting holey tissue sections.

### 1.4. Ice Nucleation Protein Immunofluorescence staining of cryosections

Before each INP immunofluorescence stain of cryo sections, it was necessary to darken the staining chamber from the outside with aluminium foil, and create a humid atmosphere inside it using paper towels wetted with distilled water. After transferring the chamber under the hood, the selected slides have been defrosted in the humid chamber and the positive control in a 6-well-plate for approximately 5 minutes, without letting them dry (the tissue should not whiten). The tissue sections were then circled from the bottom of the slide with a solvent-proof fine liner, to better visualize the location of tissue sections.

The fixation step is crucial in preserving cells and tissue components for further staining processes. In order to ensure a proper fixation of tissue sections, 4% PFA, paraformaldehyde 4% in HBS-Buffer pH: 7,4 which was prepared in MMCT lab, had been applied for 15 minutes on tissue sections. The tissue sections should be completely covered with 4% PFA and the stopwatch should be started from the first drop on. While applying it, the drop should never be directly applied on tissue sections. We have always tried to apply the solution from the side of the slide. During this time the blocking buffer should be prepared. After 15 minutes from applying the solution, the slides had been taken one by and let them drain by dabbing them carefully onto paper towels. The slides had been washed then two times, each time for five minutes, with PBST (prepared in MMCT lab from mixing Dulbecco's phosphate buffered saline with 0.1% Tween 20 for molecular biology purchased from AppliChem GmBH). After applying PBST for the second time, the humid chamber was transferred to a working place outside the hood. The slides had been taken then one by one and let them drain by dabbing them carefully onto paper towels. The remained liquid around the tissue sections had been always wiped away and then the tissue sections were circled using a hydrophobic pen. According to the original SOP, written by Diana Groza, one of the two tissue sections on each slide had chosen to be the negative control. Because of the improper separation sometimes, using the hydrophobic pen, and the possibility of contaminating negative control sections with primary antibodies during washing steps, the negative control sections had been manipulated on separated slides. After circling the tissue sections with hydrophobic pen, the slide had been washed two times, each time for five minutes, with PBST.

Blocking step is after that crucial to avoid the interference of background signals, that is why **50 µl** of blocking buffer (PBST + 5% goat serum; Normal Goat Serum from Vector Laboratories Inc.) were applied on each tissue section for 45 minutes, to ensure a proper blocking. After blocking step, the tissue sections were incubated each with **50 µl** of primary antibodies serum; Rabbit serum to INP no. 2 second immunization purchased from BIRD-C GmBH (The serum of primary antibodies was diluted in a ratio of 1:50 with PBS, plus adding 5% goat serum). Tissue sections were incubated with primary antibodies for one hour at room temperature. The slides with negative control sections were treated with the same solution just without the primary antibodies serum (PBS with 5% goat serum). During this time, the secondary antibodies solution could be prepared, by diluting the secondary antibodies (Anti-rabbit-IgG-FITC-antibody produced in goat from Sigma-Aldrich, ) in a ratio of 1:400 with PBS, mixed with a 1:500 dilution of WGA-Rhodamine, which was just used for the staining but was not imaged, from Vector Laboratories Inc., with PBS, and finally 1% goat serum).

After the incubation with primary antibodies for one hour, the tissue sections had been washed three times, each for five minutes with PBST, and were then incubated, for one hour at room temperature, with **50 µl** of secondary antibodies solution applied on each tissue section. This step followed by washing the slides three times, each for five minutes, with PBST.

The final main step was staining the cells with DAPI solution, which was achieved by incubating each tissue section with **50 µl** DAPI solution (1:1000 dilution of DAPI stock solution 1 mg/ 1 ml from Sigma-Aldrich, with PBST) for 10 minutes at room temperature. The slides were then washed for three minutes with PBST, and then rinsed one by one for one minute in a beaker or staining jar filled with distilled water. The slides were then dried by dabbing them carefully one by one onto paper towels. After ensuring the complete dryness of the slides, around **6-10 µl** of mounting medium (VectaShield for FL) were applied then onto each tissue section, which were covered then with 24*50 mm coverslip. During the last covering step, it was important to make sure that there were no bubbles under the coverslip, especially where the tissue is located. The coverslips were then sealed with the slides using transparent nail polish, dried for approximately 30 minutes in a dark place, and finally placed into a box and stored in the fridge at **4°C (Table 2)**.

| **Procedure** | **BGs positive control and organs' tissue sections** | **Negative control** |
|---|---|---|
| **Defrosting** | Defrosting the slides in dark and humid chamber and the positive control in 6-well plate. | |
| **Encircling** | Encircling the tissue sections with a solvent-proof fine liner from the bottom of the slide. | |
| **Fixing step** | Fixation with 4% PFA for 15 min. | |
| **Washing step** | Washing two times, each for 5 min, with PBST. | |
| **Hydrophobic encircling** | Encircling the tissue sections with hydrophobic pen. | |
| **Washing step** | Washing two times, each for 5 min, with PBST. | |
| **Blocking step** | incubation with blocking buffer (PBST + 5% goat serum), for 45 min. | |
| **Primary Antibodies** | Incubation with primary antibodies serum for 1 hour (Rabbit serum to INP diluted 1:50 with PBS + 5% goat serum). | Incubation with PBS + 5% goat serum (without primary antibodies) for 1 hour. |

| | |
|---|---|
| **Washing step** | Washing three times, each for 5 min, with PBST. |
| **Secondary Antibodies** | Incubation with secondary antibodies serum (1:400 dilution of secondary antibodies, and 1:500 dilution of WGA-Rhodamine with PBS and 1% goat serum) for 1 hour. |
| **Washing step** | Washing three times, each for 5 min, with PBST. |
| **DAPI staining** | Incubation with 1:1000 dilution of DAPI stock solution with PBST for 10 min. |
| **Washing steps** | Washing with PBST for 3 min, followed by washing with distilled water for 1 min. |
| **Covering and sealing steps** | Applying **6-10 µl** of mounting medium onto each tissue section, covering them with cover slip and sealing them with nail polish. |
| **Storing** | After letting them dry, the slides were placed in a box and stored in the fridge at **4°C**. |

**Table 2.** INP Immunofluorescence staining steps for BGs' positive control, organs' tissue sections and negative control.

### 1.5. INP Immunofluorescence stain of BGs positive control

INP immunofluorescence staining for positive control (previously described bacterial ghosts' positive control) should be carried out simultaneously to the staining of cryosections. The positive control slips were carried out of the freezer **-20 °C** and placed in Cellstar® 6-well-cell-culture plate, sterile, with lid purchased from Sigma-Aldrich. The empty space of well-plate was filled with water, in order to insure a humid atmosphere, and the positive control slips were let thawing for approximately 5 minutes. Once they had reached the room temperature, 4% PFA was added onto the slips for 15 minutes to fix them. The rest of the steps were carried out exactly like in staining cryosections, and ended with drying the back of the slip, applying **5 µl** Vectashield on a prepared slide and covering it with the positive control slip **(Table 2)**.

## 1.6. Determining the optimal exposure time for BGs´ Imaging by using ‚artificial positive control‘

Although BG’s positive control was available during each staining and imaging round, tissue’s background was always a problem. In order to confirm the certainty of BGs’ AF750 emission results (detected through Cy7 channel) and to cancel the possible overlapping with tissue’s background), it was essential to optimize the imaging’s exposure time. For this purpose, artificial positive controls were constructed, by which BG’s were placed under and above tissues’ cryosections, INP immunostained, imaged and then compared with negative controls (tissue’s cryosections from the same organs, treated the same as artificial positive control without applying BG’s suspension).

### 1.6.1. Documenting the exposure time for imaging BG’s localized on tissue’ cryosections

In order to optimize the imaging’s exposure time of BG’s localized on the organs’ cryosections, pancreas from a previous experiment was selected (from MCT 274, a negative control tumor bearing mouse from Nadine Follrich’s experiment), cryosections from this pancreas were taken on SuperFrost® plus slide (two sections on each slide, exactly under the same conditions described earlier). 50µl of BG’s suspension (1/100 and 1/1000 dilutions from the same stock solution of 1,6* $10^{10}$ BGs/ml with distilled water) were applied on organs’ cryosections. The slides were then placed in oven at max 60 °C for almost 5 min. After drying step, cryosections with BG’s were INP immunofluorescent and DAPI stained and fluorescently imaged and saved. The exposure time used for each magnification was reported and the results were compared with negative control tissue’s sections.

### 1.6.2. Documenting the exposure time for imaging BG’s localized under tissue’s cryosections

In order to optimize the imaging’s exposure time of BG’s localized under the organs’ cryosections, 50µl of BG’s suspension (1/100 and 1/1000 dilutions) were applied on SuperFrost® plus slide. The slides were then placed in oven at max 60 °C for almost 5 min. After drying step, pancreas from a previous experiment was selected (from MCT 274, a negative control tumor bearing mouse from Nadine Follrich’s experiment), cryosections from this pancreas were taken on these slides (two sections on each slide, exactly under the same conditions described earlier). The cryosections with BG’s were INP immunofluorescent and DAPI stained and fluorescently imaged and saved. The exposure time used for each magnification was reported and the results were compared with negative control tissue’s sections.

### 1.6.3. Comparing artificial positive controls’ results with negative control

Negative control slide was prepared also from MCT 274 pancreas following the previous steps and conditions described under “Cryosectioning of organs and Ice Nucleation Protein Immunofluorescence staining of cryosections”, without applying BG’s suspension. Using Olympus IX73 inverted microscope from Olympus Company, equipped with a light source optimized for NIR imaging, suitable fluorescence filter pairs, along with OLYMPUS cellSens Standard software, the negative control slide was placed on the slide holder. After choosing Cy7 channel and selecting the desired magnification, a previously saved image from the artificial positive controls was opened, and its imaging settings were reloaded in order to capture a snapshot for the negative control under the same exposure time (through choosing “reload settings”) and adjustment range.

## 1.7. Imaging of INP Immunofluorescence stained tissue sections and positive control

Imaging step was the most critical step in our work, which can show both the positive results and the mistakes from previous steps. Olympus IX73 inverted microscope from Olympus Company was used for this purpose, along with OLYMPUS cellSens Standard software. In order to optimise the credibility of our results, it was important to use the same criteria to image both the positive control and our samples.

After sterilizing the place of work, the prestained slides were taken out of the fridge. The microscope and PC were switched on and cellSens software was opened. The positive control slide was put on the slide holder and 10X magnification was chosen. It was easier to observe firstly the areas where Anti-rabbit-IgG-FITC-antibodies bind, mainly to primary antibodies bound to bacterial Ice Nucleation Protein, using FITC channel. By activating “live” button, the sample could be observed on the computer screen. A photo for the desired place was captured, adjusted, saved as TIFF and exported. AF750 labeled BGs were observed using Cy7 channel.

It was critical to adjust the exposure time while imaging BGs (around 1.5s on 10X magnification, which was determined according to the results of imaging the artificial positive control) to avoid the negative background effect. The same steps of capturing a photo, adjusting the background and saving the picture were repeated, and finally, both FITC and Cy7 channels were merged and saved. The same steps were then repeated for each of 20X, 40X, and 60X (with the use of immersion oil, Type F Immersion liquid from Leica Microsystems CMS GmbH).

The same steps used to image BGs' positive control were followed to image the tissue samples, plus imaging the DAPI stained tissue with DAPI channel and then merging all of DAPI, FITC and Cy7 channels and saving the pictures.

In order to confirm the certainty of Cy7 results (to cancel the possible overlapping with background), they were compared with pre-stained tissue samples from control mice (not treated with AF750), through imaging them using the same settings (reload settings).

## 2. Archaea infiltration Project

### 2.1. Cell Seeding for cultivation of spheroids

#### 2.1.1. Cell splitting

The following procedure had been carried out in "S1 lab (Narnia lab)" which is considered as S1 cell culture lab. All experiments were done under the hood in strictly sterile conditions. To maintain laminar air flow, the hood sash was closed to proper position. The hood was sterilized with 70% ethanol and supplied with the needed and sterilized Serological Pipettes 5 ml, 10 ml, 25 ml purchased from Sarstedt, Pipette Controller (accu-jet® pro) from Brandtech Scientific Inc., Eppendorf Research ® plus micropipettes from Eppendorf, Pipette Tips from Nerbe plus GmBH, Centrifuge Tube 15 ml, 50 ml from Starlab International GmBH, Eppendorf Tubes from Nerbe plus GmBH, Haemocytometer Neubauer improved from Paul Marienfeld GmBH & Co. KG, Corning® COSTAR® Ultra-Low Attachment 96-well-plate from Corning Incorporated, TC Flask T75, Stand., Vent. Cap from Sarstedt, beaker (to collect the waste), lab marker, and calculator.

All reagents and growth mediums were prepared before start working with the cells. Their containers were sterilized using 70% ethanol, to prevent microbial growth in the cell culture, and placed in sterile and **37 °C** warmed water bath purchased from Linder Labortechnik, Labor- und Industriegeräte. Dulbecco's Modified Eagle's Medium/ Nutrient Mixture, F-12 Ham, with 15 mM HEPES, from SIGMA-Aldrich, was used as a growth medium for CT-26 luc *in vivo* cell line. 50 ml of the growth medium were removed from the bottle and substituted with 50 ml of 10% heat inactivated FCS from Biowest company, 5 ml L-Glutamine 200mM and 5 ml Penicillin-Streptomycin from Sigma-Aldrich.

T-75-flask, with the running CT-26 Luc "*in vivo* cell-line" (the same cells used earlier in the experiment done in Institute of Cancer Research, Medical University of Vienna), were taken out of the incubator, which optimizes cells growth under **37 °C** and 5% $CO_2$, the viability of the cells had been checked under the microscope, and then transferred to the workplace under the hood. The old medium were removed using 10 ml serological pipette and discarded in the beaker. 5 ml of Dulbecco's phosphate buffered saline (DPBS) from Sigma-Aldrich, were pipetted in the corner of T-75-flask, and the cells were washed by tilting the flask. The same pipette was used to remove the PBS and discard it in the beaker. This washing step was crucial to remove the remained medium, cells debris and dead cells, and to support the function of Trypsin. 2 ml of detaching reagent, Trypsin-EDTA Solution 1x from Sigma-Aldrich, were pipetted onto the cells and the flask was tilted carefully so that it covers the whole cell monolayer. This flask was placed then in Incubator 5 % $CO_2$, 37 °C, HERACELL VIOS 160i from Thermo Fisher Scientific Inc., and incubated for 4 minutes. The flask was then taken out of the incubator and tapped with hand in order to detach the cells. This could be checked under the microscope (Motic® AE31) from Motic Deutschland GmBH.

The cells were flushed with 3 ml of growth medium. The whole bottom was flushed in order to get as many cells as possible. At this point, the T-75-flask contains approximately 5 ml suspension, including 2 ml Trypsin and 3 ml medium. These 5 ml were transferred into CT-15, which was placed into the centrifuge (3K30) from Sigma Laborzentrifugen GmBH, to be centrifuged for 5 minutes. In order to get a properly separated cell pellet, the CT-15 should be left in the centrifuge for 3-5 minutes. The supernatant was then removed carefully with 5 ml serological pipette. Using the pipette, 1 ml of growth medium was added to the pellet, which was resuspended by pipetting the medium quickly, up and down, a few times, until the cell suspension appeared regularly turbid and no cell clumps were visible.

For further cultivation processes, a new T-75-flask was labeled with the name of cell line, split ratio, date and passage number. The flask was placed into flat position and filled with 12 ml growth medium. The cells in CT-15 were resuspended and **100µl** from this suspension were pipetted into the fresh medium. The flask was closed, tilted in a way that the medium covered the whole bottom, and placed into the incubator.

### 2.1.2. Cell counting

CT-15 was filled up to 5 ml to get a higher dilution and facilitate the process of cell counting. After that, the hemocytometer was prepared, by covering the contact points between the chamber and the coverslip with 70% ethanol and pressing the coverslip onto the chamber until Newton’s rings were visible. **15 µl** of cell suspension were added to each chamber of the hemocytometer. Each one of these chambers holds **0.1 µl** of cell suspension. The cells were counted under the microscope, by counting the cells in the four big squares of each chamber and calculating the mean. The number of the cells was 125 cells/ **0.1 µl**, which equals 1250000 cells/ ml and 6 250 000 cells/ cell pellet after multiplying it with 5, which represents the dilution factor.

### 2.1.3. Cell seeding

96-well-plate (COSTAR® Ultra-Low Attachment, Round Bottom, Polystyrene, purchased from Corning Incorporated, was recruited in cell seeding. Starting from the total number of cells we had, 6 250 000 cells/ cell pellet, the seeding number was calculated and the cell suspension was diluted in order to get 6 ml of cell suspension with concentration of **10 000 cells / 200 µl**, sufficient to seed 30 wells, and 6 ml of cell suspension with concentration of **5000 cells / 200 µl** sufficient to seed another 30 wells, each with **200 µl**.

96-well-plate was marked with the cell line, the cell cultivation zone with initial concentrations and the date. The adjacent wells (the border wells) were filled up with PBS, and the rest of the wells were seeded with cell suspension as decided beforehand in the well-plate template. The well-plate was closed with the lid and placed in the incubator. The well-plate was checked after few hours, which is a sufficient period for spheroids formation, and the spheroids were clearly visible.

The spheroids were grown in “S1 lab (Narnia lab)” for 7 days. During this period, the growth medium had been changed every day by removing **100 µl** from the old medium in each well and substituting them with a same quantity from the fresh medium. After these 7 days, the well-plate was transferred to BacLab for further inoculation with Archaea **(Table 3)**.

| **Time Interval** | **The Procedure** |
|---|---|
| **At the first day** | splitting, counting and seeding the running CT-26-Luc cell-line |
| **Till day 6** | Changing spheroids' growth medium. |
| **On day 7** | Inoculation with Archaea |
| **On day 8** | Harvesting and prefixation of spheroids 24h. |
| **On day 9** | Embedding of single spheroids 24h |
| **On day 12** | Harvesting and prefixation of spheroids 120h. |
| **On day 13** | Embedding of single spheroids 120h |
| **On day 14** | Harvesting and prefixation of spheroids 168h. |
| **On day 15** | Embedding of single spheroids 168h |
| Cryosectioning of spheroids, DAPI staining and imaging. | |

**Table 3.** Ttimeline of the steps followed in Archaea CT26-derived spheroid co-culture project, started from CT26-Luc cells splitting ending with DAPI stained spheroids' cryosections imaging.

## 2.2. Co-culture with Archaea: Preparation of Archaea suspension & Inoculation of spheroids with (AF488-prelabeled) Archaea

### 2.2.1. Preparation of Archaea suspensions for inoculation

This part of the project was carried on in "BacLab", which is supplied with the needed equipment to safely and properly deal with Archaea. The lab is supplied with an incubator / drying cabinet (WTB Binder) from BINDER GmbH, Vortex mixer purchased from IKA Labortechnik, IKA®-Werke GmbH & Co. KG, shaker (Thermo Scientific™ MaxQ™ 4450 Incubated Shaker) from Thermo Fisher Scientific Inc., and centrifuge (VWR Microstar 17R) from VWR International.

The 96-well-plate was transferred into BacLab and placed in the incubator under **37 °C** and no $CO_2$. A bottle of Methanococcus maripaludis Archaea S0001 suspension, which is able to undergo genetic engineering, received from Barbara Reischl, Department of Ecogenomics and

Systems Biology, University of Vienna. Methanococcus maripaludis is mesophilic, fast growing, hydrogenotrophic archaebacteria. The optimal temperature for the growing of this nonpathogenic, strictly anaerobic microbe is 38 °C, which insures a doubling time of 2 hours. This microorganism does not need complex carbon substrates to insure their growth. It considered to be a renewable source of H2, capable on capturing and converting CO2 into methane via Wolfe cycle (Jones & Paynter, 1983).

Checking the concentration of Archaea suspension had been carried out there, to be $1*10^9$ Archaea/ ml, and the bottle was brought directly to BacLab. The concentration of Archaea suspension was sufficient to carry out the experiment without the necessity of concentrating it. In order to inoculate the spheroids with Archaea, **40 µl** of Archaea suspension was planned to be added to each of the 48 wells (24 wells to be inoculated with Alexa-Fluor-488 labeled Archaea suspension, and 24 wells inoculated with unlabeled Archaea suspension as control. The total amount of Archaea suspension needed was **1920 µl**, half of them, **960 µl,** were labeled with Alexa-fluor-488, and the left **960 µl** were used without being labeled. An extra amount from Archaea suspension was added to the total amount, to be **2200 µl**, in case wasting something while working. As the viability for both suspensions of labeled and unlabeled Archaea needed to be rechecked after the labeling process, **100 µl** were added to the total amount to be **2300 µl**.

Using BD Luer-Lok$^{TM}$ 3 ml syringe (BD$^{TM}$ Syringe) from Becton Dickinson and Company, and Sterican® Standard Gr.17 G24 x 1", Ø 0,55 x 25 mm needle from B. Braun Melsungen AG, **2300 µl** were taken out of Archaea suspension, divided in two 1,5-ml-eppis, each with **1150 µl**. As we worked with anaerobic Archaea strain, we have tried not to expose them for too long periods to oxygen. All epis were opened immediately before going in with the pipette tip and closed right after we were done, and the same thing while handling the well-plate. In order to wash out the growth medium and resuspend the Archaea in PBS, the two eppis were centrifuged for 5 minutes under 6800 g. Most of the supernatant, **1100 µl**, were removed carefully from both epis, to not damage the dark pellet of Archaea, and equal amount of PBS was added to the epis again and the pellet was resuspended. This step had been repeated three times in order to insure the complete removal of the growth medium, which was handled to be yeast free. After the third time, the retained pellets were resuspended, each with **1100 µl** PBS, in order to get two eppis, each one with **1150 µl** for both labeled (marked with AA) and unlabeled (marked with AU) Archaea suspensions **(Table 3).**

### 2.2.2. Labeling of Archaea with Alexa-Fluor$^{TM}$ 488 NHS Ester (Succinimidyl Ester)

The Archaea suspension in the eppi marked with AA was treated with **31.05 µl** of Alexa-Fluor$^{TM}$ 488 NHS Ester (Succinimidyl Ester), purchased from Thermo Scientific (2,7 µl Alexa-Fluor$^{TM}$ 488 NHS Ester for each 100 µl Archaea suspension equals to 27µl/ml). The two eppis were then covered with aluminum foil (to protect the fluorescent dye from the effect of light), vortexed, and placed in a beaker onto the shaker. The incubation time lasted 4 hours, interrupted with vortexing every hour. The eppis were then centrifuged for 5 minutes under 6800 g. The supernatants, composed of PBS and Alexa-Fluor-488 surplus, were removed and substituted with equal amounts of PBS. The pellets were resuspended and centrifuged again. This step was repeated two times. The pellets were resuspended then with equal amounts of PBS.

Small specimen, around **10 µl**, was taken from each Archaea suspension and placed on a Superfrost® slides, cut edges, from Carl Roth GmbH + Co. KG, and covered with coverslip 24x50 mm from Carl Roth GmbH + Co. KG, to check under the microscope the presence of Archaea, the efficiency of staining, and to prove that unlabeled Archaea suspension do not show any auto-fluorescence. To check the viability of Archaea, **100 µl** from each Archaea suspension were resuspended in two 1.5-ml-eppis, each one was filled with **900 µl** Dulbecco's Modified Eagle's Medium/ Nutrient Mixture, F-12 Ham, with 15 mM HEPES from SIGMA Life Science, which was during cell splitting and seeding, and spheroids formation, to get **1000 µl** Archaea suspension with 1:10 dilution for both labeled and unlabeled Archaea. The eppis were sent to Barbara for further check **(Table 3).**

### 2.2.3. Inoculation of spheroids with Archaea

**40 µl** of Alexa-Fluor-488 labeled Archaea suspension were added to each of the 30 wells marked with AA, and **40 µl** from the unlabeled Archaea suspension were added to each of the 30 wells marked with AU. The rest of spheroids marked with UT kept untreated with Archaea. The well-plate was sealed with parafilm to maintain an anaerobic condition for the Archaea, and then cover with aluminum foil, to protect the fluorescent dye from the light, and placed in the incubator for further harvesting, pre-fixation and embedding procedures **(Table 3 & Figure1).**

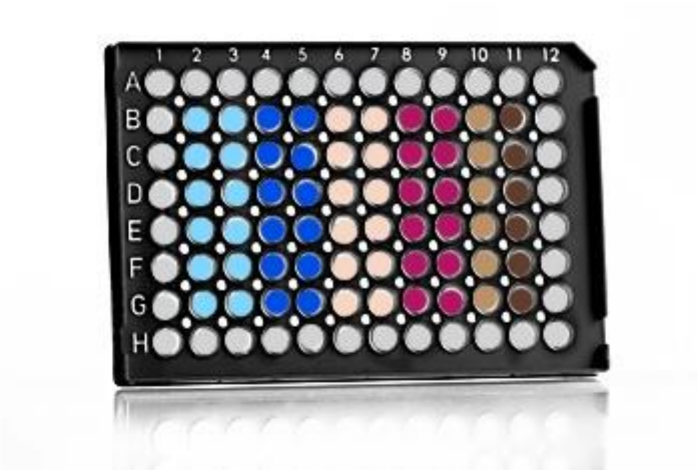

**Figure 1.**
The grey wells on the edges ○ filled with PBS, light blue wells ● (columns 2&3) contain AF488-labeled archaea-inoculated 5K spheroids AA, dark blue wells (columns 4&5) ● contain AF488-labeled archaea-inoculated 10K spheroids AA, pink wells ● (columns 6&7) contain Alexa-untreated archaea-inoculated 5K spheroids AU, violet wells (columns 8&9) ● contain Alexa-untreated archaea-inoculated 10K spheroids AU, beige wells ● (column 10) contain archaea-untreated 5K spheroids UT, brown wells ● (column 11) contain archaea-untreated 10K spheroids UT

## 2.3. Harvesting and pre-fixation of spheroids & Embedding of single spheroid into one cryomold

Morphological changes in spheroid sections were observed while comparing the sections fixed just onto the slides after spheroids sectioning, and the sections of spheroids fixed prior to the embedding and cryosectioning steps, which leads to more compact spheroid sections. These observations were based on a previous experiment done by the diploma student Tini Le in MMCT lab, which also noted the preference of embedding each spheroid into a separated cryomold, and not multiple-spheroids into one cryomold, to better differentiate the sections' sequencing for each spheroid (beginn, middle and end) **(Table 3).**.

### 2.3.1. Harvesting of spheroids

The procedure of harvesting and prefixation of spheroids and embedding them in cryomolds was carried out three time. The first time was after 24 hours from inoculating the spheroids with Archaea suspension (applied on the spheroids of rows B and C from the 96-well-plate, which include 4 AA spheroids 5K, 4 AA spheroids 10K, 4 AU spheroids 5K, 4 AU spheroids 10K, 2 UT spheroids 5K, 2 UT spheroids 10K). The second time was after 120 hours from inoculating the spheroids with Archaea suspension (applied on the spheroids of rows D and E from the 96-well-plate), and the third time was after 168 hours from inoculating the spheroids with Archaea suspension (applied on the spheroids of rows F and G from the 96-well-plate).

After 24 hours from spheroids inoculation with Archaea suspension, 1.5-ml-eppis were placed in a rack, and marked with cell seeding numbers (5K or 10K) of the 20 spheroids from rows B and C of the 96-well-plate, and each of the abbreviations AA for Alexa-Fluor-488 labeled Archaea, AU for unlabeled Archaea, and UT for untreated spheroids. The well-plate was taken then out of the incubator and placed inside the Laminar Air Flow to prevent the contamination of other spheroids. After the aluminum foil and parafilm were removed, the spheroids were transferred one by one to the prepared eppis, using a **1000-µl-**pipette. The well-plate was wrapped again with parafilm, covered with aluminum foil, and placed back in the incubator. The eppis were transferred then outside the LAF but kept under the hood, because of working with PFA, which is hazardous to health **(Table 3).**

### 2.3.2. Prefixation of spheroids

Using a pipette, the growth medium was removed from each eppi, and the spheroids were washed two times with **200 µl** PBS, and then one time with **200 µl** .Paraformaldehyde 4% in HBS-Buffer, pH: 7,4, which was prepared in MMCT lab. **200 µl** of PFA 4% were then added to each eppi, which were tightened up with parafilm and covered with aluminum foil. They were placed then into a box marked with “paraformaldehyde containing sample” and stored in the fridge at **4°C** for 24 hours. This box was taken, on the next day, out of the fridge and PFA 4% was removed using a pipette. The spheroids were washed three times with **200 µl** PBS and the eppis were filled again, each with **200 µl** PBS **(Table 3).**

### 2.3.3. Embedding of single spheroid into one cryomold

Cryomolds (Tissue Tek Cryomold® Intermediate, square 10X10X5 mm, from Sakura Finetek Europe B.V.) were marked exactly like the eppis and filled up to the half with Tissue Tek® O.C.T™ Compound, purchased from Sakura Finetek Europe B.V. The spheroids were transferred carefully, using a **1000-µl-**pipette, each one into separated cryomold. Each cryomold was then filled up fully with Tissue Tek® O.C.T™ Compound and placed into a box with lid. The box was stored in the freezer at **-20 °C**, because it was planned to section the spheroids after a short storage time (in 5-6 days). The smoothness of the blocks decreases with the time that is why it was optimal to section them after 2-3 hours from freezing them.

The same steps of spheroids harvesting, prefixation, and embedding in cryomolds were repeated after 120 and 168 hours from inoculating the spheroids with Archaea suspensions **(Table 3).**

### 2.4. Cryosectioning of the embedded spheroid

Cryostat, model: MNT purchased from SLEE Medical GmbH, has been used in sectioning the embedded spheroids. In order to obtain 6 µm thick, frozen sections, ready for further fixation and staining procedures. After switching on cryostat it was very important to adjust the temperature on **-20 °C** (it was necessary sometimes to switch the temperature from -20°**C** to -22 °**C** during the hot weather on summer time, as we got too sticky sections, and sometimes the temperature was changed to **-17 °C** while getting crumbled and brittle sections). The second crucial thing was switching the LPS Plasma blade low profile, which were purchased from SLEE Medical GmbH, before each sectioning. Moving the blade to unused spot was only effective when the sections were divided into the half, which reflects the worn of the blade at this point). Lastly, it was ideal to wait 4-5 hours before beginning the sectioning process to ensure homogenizing the atmosphere of sectioning area, and to turn off the light while working with light-sensitive materials, such as the spheroids inoculated with Alexa-Fluor-488 treated Archaea.

The cryomold that contains the frozen embedded spheroid was taken out of the **-20 °C** freezer and placed onto the storage shelf into the cryostat for short term acclimatization. After about one hour, the block was pressed out of the cryomold and placed on the storage shelf again.

Tissue-Tek® O.C.T.™ Compound, purchased from Sakura Finetek Europe B.V., were added to a pre-cooled stamp and the frozen block was immediately placed onto the stamp, in a way that the surface is as even as possible for cutting regular and even sections. The stamp with the block were turned back, for few minutes, into the cryostat until the block was completely fixed.

SuperFrost® plus microscope slides, purchased from Thermo Fisher Scientific Inc. Company, were labeled, in the meantime, with symbols like **AA** for the sections of spheroids inoculated with Alexa-Fluor-488 labeled Archaea, **AU** for the sections of spheroids inoculated with untreated Archaea, and **UT** for sections of the spheroids which were not inoculated with Archaea, and with the date, initial concentration and a number represents the order of sectioning, to distinguish the beginning, middle and the end of the spheroids. After proving the perfect fixation of the frozen block on the stamp, this stamp was inserted into the specimen head. Using the hand wheel of cryostat, the frozen block has been moved manually until it reached the blade so we could have been able to adjust the surface orientation of the block to the orientation of the blade in order to cut regular even sections. To simplify this step, it was possible to use the trim function, which cuts **10-15 µm** thick sections, in finding an even level, and taking up the first sections on normal slides to check approaching the beginning of the spheroid. As soon as the spheroid appears, the automatic cutting function was turned on, with a downward speed of **5 mm/s** and an upward speed of **24 mm/s**. The sections were carefully grabbed and the edge of the approached section was pulled using a thin brush, and a SuperFrost® plus slide was pressed onto the section to gather it up. This step was repeated till getting almost eight spheroids sections on each slide, following a specific pattern for placing the sections on the slide in a way that allows to track the spheroids shape from one end to the other. The slide, with the spheroids sections, was transferred right away into a slide-box. The sectioning was continued until no spheroid could be seen anymore. The slide-box was stored into the freezer at **-20 °C** for short term storage (4-5 days), and at **-80 °C** for longer storage periods **(Table 3).**

### 2.5. Post-fixation of spheroid sections & Staining spheroid sections with DAPI

The slides with spheroid sections were taken out of **-20 °C** freezer to let them thaw at room temperature for almost 5 minutes. They were placed then into a Kartell™ PMP Hellendahl Staining Jar purchased from Thermo Fisher Scientific Inc., and the rest of the experiment were done under the hood, as the jars were then filled up with 4% PFA, in order to fix the spheroids sections onto the slides and without being washed away afterwards. The fixation step with 4% PFA took 30 minutes. It is important to fix each type of spheroids in different jars. For example, the sections of spheroids inoculated with Alexa-Fluor-488 labeled Archaea should be fixed separately from other sections of the spheroids inoculated with unlabeled Archaea, as the dye could stain the unlabeled sections. After 30 minutes, PFA was discarded into an appropriate waste container and the slides were washed three times with PBS. The jar must be filled again with PBS, to ensure that the sections will not dry up.

The slides were taken then one by one out of the staining jar, the presence of spheroids sections was checked, and the sections were encircled with Histo Mark Pen purchased from Cedarlane Laboratories. For persistence humidification, the slides were then turned back into the staining jar with PBS. 1:500 dilution was prepared from DAPI 1 mg/ml stock solution, purchased from Sigma-Aldrich Company, after diluting if with PBS to get a DAPI-solution of a concentration of 2 µg DAPI / ml PBS. Using a pipette, the prepared DAPI solution was applied on the encircled spheroids sections in a dark box with a lid, because DAPI is light sensitive and the enclosed space prevents the evaporation of the applied solution. After incubation time between 20-30 minutes, DAPI solution was washed off by putting the slides back into the staining jars containing PBS and washing them five times with PBS. The slides were taken then one by one out of the staining jar and dabbed carefully on a tissue to let them drain.

Lastly, two drops of Vectashield® Antifade Mounting Medium, from Vector Laboratories Inc., were applied onto each slide and covered with coverslips. The mounting medium could be spread using a pipette tip and any surplus of it was blot off with a tissue. The coverslips were sealed with a transparent nail polish, kept for 30 minutes in a dark place to dry up, then placed into a 100 Place Premium Microscope Slide Box from Heathrow Scientific, and stored in the fridge at **4 °C** for further imaging steps **(Table 3).**

### 2.6. Imaging spheroid sections with fluorescence microscope (DAPI stained nuclei / AF488-labeled Archaea)

The spheroids were imaged using Olympus inverted microscope, model: IX73, from Olympus Company, and cellSens Standard software. Imaging process took place in S2 lab.

After taking the pre-stained slides out of the fridge, the microscope and PC were switched on, cellSens software was opened and the first slide was put on the slide holder. Through DAPI filter and 10X magnification, the entire slide was scanned in order to reach a suitable spheroid section. “Live” button was activated, the resolution was adjusted and a picture for the spheroid was captured, adjusted (to increase the intensity or reduce the background), and saved. Without moving the slide, FITC filter was used to image the AF488-labeled Archaea. A picture for FITC channel was captured, adjusted and saved. Finally, both DAPI and FITC channels were merged in one picture, so we could observe the allocation of Archaea in the spheroid, and this photo was also saved and exported.

The same steps were repeated to get similar pictures, for the same spheroid section, at 20X magnification, also, for each of the beginning, middle and end sections of the same spheroid and from different spheroids, which had been incubated with Alexa-Fl-488-stained Archaea for 24h, 120h and 168h).

# Results and discussion

## 1. Bacterial Ghost's Project

Because of the importance of Bacterial Ghosts in cancer treatment, a previous experiment performed, by Nadine Follrich in MMCT lab, aimed to investigate the localization of intraperitoneally injected, AF750-labeled BGs in both tumor bearing and non-tumor bearing mice. 2D fluorescence imaging FLI, for the organs taken out from both tumor bearing and non-tumor bearing mice after 24 hours from injecting BGs, detected signals in all of the pancreas, gastrointestinal tract, liver, kidneys and uterus, still in lower intensity than the signals detected in mice organs after 1-2 hours from injecting BGs. However, the signals of 2D fluorescence imaging from tumor bearing mice detected to be more associated with pancreas, pancreatic tumor and peritoneal tumor. In order to precisely detect the location of BGs, these organs were immediately embedded in Tissue-Tek® O.C.T.™ compound and stored in **-80 °C** freezer for further cryosectioning and INP immunofluorescence staining.

Olympus IX73 inverted microscope has been used in imaging the INP immunofluorescence stained tissue sections of tumor bearing mice organs. In order to confirm the presence of BGs, it was important to get an overlapping between the signal detected with the FITC filter pair, which detect the antibody-stained INP, and the signal detected with the Cy7 filter pair, which detect the AF750 labeled BGs. However, detecting BGs was also accepted through Cy7 only, and the certainty of the results (eliminating the false positive effect of background) was confirmed through comparing our results with pre-stained tissue sections from control mice (not treated with AF750), imaged using the same settings (through reload settings). Through imaging organ-sections of tumor bearing mice from Nadine's experiment (organs were taken from mice after 24h from injecting BGs), almost no BGs were found.

Because of the possible degradation of BGs through the immune system after 24h from injecting them, and to insure the BGs tumor association, this experiment was repeated in the Institute of Cancer Research, Medical University of Vienna, on six Balb/c female mice (4 treated with AF750 labeled BGs and 2 non treated mice). After injecting these mice with CT26-Luc cells, some tumor nodules were detected on the pancreas and mesentery in almost all mice **(Table 4).** The whole pancreas from each of the three BGs treated mice (L699 IIL, IIL+R, and IIU) was sectioned. Some cryosections were undergone both INP immunofluorescence and DAPI staining, and the other sections were stained just with DAPI.

| **Mouse ID** | **Strain** | **Gender** | **Suspected tumor** |
|---|---|---|---|
| **L699 I R (Ctrl)** | Balb/c mice | female | **1st** mesentery<br>**2nd** on the intestine |
| **L699 I U (Ctrl)** | | | **1st** pancreas<br>**2nd** mesentery |
| **L699 II U** | Balb/c mice | female | **1st** pancreas<br>**2nd** mesentery |
| **L699 II L** | | | **1st** pancreas<br>**2nd** mesentery |
| **L699 II R** | | | **1st** pancreas<br>**2nd** mesentery |
| **L699 II L+R** | | | **1st** pancreas<br>**2nd** mesentery |

**Table 3.** The types of tumor tissues developed in both treated and controlled mice as a result on injecting CT26-Luc cells.

### 1.1. Optimal exposure time for BGs´ Imaging by using ‚artificial positive control‘

Although BGs’ positive control (a sample of only bacterial ghosts) was essential during each immunofluorescent staining round for ice nucleation protein, to insure the proper staining and compare the positive signals detected in organs’ samples, it was not sufficient to insure the proper imaging of INP immunofluorescence stained organs’ cryosections. High organs’ autofluorescence was detected through Cy7 channels, which resembled AF750 emission. That is why it was essential to optimize the exposure time used in imaging AF750-labeled BGs to cancel the effect of organs’ autofluorescence. In order to apply that, artificial positive controls from tumor bearing mice not treated with AF750-labeled BGs was constructed as described earlier. Bacterial ghosts’ suspensions of different dilutions (1/100 and 1/1000) were applied on and under organs’ cryosections on separated slides. The prepared samples were then INP immunofluorescence and DAPI stained and fluorescently imaged. The exposure time used in imaging the artificial positive controls through Cy7 channel was increased gradually till the appearance of the first positive signal of AF750 emission. The exposure time was detected in four locations from each slide, at different magnifications, and listed in four tables.

Exposure times used to detect NIR emission of 1/100 and 1/1000 diluted, AF750 labeled BGs’ suspensions, located on pancreatic cryosections in four different locations from each of the prepared artificial positive control**s** were listed in tables 4 and 5 respectively. The most important data were those collected at 10X magnification, which were almost the same which used to image BGs positive control, except of the relatively lower exposure time detected in the fourth location from table 4, as they were clumps of BGs of higher emission, required lower exposure time to be detected.

| Cy7 | 1st location | 2nd location | 3rd location | 4th location |
|---|---|---|---|---|
| **10X** | 1100ms | 990ms | 987ms | 573ms |
| **20X** | 575ms | 573ms | 794ms | 333ms |
| **40X** | 150ms | 158ms | 194ms | 242ms |
| **60X** | 53ms | 53ms | 59ms | 102ms |

**Table 4.** The exposure time used to detect NIR emission of 1/100 diluted, AF750 labeled BGs’ suspension, located on pancreatic cryosections in four different locations from the prepared artificial positive control. (ms; millisecond)

| Cy7 | 1st location | 2nd location | 3rd location | 4th location |
|---|---|---|---|---|
| **10X** | 1,5s | 1100ms | 1100ms | 1100ms |
| **20X** | 900ms | 800ms | 575ms | 575ms |
| **40X** | 516ms | 516ms | 374ms | 270ms |
| **60X** | 140ms | 140ms | 157ms | 155ms |

**Table 5**. The exposure time used to detect NIR emission of 1/1000 diluted, AF750 labeled BGs' suspension, located on pancreatic cryosections in four different locations from the prepared artificial positive control. (s; second, ms; millisecond)

Exposure times used to detect NIR emission of 1/100 and 1/1000 diluted, AF750 labeled BGs' suspensions, located under pancreatic cryosections in four different locations from each of the prepared artificial positive control**s** were listed in tables 6 and 7 respectively. This step (applying BGs' suspensions under organs cryosections) was more important than applying BGs' suspensions on the organs cryosections, to clearly detect the interference of tissue autofluorescence through fluorescence imaging.

| Cy7 | 1st location | 2nd location | 3rd location | 4th location |
|---|---|---|---|---|
| **10X** | 1s | 1,5s | 1100ms | 1100ms |
| **20X** | 573ms | 800ms | 575ms | 575ms |
| **40X** | 375ms | 516ms | 374ms | 375ms |
| **60X** | 137ms | 157ms | 140ms | 137ms |

**Table 6.** The exposure time used to detect NIR emission of 1/100 diluted, AF750 labeled BGs' suspension, located under pancreatic cryosections in four different locations from the prepared artificial positive control. (s; second, ms; millisecond)

| Cy7 | 1st location | 2nd location | 3rd location | 4th location |
|---|---|---|---|---|
| **10X** | 1100ms | 1200ms | 1100ms | 1,5s |
| **20X** | 575ms | 800ms | 575ms | 900ms |
| **40X** | 375ms | 437ms | 375ms | 516ms |
| **60X** | 140ms | 157ms | 137ms | 157ms |

**Table 7.** The exposure time used to detect NIR emission of 1/1000 diluted, AF750 labeled BGs' suspension, located under pancreatic cryosections in four different locations from the prepared artificial positive control. (s; second, ms; millisecond)

In summary, the most important exposure time used to detect NIR emission of AF750-labeled BGs in all of the prepared BGs positive controls and artificial positive controls was between 1.5-2 seconds at 10X magnification, and there were almost no differences in imaging BGs in different localizations in organs' cryosections. However, the signals detected through higher exposure time and especially on 5s were just tissues' background.

### 1.2.Imaging BGs positive control

The first step in each imaging round was imaging BGs positive control, which underwent the same treatment as for INP immunofluorescence stained organs cryosections. Positive control samples were imaged using Cy7 filter (which detects the NIR emission of AF750) and FITC filter (which detects the immunostaining of bacterial ghosts; The areas where Anti-rabbit-IgG-FITC-antibodies bind, mainly to primary antibodies bound to bacterial Ice Nucleation Protein), at different magnifications. Finally, these two channels, from each magnification, were merged and the overlapping between the green (FITC channel) and red (Cy7 channel) colors confirmed the proper staining and the positive presence of bacterial ghosts **(Figure 2).**

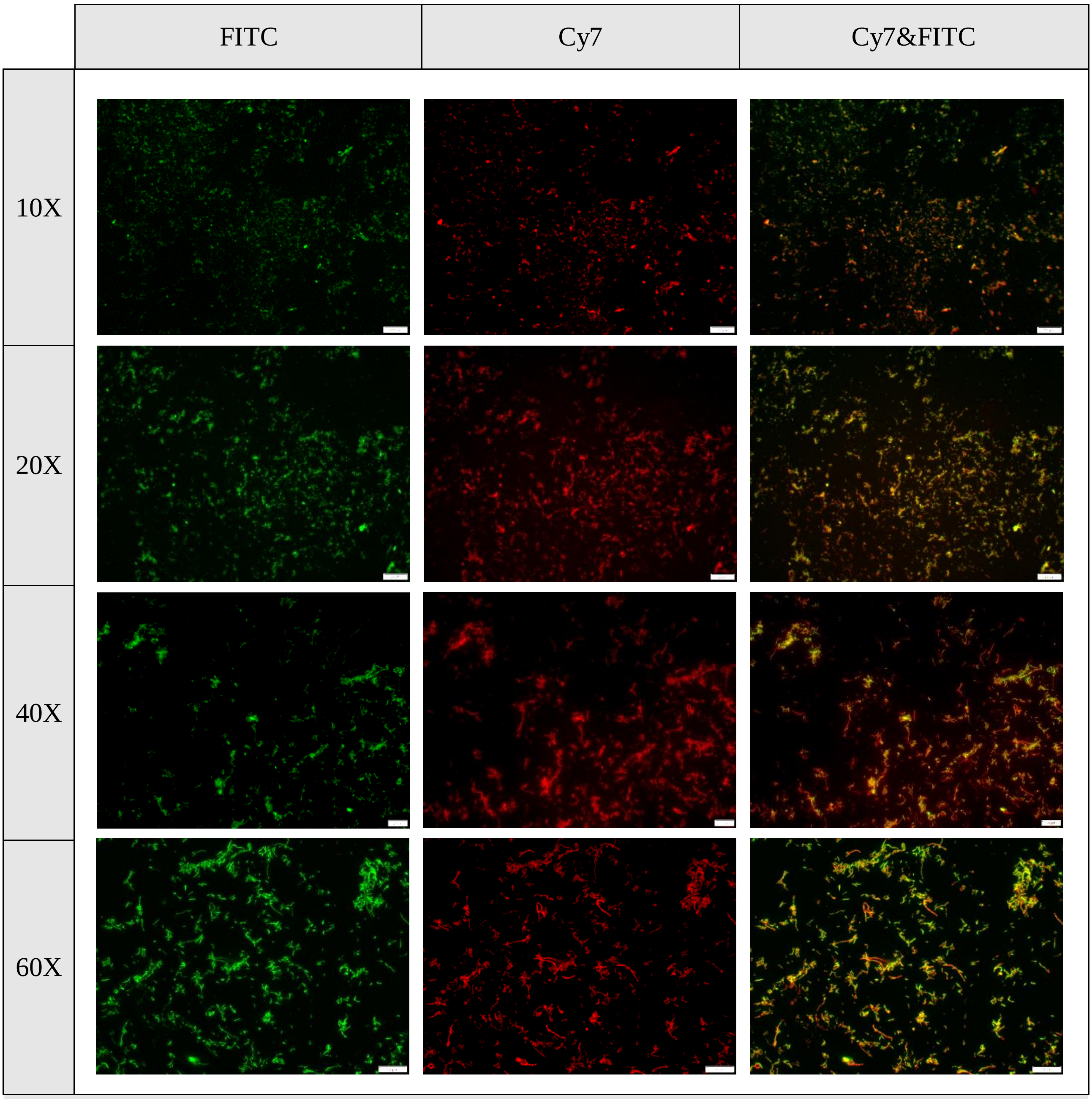

**Figure 2.** Fluorescence microscopy images of AF750-labeled bacterial ghosts' positive control showing immunofluorescence staining of ice nucleation protein, detected through FITC channel (left column), which observes firstly the areas where Anti-rabbit-IgG-FITC-antibodies bind, mainly to primary antibodies bound to bacterial Ice Nucleation Protein. Cy7 channel (middle column) detects the emission from the direct labeling of BGs with AF750 dye. Cy7&FITC (right column) represents an overlay of both emissions. The sample was imaged at different magnifications; 10X (scale bar 100µm), 20X (scale bar 50µm), 40X (scale bar 20µm) and 60X (scale bar 20µm).

### 1.3. Imaging pancreas cryosections

After sectioning the whole pancreas from mouse L699 IIL (CT26-Luc tumor bearing mouse, treated with AF750-labeled BGs on day 6 from tumor growth, and this pancreas was taken out of the mouse two hours after intraperitoneally injecting BGs), some cryosections, from begin, middle and end locations, were INP immunofluorescence and DAPI stained and other sections were just DAPI stained. BGs were detected in the middle part of this pancreas, based on the overlapping between Cy7 and FITC channels, which detected their localization on the surface of this organ. **Figure 3** illustrates BGs attachment on the surface of pancreas, imaged at 10X, 20X and 60X magnifications. The merge channels of Cy7 and DAPI are sufficient to positively insure the presence of AF750 labeled BGs. However, these results were confirmed after the complete overlapping between Cy7 and FITC channels.

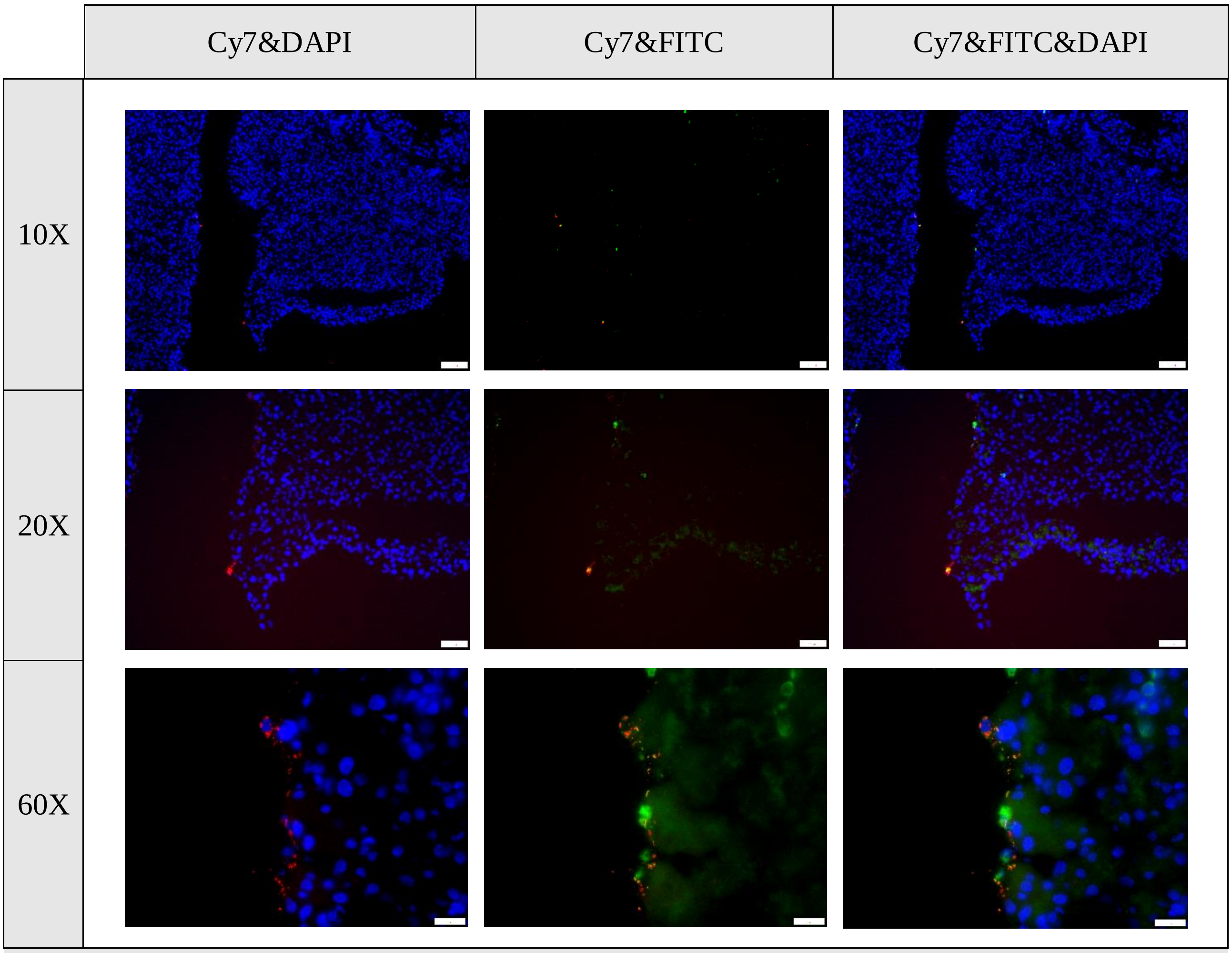

**Figure 3**. Fluorescence microscopy images of the DAPI stained pancreatic cryosection from CT26-Luc tumor bearing mice, which was taken out from mouse L699 IIL after two hours from intraperitoneally administrating AF750-labeled BGs on day 6 from tumor growth. The tissue cryosection was imaged at different magnifications; 10X (scale bar 100µm), 20X (scale bar 50µm) and 60X (scale bar 20µm). Cy7 and DAPI merge channels (left column) illustrate the alignment of AF750 labeled BGs on the surface of pancreatic tissue. Cy7 and FITC merge channels (middle column) illustrate the overlay between AF750 emission and immunofluorescence staining of ice nucleation protein. Cy7, FITC and DAPI merge channels (right column) represent the final results.

Another tissue cryosection from the middle part of the same pancreas (from mouse L699 IIL) was stained just using DAPI, and the obtained results were sufficient to confirm the positive presence of AF750-labeled BGs as they could be observed through Cy7 channel which detects the AF750 NIR emission, on exposure time of almost 1.5 s (which is sufficient to detect AF750 signals without the interference of tissue's background, as discussed earlier) at 10X magnification and compared with negative control sections **(Figures 4).** Further imaging at 60X magnification shows the precise shape of BGs **(Figure 5).**

| | 1st Location | 2nd Location | 3rd Location |
|---|---|---|---|
| 10X | 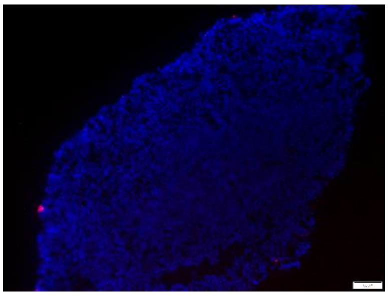 | 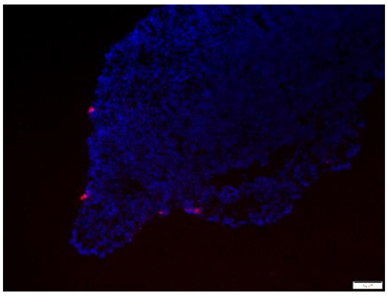 | 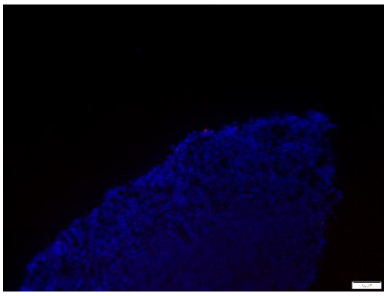 |

**Figure 4.** Fluorescence microscopy images of the DAPI stained pancreatic cryosection from CT26-Luc tumor bearing mice, which was taken out from mouse L699 IIL after two hours from intraperitoneally administrating AF750-labeled BGs on day 6 from tumor growth. FLM images illustrate the presence of AF750 labeled BGs in three locations surrounding the pancreas at 10X magnification (scale bar 100µm).

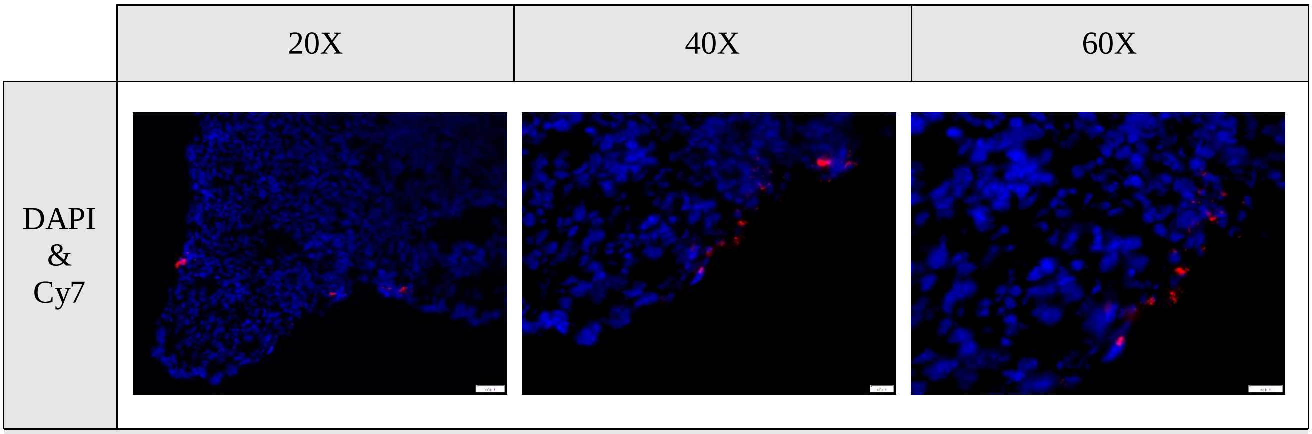

**Figure 5.** Fluorescence microscopy images of the second location from figure 4 at 20X (scale bar 50µm), 40X (scale bar 20µm) and 60X (scale bar 20µm) magnifications, in order to precisely observe the shape of BGs.

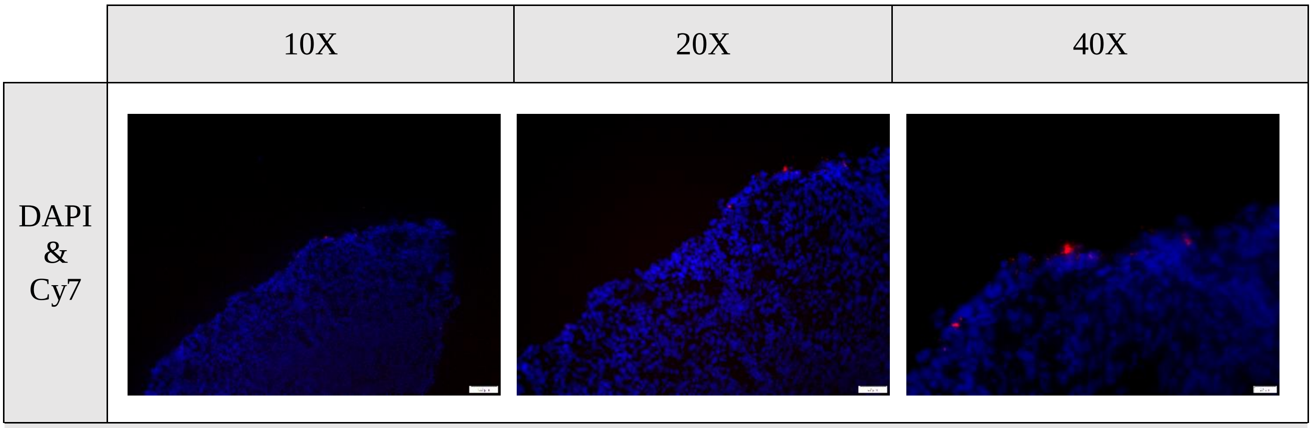

**Figure 6.** Fluorescence microscopy images of the third location from figure 4 at 20X (scale bar 50µm), 40X (scale bar 20µm) and 60X (scale bar 20µm) magnifications.

INP immunofluorescence staining for junction locations in the middle part of the same pancreas (from mouse L699 IIL) demonstrated the localization of BGs on these surfaces in different locations. **Figure 7** represents one of these locations, imaged at 40X and 60X magnifications, and **figure 8** illustrates Cy7 and DAPI merge channels of the same location at 20X, 40X and 60X magnifications.

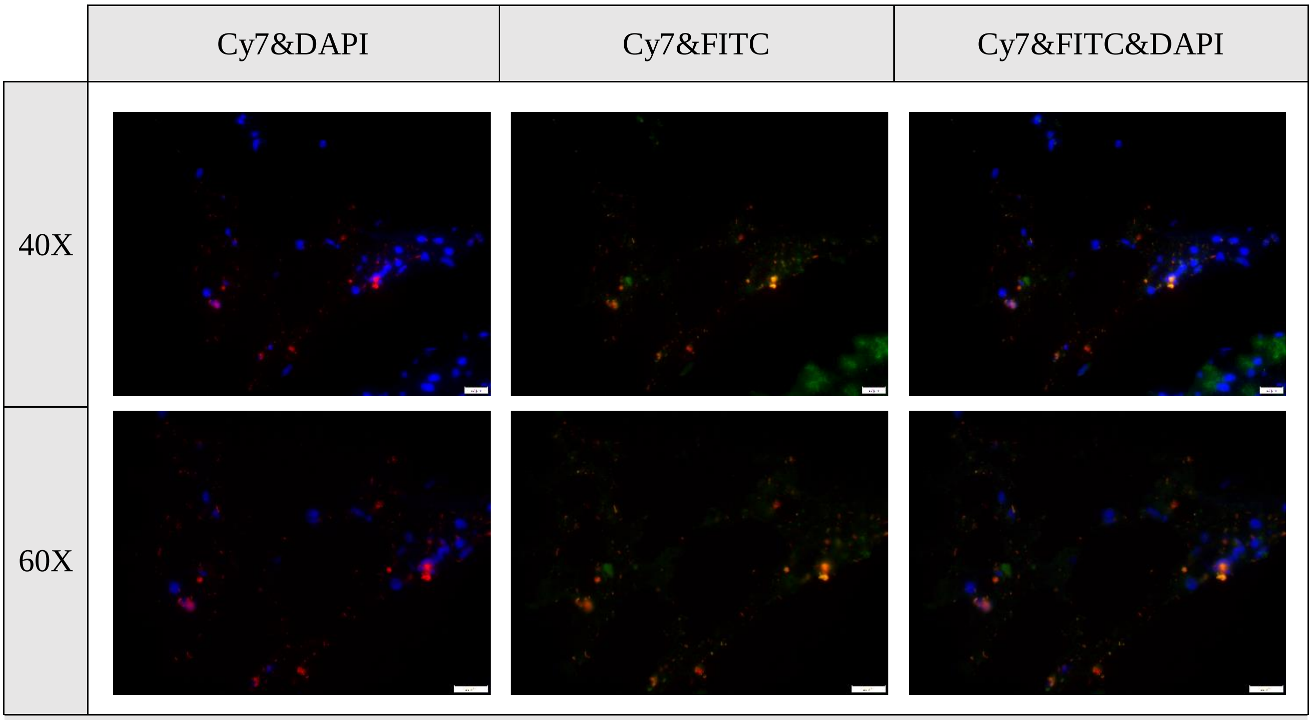

**Figure 7.** Fluorescence microscopy images of the DAPI stained pancreatic cryosection from CT26-Luc tumor bearing mice, which was taken out from mouse L699 IIL after two hours from intraperitoneally administrating AF750-labeled BGs on day 6 from tumor growth. The tissue cryosection, which represents a junction site, was imaged at 40X and 60X magnifications (scale bar 20µm). Cy7 and DAPI merge channels (left column) illustrate the alignment of AF750 labeled BGs on the surface of pancreatic tissue. Cy7 and FITC merge channels (middle column) illustrate the overlay between AF750 emission and immunofluorescence staining of ice nucleation protein. Cy7, FITC and DAPI merge channels (right column) represent the final results.

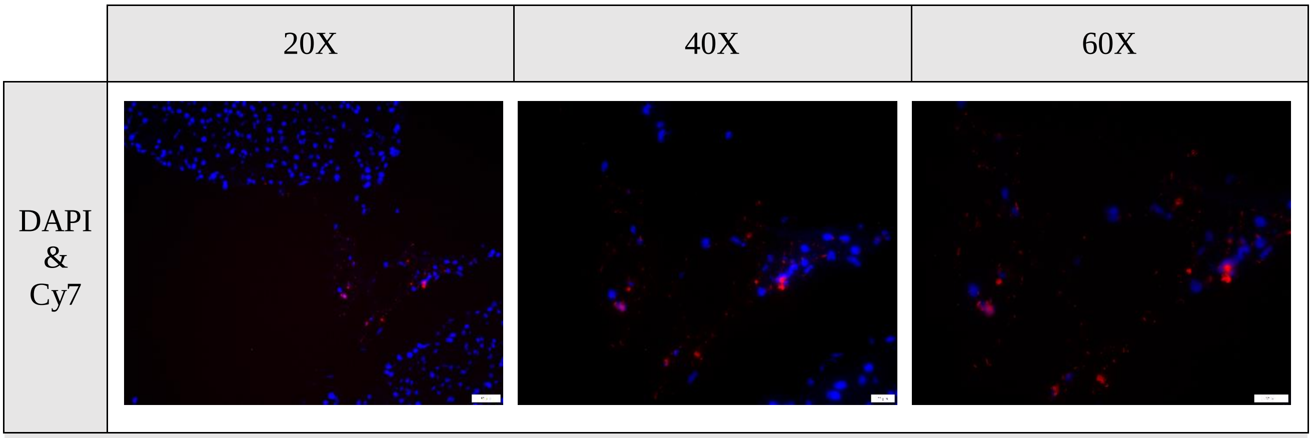

**Figure 8.** Fluorescence microscopy images of the same location in figure 7, presents clearly the localization of AF750 labeled BGs on the junction site, imaged using Cy7 filter and merged with DAPI stained tissue at 20X (scale bar 50μm), 40X and 60X magnifications (scale bar 20μm).

In figure 9 is another example on the positive presence of AF750-labeled BGs, also in a junction part of a DAPI stained pancreatic cryosections, taken from mouse L699 IIL, fluorescently imaged using DAPI and Cy7 filter at 10X magnification.

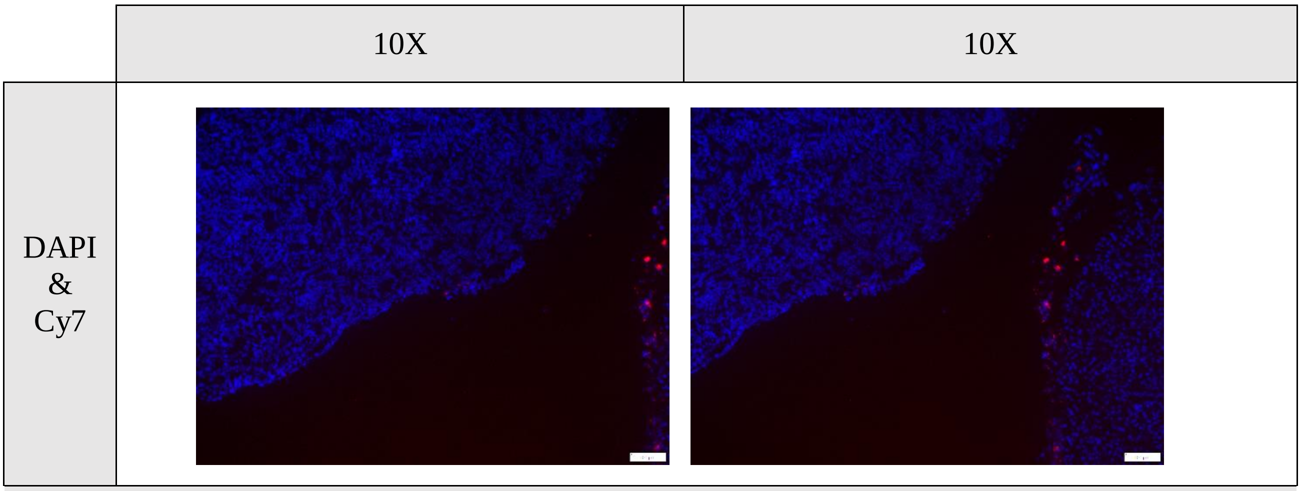

**Figure 9.** Fluorescence microscopy images of the DAPI stained pancreatic cryosection from CT26-Luc tumor bearing mice, which was taken out from mouse L699 IIL after two hours from intraperitoneally administrating AF750-labeled BGs on day 6 from tumor growth. The tissue cryosection, which represents a junction site was imaged using Cy7 filter and merged with DAPI channel at 10X magnification (scale bar 100μm).

The presence of AF750-labeled BGs was visibly more in the pancreas taken from mouse L699 IIL+R (CT26-Luc tumor bearing mouse, treated with AF750-labeled BGs on day 6 from tumor growth, and this pancreas was taken out of the mouse two hours after intraperitoneally injecting BGs). Through fluorescence imaging, BGs were detected on the begin and middle parts of this pancreas (we use the terms of begin, middle and end to describe the direction by which these organs were sectioned, so it was linked to the way of embedding the organ and not their real localization in the mouse). Figures 10 and 11 are examples on the middle parts and figure 12 is an example on detecting AF750-labeled BGs on the beginning of the same pancreas.

| | Cy7&DAPI | Cy7&FITC | Cy7&FITC&DAPI |
|---|---|---|---|
| 10X | 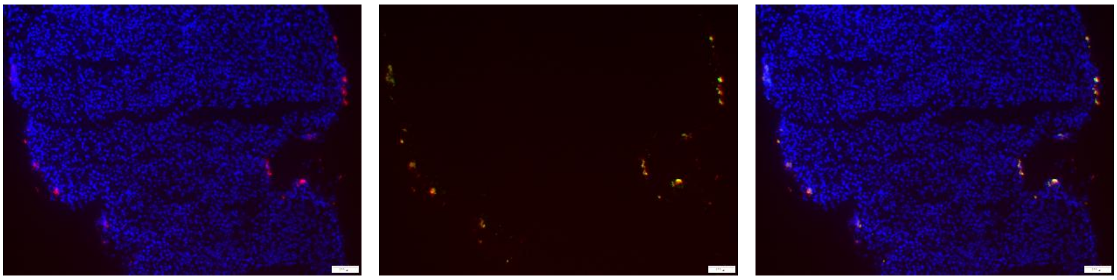 | | |

**Figure 10.** Fluorescence microscopy images of the DAPI stained pancreatic cryosection from CT26-Luc tumor bearing mice, which was taken out from mouse L699 IIL+R after two hours from intraperitoneally administrating AF750-labeled BGs on day 6 from tumor growth. The tissue cryosection, which represents a middle part from the pancreas, was imaged at 10X magnification (scale bar 100µm). Cy7 and DAPI merge channels (left column) illustrate the alignment of AF750 labeled BGs on the surface of pancreatic tissue (on the border of the taken image). Cy7 and FITC merge channels (middle column) illustrate the overlay between AF750 emission and immunofluorescence staining of ice nucleation protein. Cy7, FITC and DAPI merge channels (right column) represent the final results.

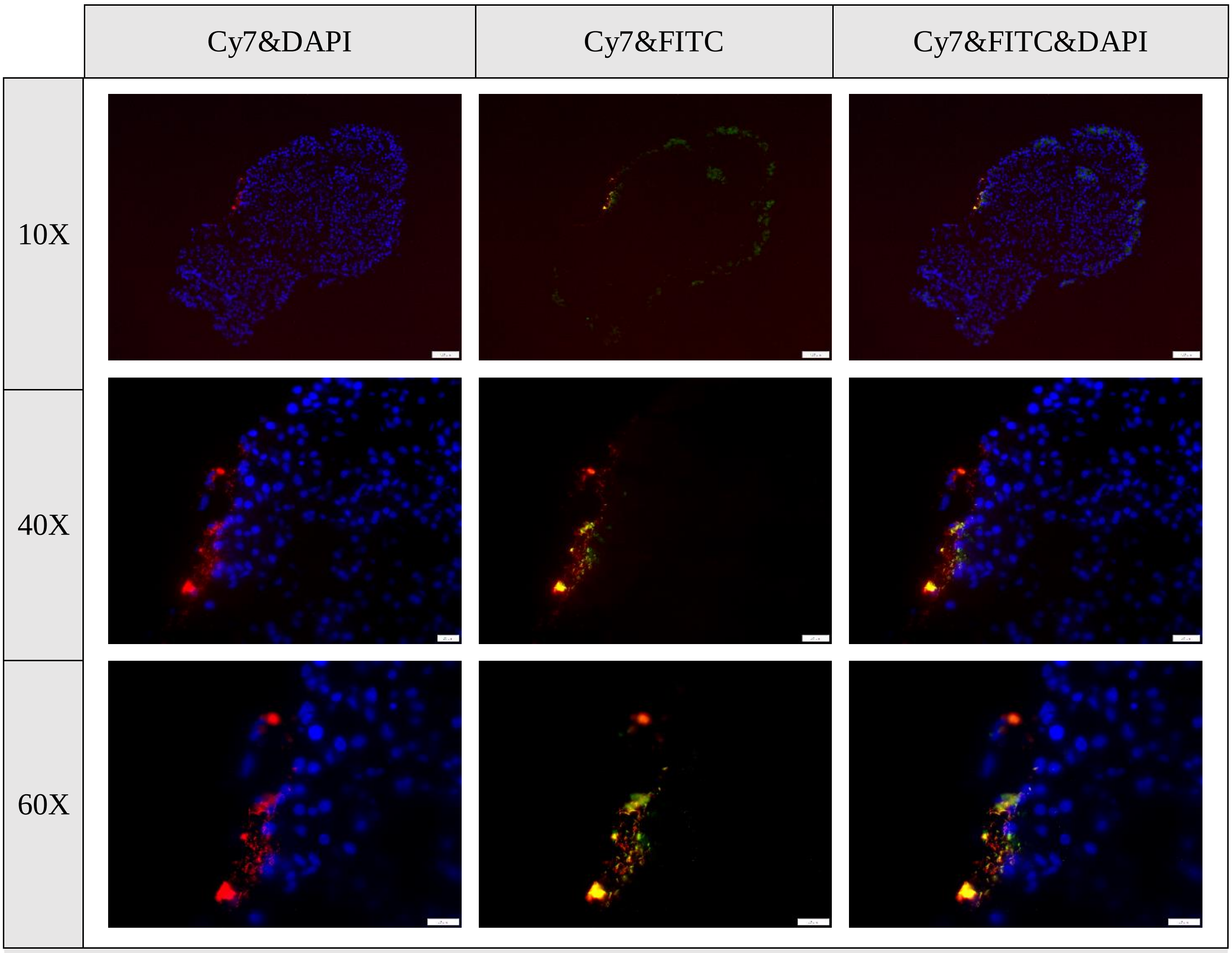

**Figure 11.** Fluorescence microscopy images of the DAPI stained pancreatic cryosection from CT26-Luc tumor bearing mice, which was taken out from mouse L699 IIL+R after two hours from intraperitoneally administrating AF750-labeled BGs on day 6 from tumor growth. The tissue cryosection, which represents another middle part from the pancreas, was imaged at 10X (scale bar 100µm), 40X and 60X magnifications (scale bar 20µm). Cy7 and DAPI merge channels (left column) illustrate the alignment of AF750 labeled BGs on the surface of pancreatic tissue (on the border of the taken image). Cy7 and FITC merge channels (middle column) illustrate the overlay between AF750 emission and immunofluorescence staining of ice nucleation protein. Cy7, FITC and DAPI merge channels (right column) represent the final results.

|  | Cy7&DAPI | Cy7&FITC | Cy7&FITC&DAPI |
|---|---|---|---|
| 10X | 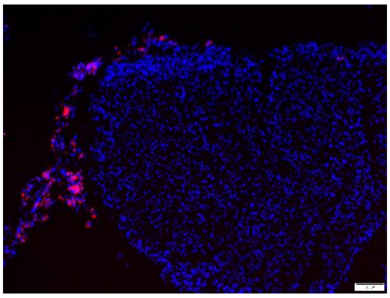 | 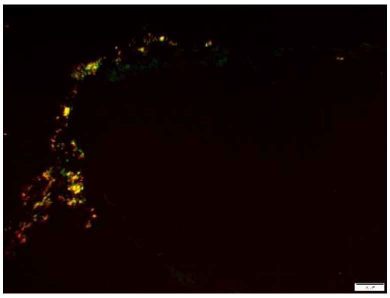 | 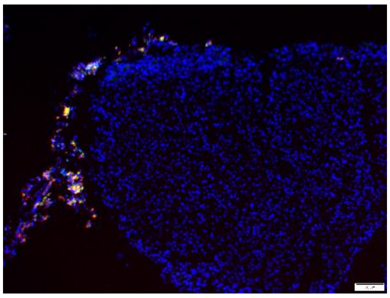 |

**Figure 12.** Fluorescence microscopy images of the DAPI stained pancreatic cryosection from CT26-Luc tumor bearing mice, which was taken out from mouse L699 IIL+R after two hours from intraperitoneally administrating AF750-labeled BGs on day 6 from tumor growth. The tissue cryosection, which represents a beginning part from the pancreas, was imaged at 10X magnification (scale bar 100µm). Cy7 and DAPI merge channels (left column) illustrate the alignment of AF750 labeled BGs on the surface of pancreatic tissue. Cy7 and FITC merge channels (middle column) illustrate the overlay between AF750 emission and immunofluorescence staining of ice nucleation protein. Cy7, FITC and DAPI merge channels (right column) represent the final results.

AF750 labeled BGs were also positively detected in INP immunofluorescence stained pancreatic cryosections from mouse L699 IIU (CT26-Luc tumor bearing mouse, treated with AF750-labeled BGs on day 6 from tumor growth, and this pancreas was taken out of the mouse two hours after intraperitoneally injecting BGs), on the beginning parts (figure 13), junction locations (figure 14) and middle parts (figure 15).

|  | Cy7&DAPI | Cy7&FITC | Cy7&FITC&DAPI |
|---|---|---|---|
| 10X | 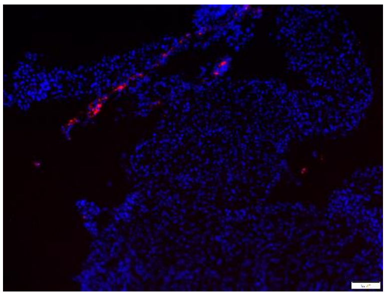 | 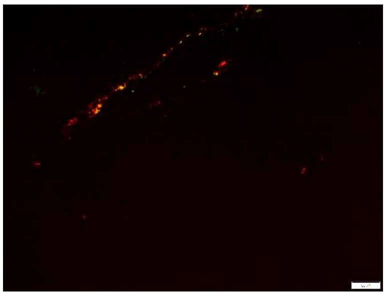 | 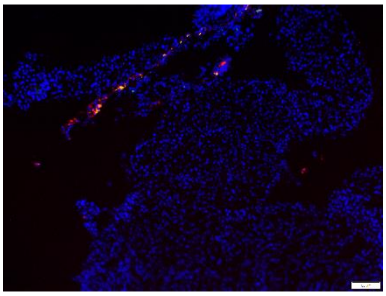 |

**Figure 13.** Fluorescence microscopy images of the DAPI stained pancreatic cryosection from CT26-Luc tumor bearing mice, which was taken out from mouse L699 IIU after two hours from intraperitoneally administrating AF750-labeled BGs on day 6 from tumor growth. The tissue cryosection, which represents a beginning part from the pancreas, was imaged at 10X magnification (scale bar 100µm). Cy7 and DAPI merge channels (left column) illustrate the alignment of AF750 labeled BGs on the surface of pancreatic tissue. Cy7 and FITC merge channels (middle column) illustrate the overlay between AF750 emission and immunofluorescence staining of ice nucleation protein. Cy7, FITC and DAPI merge channels (right column) represent the final results.

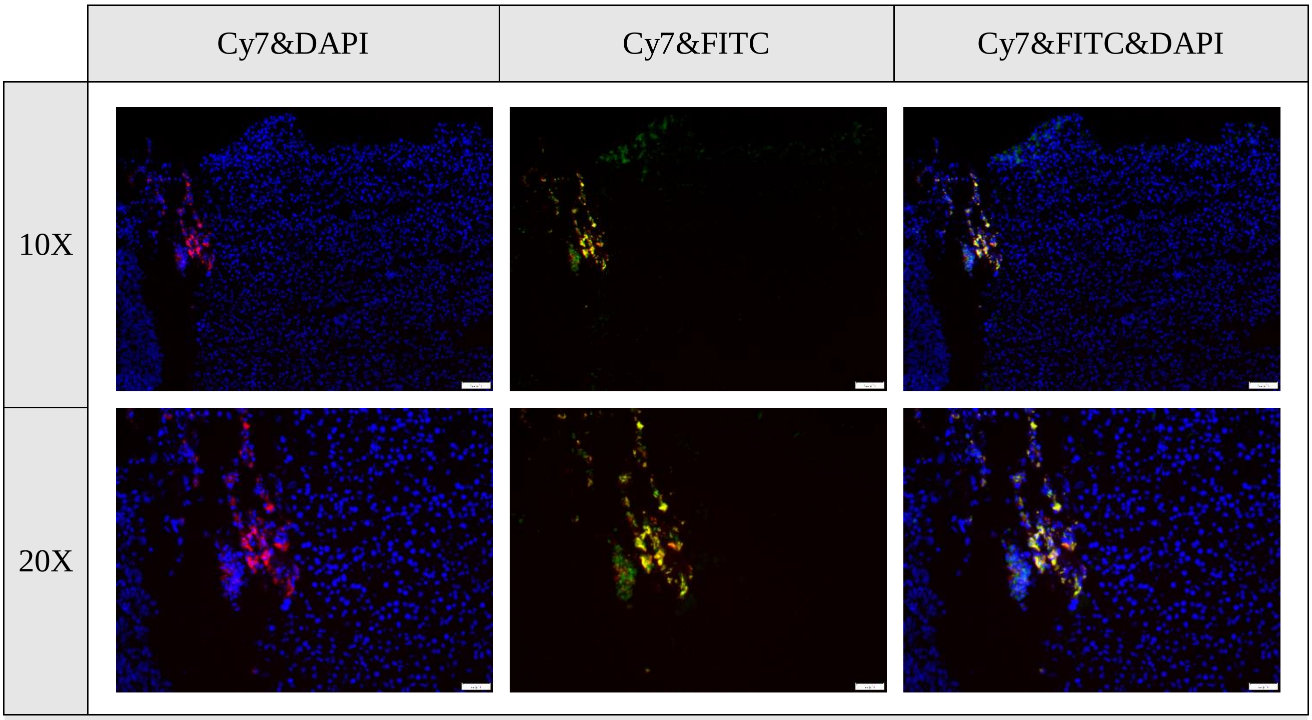

**Figure 14.** Fluorescence microscopy images of the DAPI stained pancreatic cryosection from CT26-Luc tumor bearing mice, which was taken out from mouse L699 IIU after two hours from intraperitoneally administrating AF750-labeled BGs on day 6 from tumor growth. The tissue cryosection, which represents a junction site from the pancreas, was imaged at 10X (scale bar 100µm) and 20X magnifications (scale bar 50µm). Cy7 and DAPI merge channels (left column) illustrate the alignment of AF750 labeled BGs on the surface of pancreatic tissue. Cy7 and FITC merge channels (middle column) illustrate the overlay between AF750 emission and immunofluorescence staining of ice nucleation protein. Cy7, FITC and DAPI merge channels (right column) represent the final results.

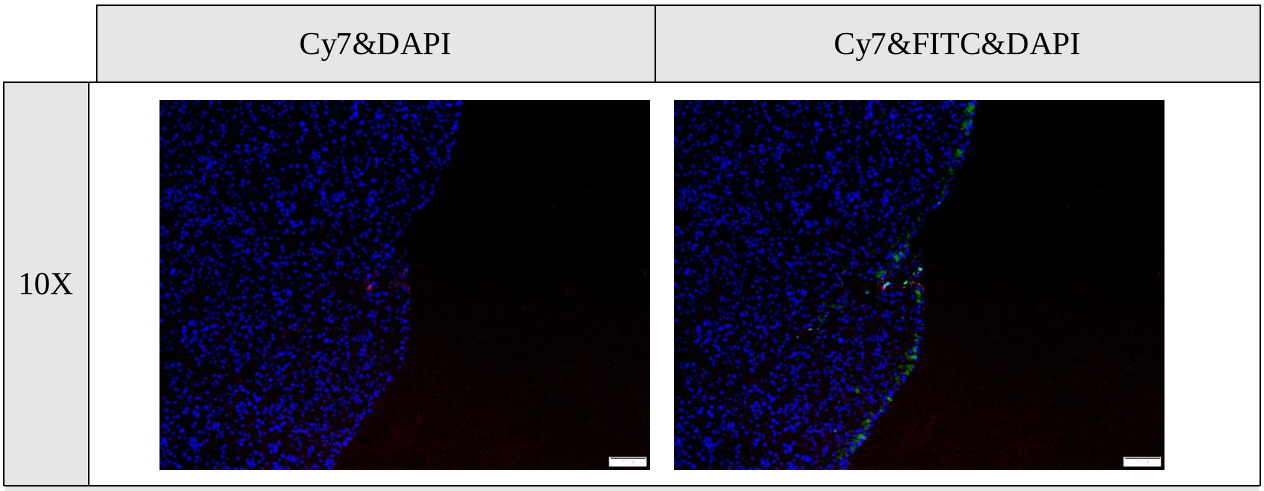

**Figure 15.** Fluorescence microscopy images of the DAPI stained pancreatic cryosection from CT26-Luc tumor bearing mice, which was taken out from mouse L699 IIU after two hours from intraperitoneally administrating AF750-labeled BGs on day 6 from tumor growth. The tissue cryosection, which represents a middle part from the pancreas, was imaged at 10X magnification (scale bar 100µm). Cy7 and DAPI merge channels (left column) illustrate the alignment of AF750 labeled BGs on the surface of pancreatic tissue (on the border of the taken image). Cy7, FITC and DAPI merge channels (right column) confirm the positive signals and represent the final results.

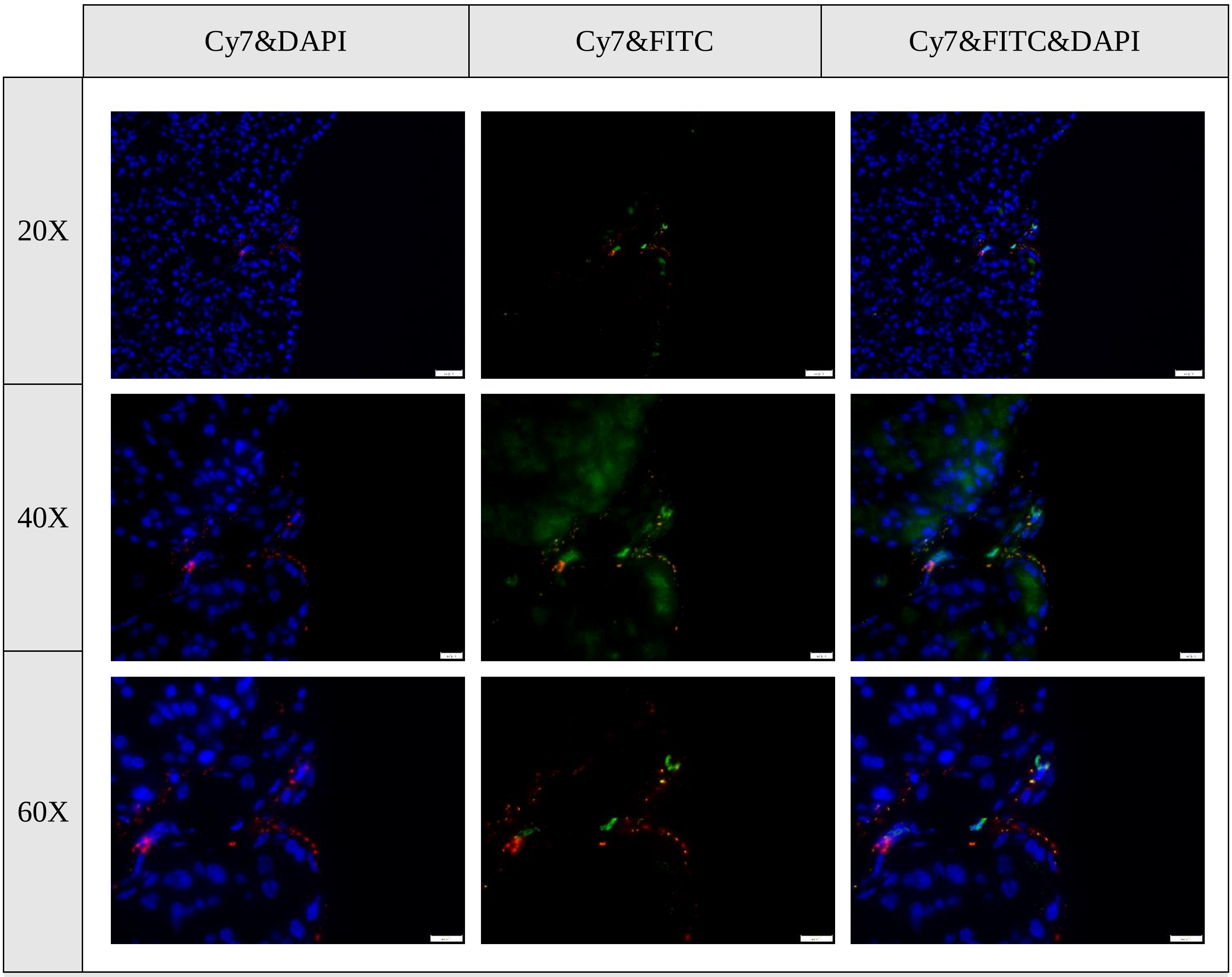

**Figure 16.** Fluorescence microscopy images of the same DAPI stained location in figure 15 at 20X (scale bar 50µm), 40X and 60X magnifications (scale bar 20µm). Cy7 and DAPI merge channels (left column) illustrate the alignment of AF750 labeled BGs on the surface of pancreatic tissue. Cy7 and FITC merge channels (middle column) illustrate the overlay between AF750 emission and immunofluorescence staining of ice nucleation protein. Cy7, FITC and DAPI merge channels (right column) represent the final results.

### 1.4. Imaging pancreatic tumor cryosections

The detection of AF750-labeled BGs was obviously more in pancreatic tumor cryosections than in their corresponding pancreatic cryosections, as these tumors represent the superficial parts of the tissues exposed to the IP injected AF750 labeled BGs. However, BGs were detected in the three pancreatic tumors, which were taken from the three tumor bearing mice L699 IIL, IIL+R and IIU.

Fluorescent microscopy imaging of INP immunofluorescence stained pancreatic tumor cryosections from mouse L699 IIL (CT26-Luc tumor bearing mouse, treated with AF750-

labeled BGs on day 6 from tumor growth, and this pancreatic tumor was taken out of the mouse two hours after intraperitoneally injecting BGs) illustrated the localization of AF750 labeled BGs in the beginning (figures 17 and 18) and middle parts of this tissue (figure 17).

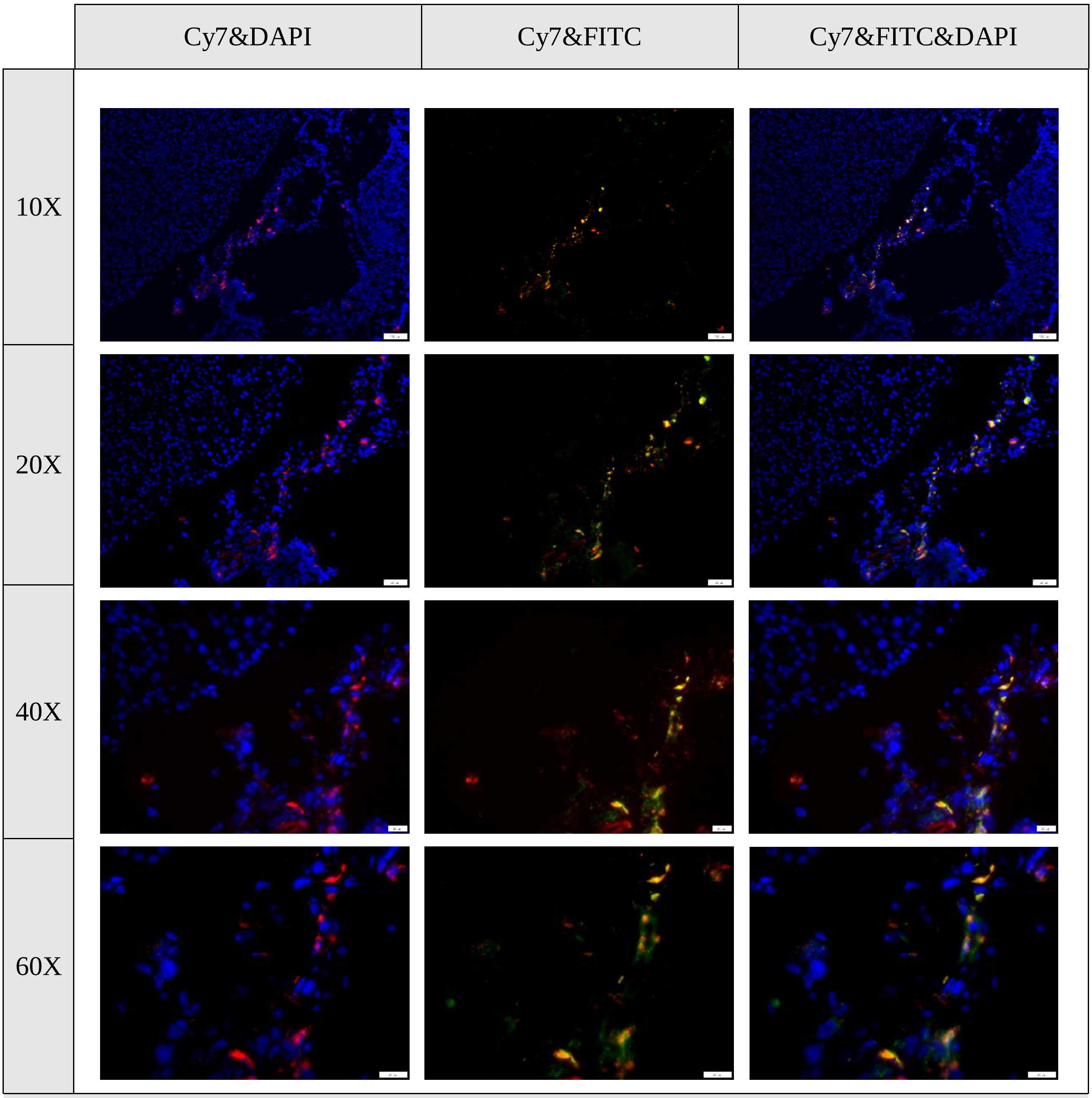

**Figure 17.** Fluorescence microscopy images of the DAPI stained pancreatic tumor cryosection from CT26-Luc tumor bearing mice, which was taken out from mouse L699 IIL after two hours from intraperitoneally administrating AF750-labeled BGs on day 6 from tumor growth. The tissue cryosection, which represents a beginning part from the pancreatic tumor, was imaged at 10X (scale bar 100µm), 20X (scale bar 50µm), 40X and 60X magnifications (scale bar 20µm). Cy7 and DAPI merge channels (left column) illustrate the alignment of AF750 labeled BGs on the surface of pancreatic tissue. Cy7 and FITC merge channels (middle column) illustrate the overlay between AF750 emission and immunofluorescence staining of ice nucleation protein. Cy7, FITC and DAPI merge channels (right column) represent the final results.

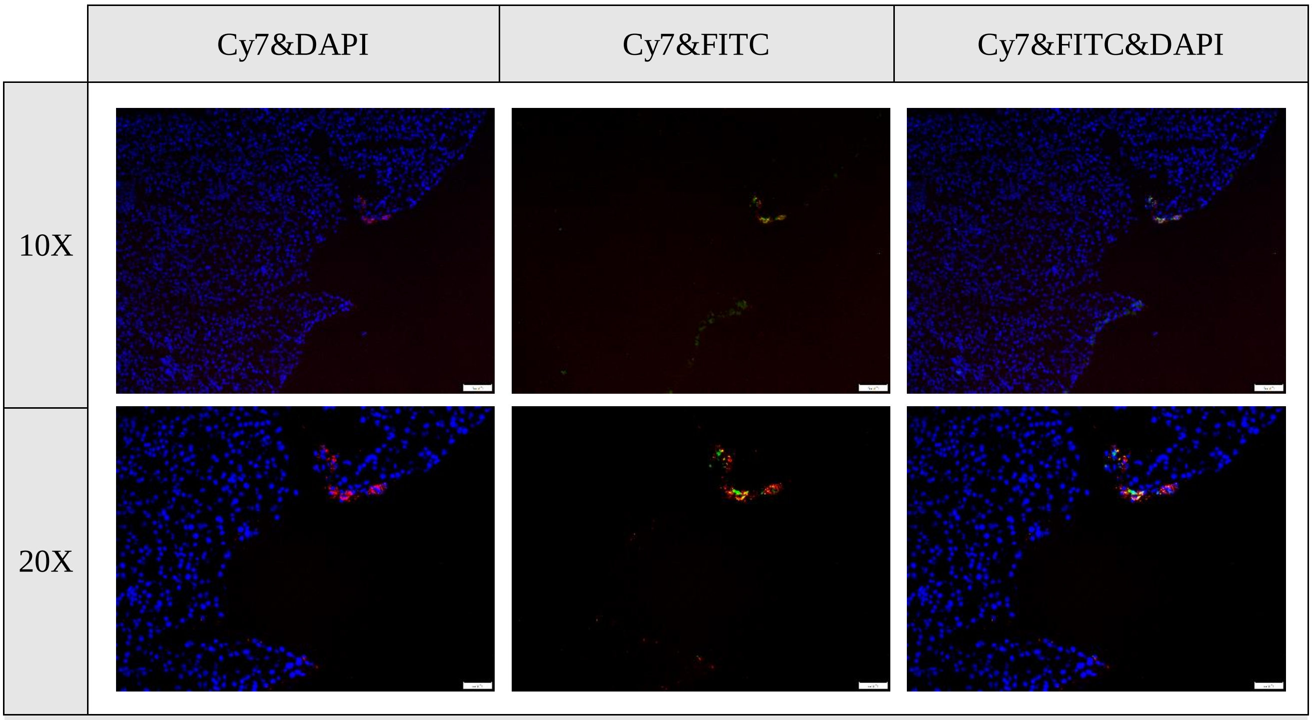

**Figure 18.** Fluorescence microscopy images of the DAPI stained pancreatic tumor cryosection from CT26-Luc tumor bearing mice, which was taken out from mouse L699 IIL after two hours from intraperitoneally administrating AF750-labeled BGs on day 6 from tumor growth. The tissue cryosection, which represents another beginning part from the pancreatic tumor, was imaged at 10X (scale bar 100µm) and 20X magnifications (scale bar 50µm). Cy7 and DAPI merge channels (left column) illustrate the alignment of AF750 labeled BGs on the surface of pancreatic tissue. Cy7 and FITC merge channels (middle column) illustrate the overlay between AF750 emission and immunofluorescence staining of ice nucleation protein. Cy7, FITC and DAPI merge channels (right column) represent the final results.

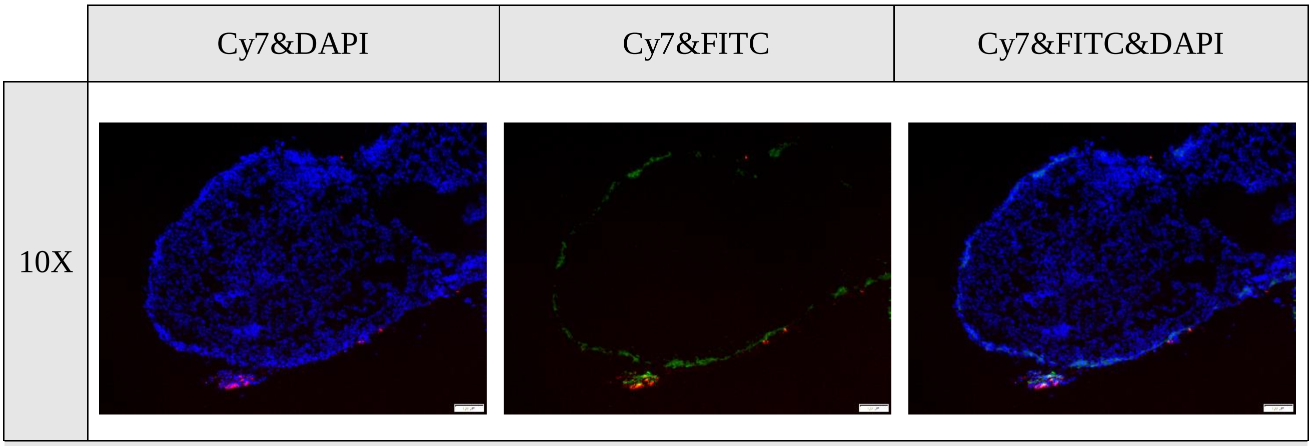

**Figure 19.** Fluorescence microscopy images of the DAPI stained pancreatic tumor cryosection from CT26-Luc tumor bearing mice, which was taken out from mouse L699 IIL after two hours from intraperitoneally administrating AF750-labeled BGs on day 6 from tumor growth. The tissue cryosection, which represents a middle part from the pancreatic tumor, was imaged at 10X magnification (scale bar 100μm). Cy7 and DAPI merge channels (left column) illustrate the alignment of AF750 labeled BGs on the border of pancreatic tissue. Cy7 and FITC merge channels (middle column) illustrate the overlay between AF750 emission and immunofluorescence staining of ice nucleation protein. Cy7, FITC and DAPI merge channels (right column) represent the final results.

Fluorescent microscopy imaging of INP immunofluorescence stained pancreatic tumor cryosections from mouse L699 IIL+R (CT26-Luc tumor bearing mouse, treated with AF750-labeled BGs on day 6 from tumor growth, and this pancreatic tumor was taken out of the mouse two hours after intraperitoneally injecting BGs) illustrated the localization of AF750 labeled BGs in the beginning parts of the sectioned tissue (figures 20, 21 and 22), as well as, the middle parts of the same tissue (figures 23, 24 and 25).

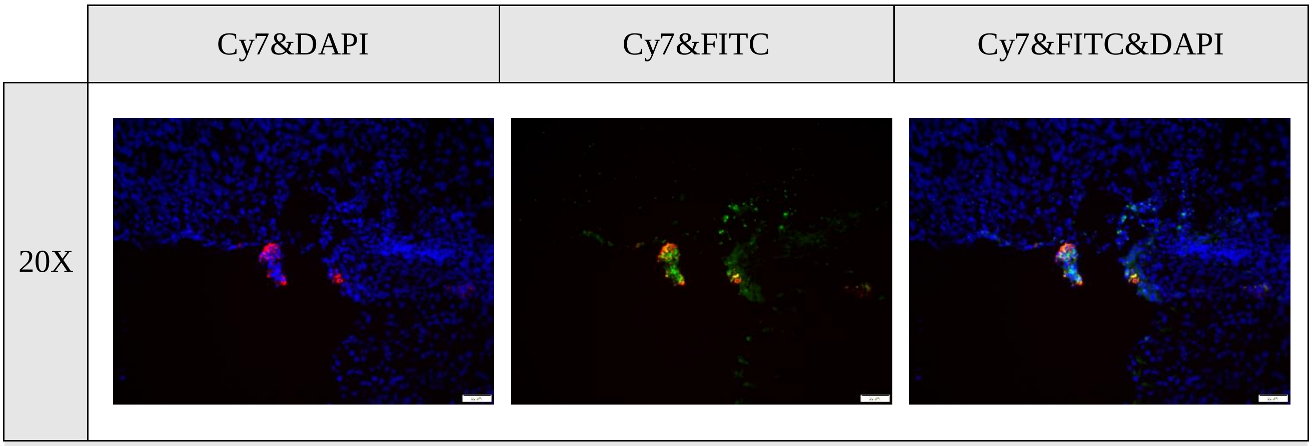

**Figure 20.** Fluorescence microscopy images of the DAPI stained pancreatic tumor cryosection from CT26-Luc tumor bearing mice, which was taken out from mouse L699 IIL+R after two hours from intraperitoneally administrating AF750-labeled BGs on day 6 from tumor growth. The tissue cryosection, which represents a beginning part from the pancreatic tumor, was imaged at 20X and magnification (scale bar 50μm). Cy7 and DAPI merge channels (left column) illustrate the alignment of AF750 labeled BGs on the surface of pancreatic tissue. Cy7 and FITC merge channels (middle column) illustrate the overlay between AF750 emission and immunofluorescence staining of ice nucleation protein. Cy7, FITC and DAPI merge channels (right column) represent the final results.

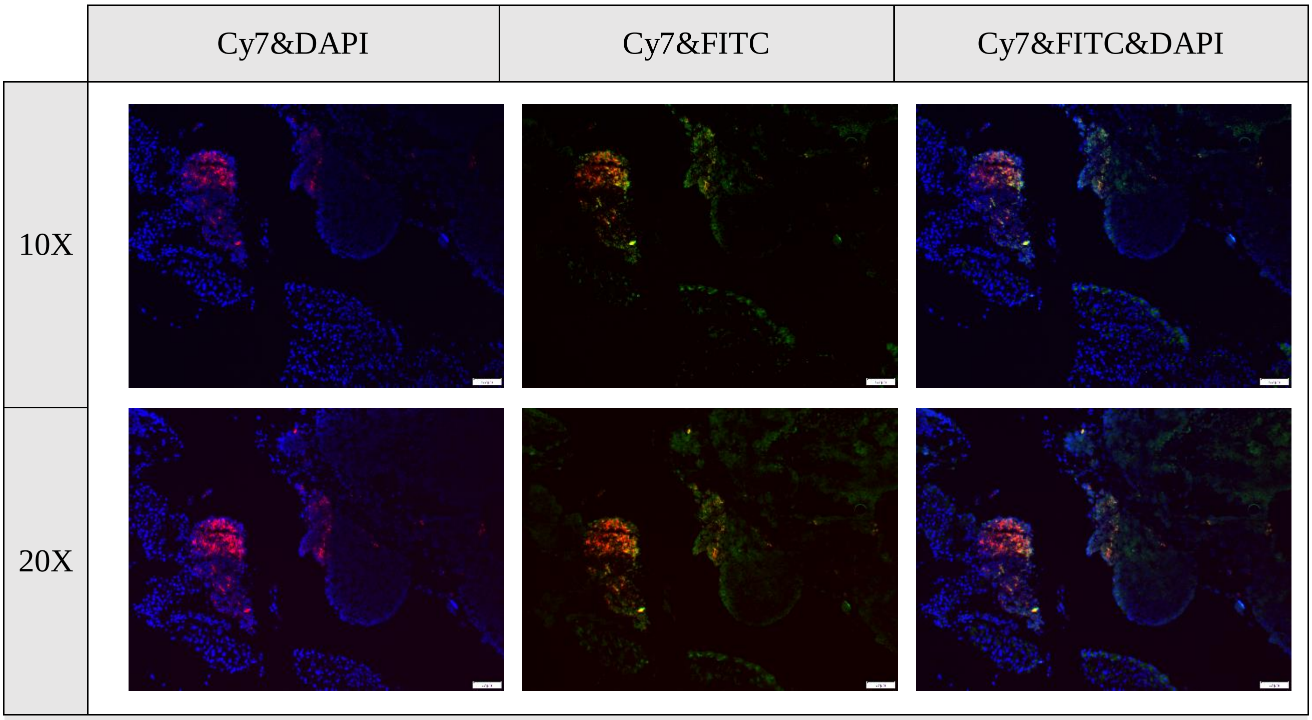

**Figure 21.** Fluorescence microscopy images of the DAPI stained pancreatic tumor cryosection from CT26-Luc tumor bearing mice, which was taken out from mouse L699 IIL+R after two hours from intraperitoneally administrating AF750-labeled BGs on day 6 from tumor growth. The tissue cryosection, which represents another beginning part from the pancreatic tumor, was imaged at 10X (scale bar 100µm) and 20X magnifications (scale bar 50µm). Cy7 and DAPI merge channels (left column) illustrate the alignment of AF750 labeled BGs on the surface of pancreatic tissue. Cy7 and FITC merge channels (middle column) illustrate the overlay between AF750 emission and immunofluorescence staining of ice nucleation protein. Cy7, FITC and DAPI merge channels (right column) represent the final results.

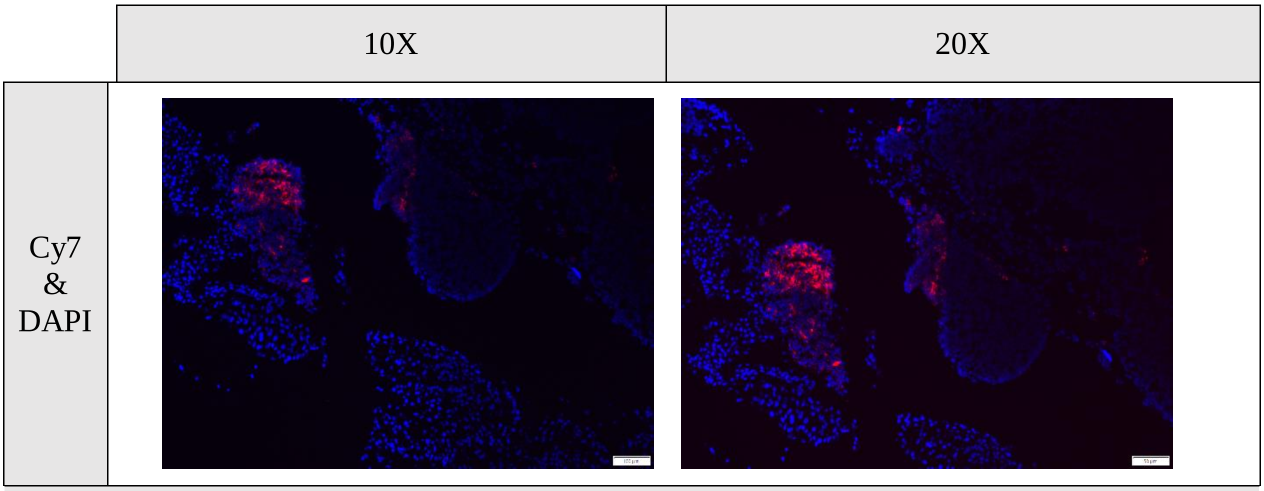

**Figure 22.** Fluorescence microscopy images of the same DAPI stained pancreatic tumor cryosection from mouse L699 IIL+R, in figure 21, at 10X (scale bar 100µm) and 20X magnifications (scale bar 50µm). Cy7 and DAPI merge channels (left column) illustrate the alignment of AF750 labeled BGs on the surface of pancreatic tissue.

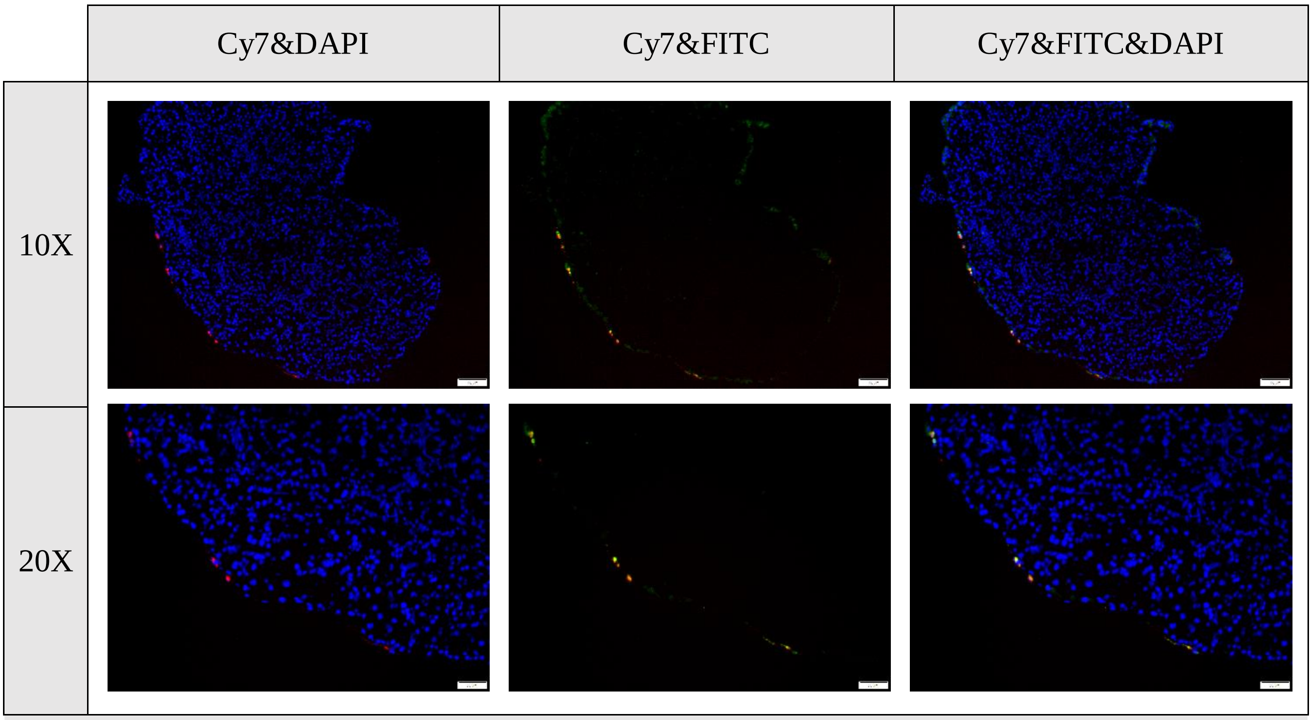

**Figure 23. .** Fluorescence microscopy images of the DAPI stained pancreatic tumor cryosection from CT26-Luc tumor bearing mice, which was taken out from mouse L699 IIL+R after two hours from intraperitoneally administrating AF750-labeled BGs on day 6 from tumor growth. The tissue cryosection, which represents a middle part from the pancreatic tumor, was imaged at 10X (scale bar 100µm) and 20X magnifications (scale bar 50µm). Cy7 and DAPI merge channels (left column) illustrate the alignment of AF750 labeled BGs on the surface of pancreatic tissue. Cy7 and FITC merge channels (middle column) illustrate the overlay between AF750 emission and immunofluorescence staining of ice nucleation protein. Cy7, FITC and DAPI merge channels (right column) represent the final results.

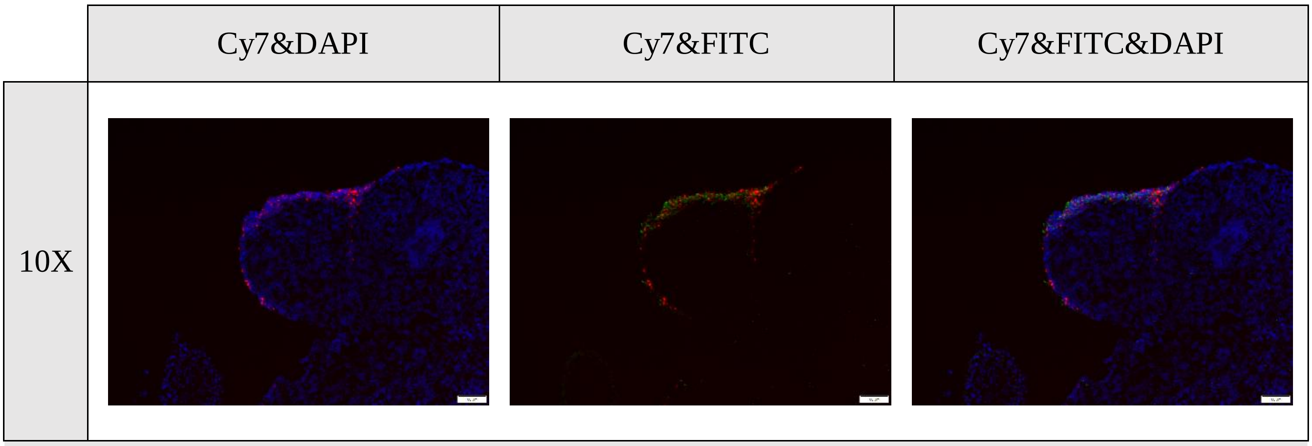

**Figure 24. .** Fluorescence microscopy images of the DAPI stained pancreatic tumor cryosection from CT26-Luc tumor bearing mice, which was taken out from mouse L699 IIL+R after two hours from intraperitoneally administrating AF750-labeled BGs on day 6 from tumor growth. The tissue cryosection, which represents another middle part from the pancreatic tumor, was imaged at 10X magnification (scale bar 100µm). Cy7 and DAPI merge channels (left column) illustrate the alignment of AF750 labeled BGs on the surface of pancreatic tissue. Cy7 and FITC merge channels (middle column) illustrate the overlay between AF750 emission and immunofluorescence staining of ice nucleation protein. Cy7, FITC and DAPI merge channels (right column) represent the final results.

|  | 10X | 20X |
|---|---|---|
| Cy7<br>&<br>DAPI | 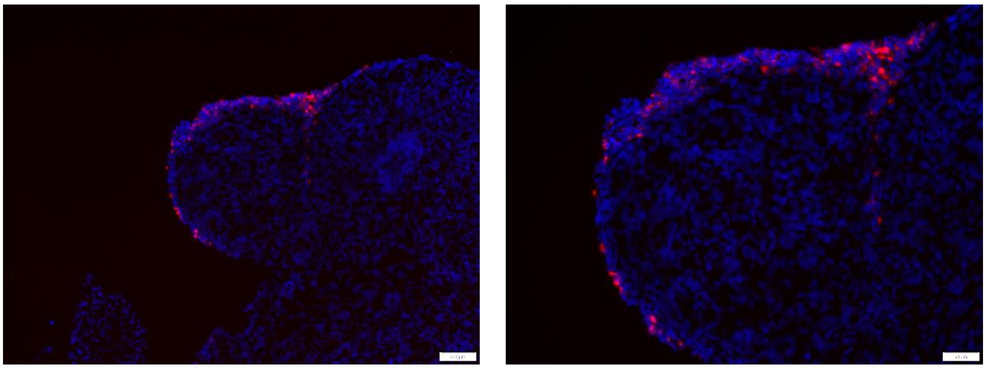 |  |

**Figure 25.** Fluorescence microscopy images of the same DAPI stained pancreatic tumor cryosection from mouse L699 IIL+R, in figure 24, at 10X (scale bar 100µm) and 20X magnifications (scale bar 50µm). Cy7 and DAPI merge channels illustrates the alignment of AF750 labeled BGs on the surface of pancreatic tissue.

Fluorescent microscopy imaging of INP immunofluorescence stained pancreatic tumor cryosections from mouse L699 IIU (CT26-Luc tumor bearing mouse, treated with AF750-labeled BGs on day 6 from tumor growth, and this pancreatic tumor was taken out of the mouse two hours after intraperitoneally injecting BGs) illustrated the localization of AF750 labeled BGs in the beginning parts of the sectioned tissue (figures 26 and 27), as well as, the middle parts of the same tissue (figures 28, 29 and 30).

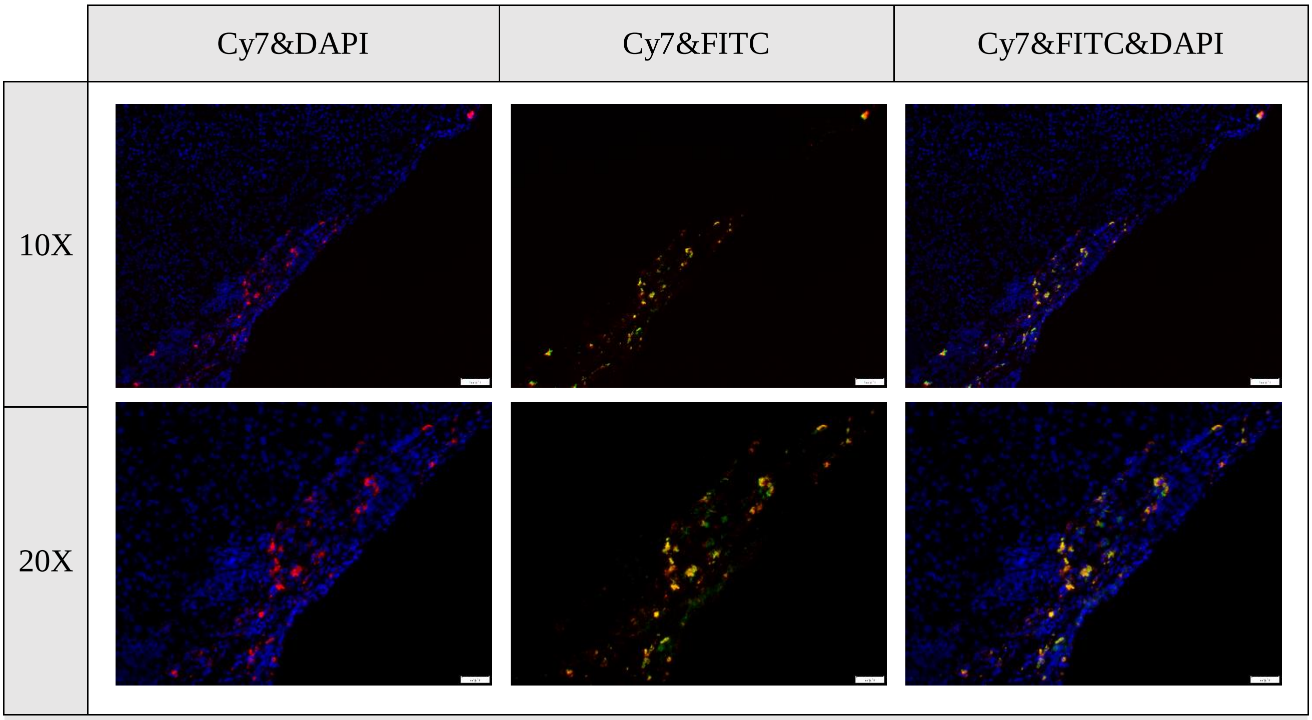

**Figure 26.** Fluorescence microscopy images of the DAPI stained pancreatic tumor cryosection from CT26-Luc tumor bearing mice, which was taken out from mouse L699 IIU after two hours from intraperitoneally administrating AF750-labeled BGs on day 6 from tumor growth. The tissue cryosection, which represents a beginning part from the pancreatic tumor, was imaged at 10X (scale bar 100µm) and 20X magnifications (scale bar 50µm). Cy7 and DAPI merge channels (left column) illustrate the alignment of AF750 labeled BGs on the surface of pancreatic tissue. Cy7 and FITC merge channels (middle column) illustrate the overlay between AF750 emission and immunofluorescence staining of ice nucleation protein. Cy7, FITC and DAPI merge channels (right column) represent the final results.

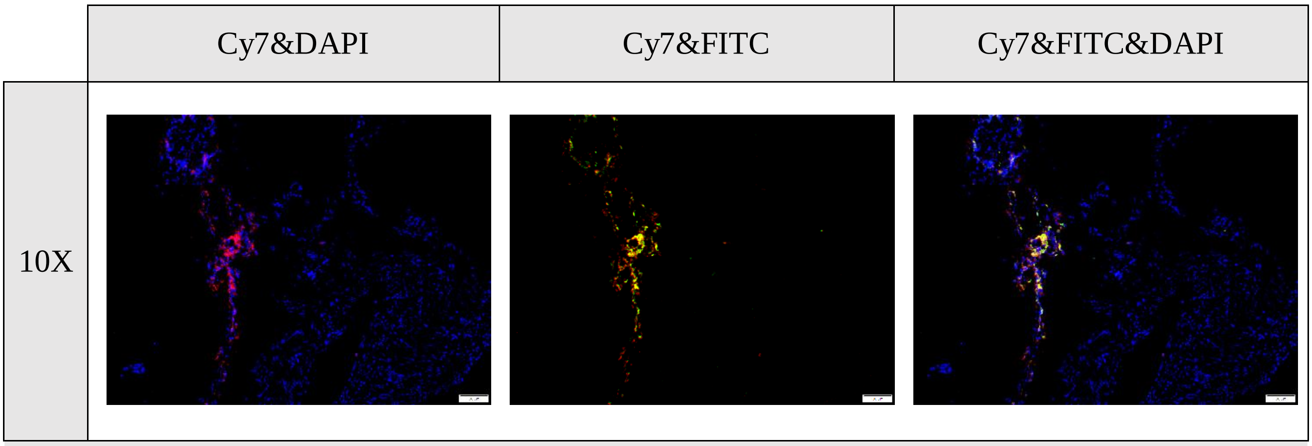

**Figure 27.** Fluorescence microscopy images of the DAPI stained pancreatic tumor cryosection from CT26-Luc tumor bearing mice, which was taken out from mouse L699 IIU after two hours from intraperitoneally administrating AF750-labeled BGs on day 6 from tumor growth. The tissue cryosection, which represents another beginning part from the pancreatic tumor, was imaged at 10X magnification (scale bar 100µm). Cy7 and DAPI merge channels (left column) illustrate the alignment of AF750 labeled BGs on the surface of pancreatic tissue. Cy7 and FITC merge channels (middle column) illustrate the overlay between AF750 emission and immunofluorescence staining of ice nucleation protein. Cy7, FITC and DAPI merge channels (right column) represent the final results.

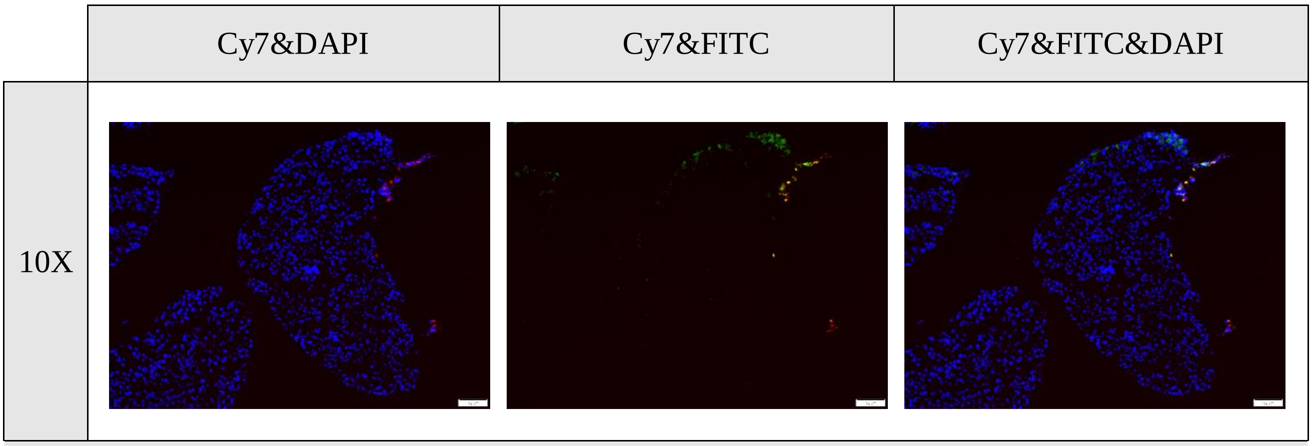

**Figure 28.** Fluorescence microscopy images of the DAPI stained pancreatic tumor cryosection from CT26-Luc tumor bearing mice, which was taken out from mouse L699 IIU after two hours from intraperitoneally administrating AF750-labeled BGs on day 6 from tumor growth. The tissue cryosection, which represents a middle part from the pancreatic tumor, was imaged at 10X magnification (scale bar 100μm). Cy7 and DAPI merge channels (left column) illustrate the alignment of AF750 labeled BGs on the surface of pancreatic tissue. Cy7 and FITC merge channels (middle column) illustrate the overlay between AF750 emission and immunofluorescence staining of ice nucleation protein. Cy7, FITC and DAPI merge channels (right column) represent the final results.

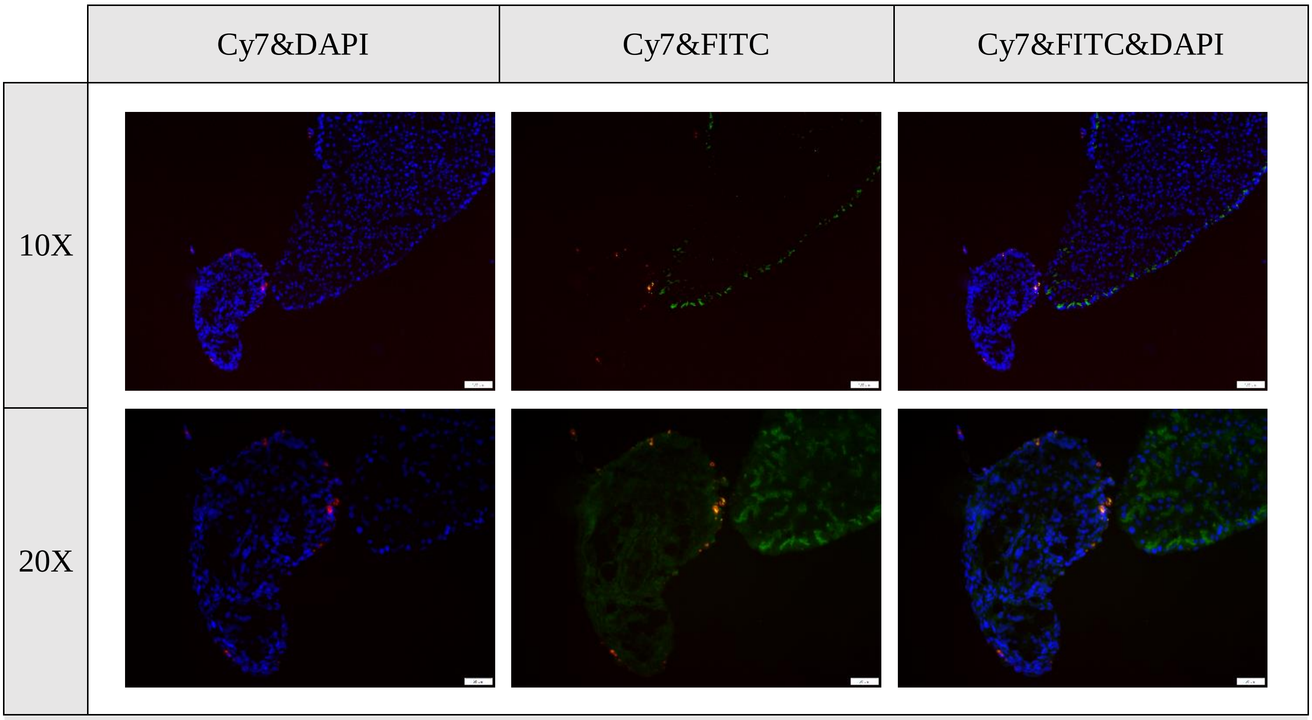

**Figure 29.** Fluorescence microscopy images of the DAPI stained pancreatic tumor cryosection from CT26-Luc tumor bearing mice, which was taken out from mouse L699 IIU after two hours from intraperitoneally administrating AF750-labeled BGs on day 6 from tumor growth. The tissue cryosection, which represents another middle part from the pancreatic tumor, was imaged at 10X (scale bar 100μm) and 20X magnifications (scale bar 50μm). Cy7 and DAPI merge channels (left column) illustrate the alignment of AF750 labeled BGs on the surface of pancreatic tissue. Cy7 and FITC merge channels (middle column) illustrate the overlay between AF750 emission and immunofluorescence staining of ice nucleation protein. Cy7, FITC and DAPI merge channels (right column) represent the final results.

|  | 10X | 20X |
|---|---|---|
| Cy7<br>&<br>DAPI | 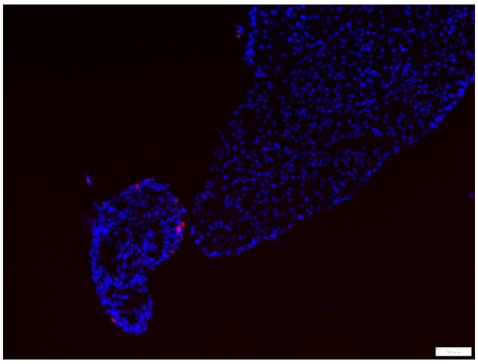 | 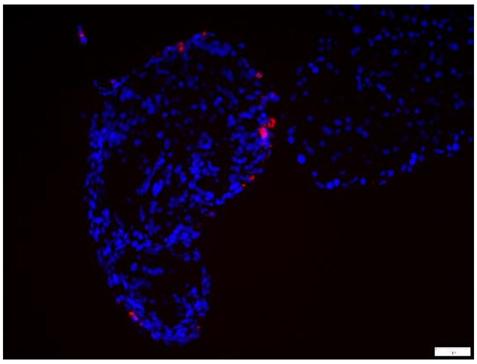 |

**Figure 30.** Fluorescence microscopy images of the same DAPI stained pancreatic tumor cryosection from mouse L699 IIU, in figure 29, at 10X (scale bar 100µm) and 20X magnifications (scale bar 50µm). Cy7 and DAPI merge channels illustrates the alignment of AF750 labeled BGs on the surface of pancreatic tissue.

## 2. Archaea Infiltration Project

In this project, two suspensions of the strictly anaerobic Methanococcus maripaludis S0001 were prepared. One of these suspensions was treated with AF488 in order to label the archaea and the other suspension remained untreated.

After that the samples from these two suspensions were sent to Barbara Reischl, Department of Ecogenomics and Systems Biology, University of Vienna, who confirmed the viability of archaea. Spheroids prepared from CT26-Luc cells were co-cultured with archaea suspensions for 24, 120 and 168 hours. These spheroids were then harvested, prefixed with Paraformaldehyde 4% and embedded in cryomolds, filled up fully with Tissue Tek® O.C.T™ Compound, and placed into a box with lid. The box was stored then in the freezer at **-20 °C.** These spheroids were then cryosectioned, fixed on the slides and DAPI stained, in order to visualize the localization of AF488-labeled archaea.

Using Olympus IX73 inverted microscope, the beginning, middle and end parts of these spheroids' sections were imaged using both DAPI channel (which visualize the prefixed cells) and FITC channel (which visualize the AF488-labeled archaea). Finally, both DAPI and FITC channels were merged and the locations of AF labeled archaea were observed.

After imaging spheroids cryosections, AF labeled archaea were still to be observed on the surface of spheroids' middle parts after 24h from archaea inoculation (figure 31). However, images from the middle parts of spheroids cryosections, inoculated with archaea for 120h, illustrated the tendency of AF labeled archaea to move toward the hypoxic center of these spheroids (figure 32), and furthermore, AF488-labeled archaea were imaged to be almost in the hypoxic center in spheroids inoculated with AF488-labeled archaea for 168h (figure 33).

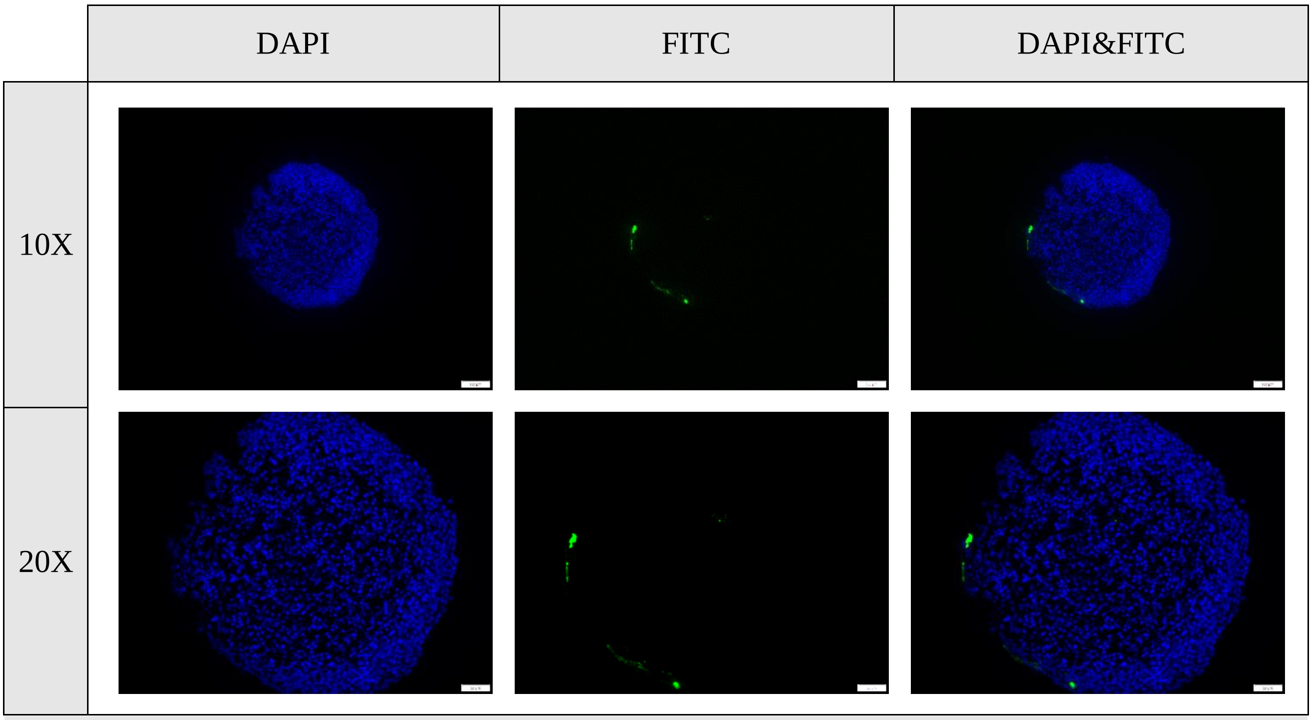

**Figure 31.** Fluorescence microscopy images of archaea's co-culture in CT26-Luc derived spheroid for 24 hours. On day 7 from seeding the spheroid, it was inoculated with AF488-labeled archaea (27µl of AF488 for each ml of archaea suspension). The spheroids were then harvested and prefixed after 24 hours from inoculation (on day 8), and then imbedded after another 24 hours (on day 9). FLM images of the middle part of spheroid's cryosection show the blue emission of DAPI stained cells' nuclei (left column), the emission of AF488 detected through FITC channel (middle column) and the localization of AF488-labeled archaea on the surface of this spheroid (DAPI and FITC merged channels on the right column). DAPI stained spheroid's cryosection was imaged at 10X and 20X magnifications (scale bars 100µm and 50µm respectively).

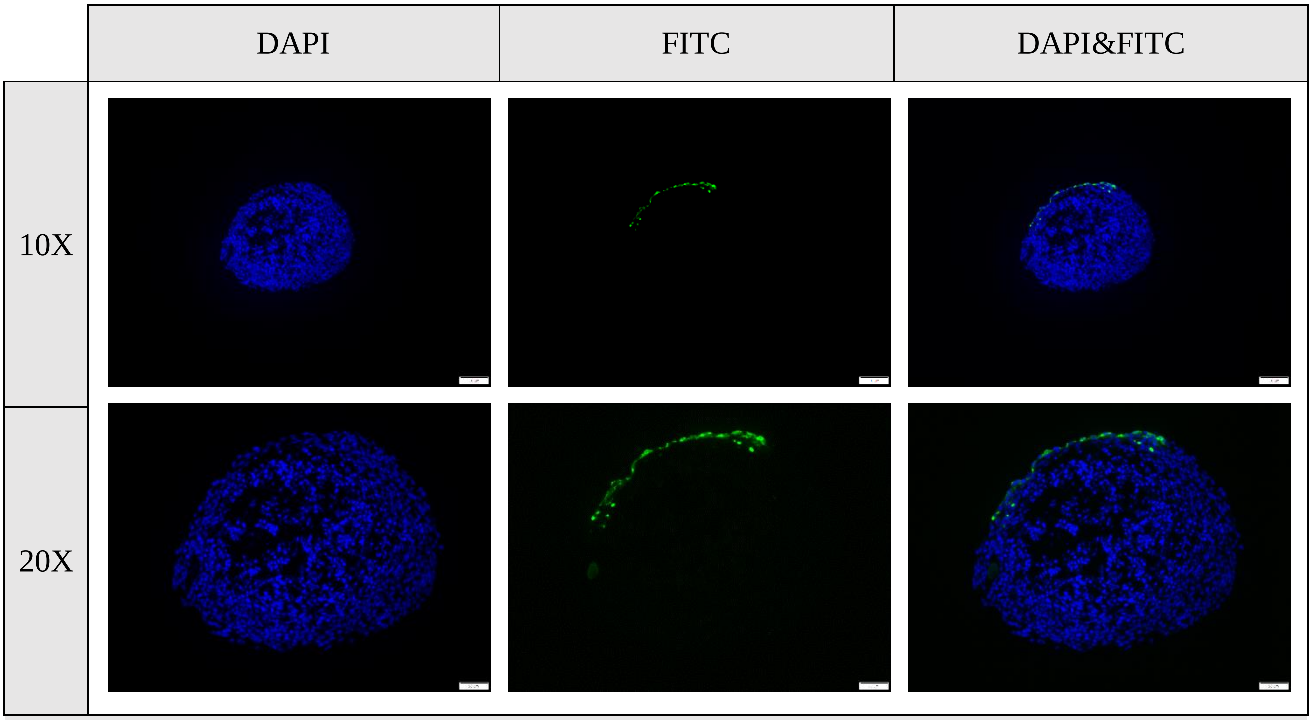

**Figure 32.** Fluorescence microscopy images of archaea’s co-culture in CT26-Luc derived spheroid for 120 hours. On day 7 from seeding the spheroid, it was inoculated with AF488-labeled archaea (27µl of AF488 for each ml of archaea suspension). The spheroids were then harvested and prefixed after 120 hours from inoculation (on day 12), and then imbedded after another 24 hours (on day 13). FLM images of the middle part of spheroid’s cryosection show the blue emission of DAPI stained cells’ nuclei (left column), the emission of AF488 detected through FITC channel (middle column) and the tendency of archaea to move toward the hypoxic center of this spheroid (DAPI and FITC merged channels on the right column). DAPI stained spheroid’s cryosection was imaged at 10X and 20X magnifications (scale bars 100µm and 50µm respectively).

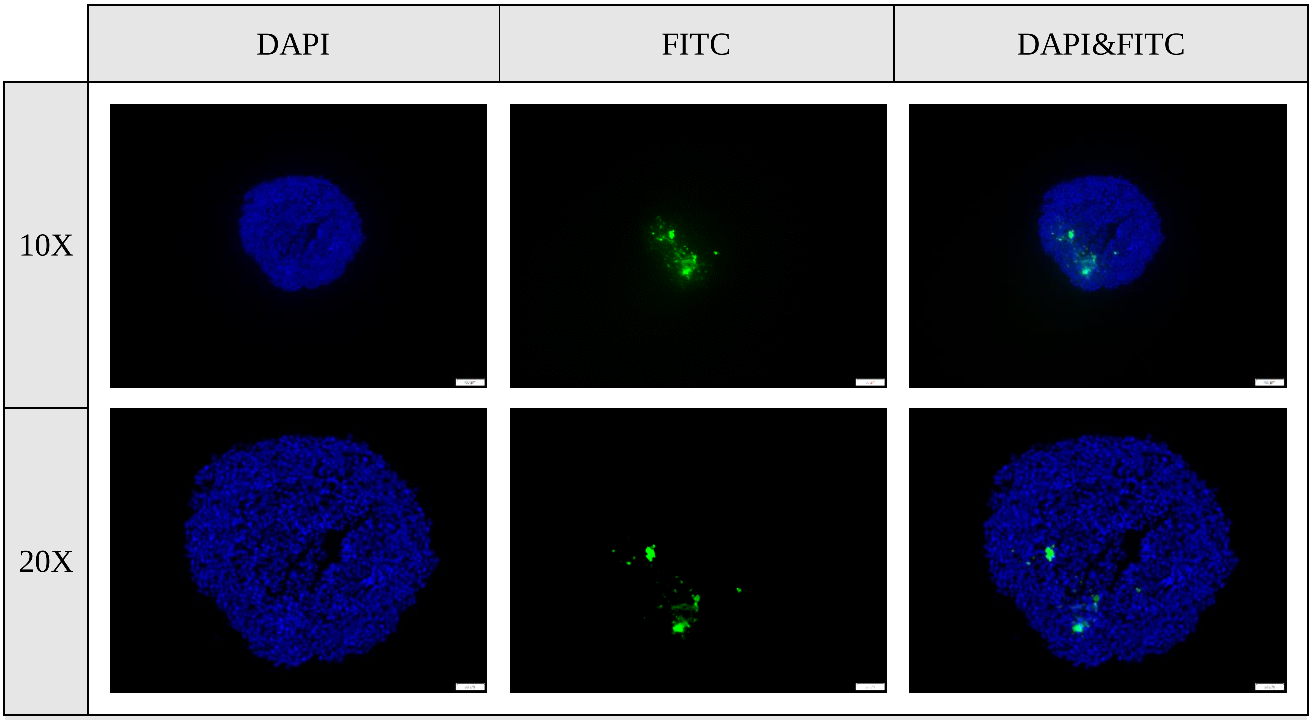

**Figure 33.** Fluorescence microscopy images of archaea’s co-culture in CT26-Luc derived spheroid for 168 hours. On day 7 from seeding the spheroid, it was inoculated with AF488-labeled archaea (27µl of AF488 for each ml of archaea suspension). The spheroids were then harvested and prefixed after 168 hours from inoculation (on day 14), and then imbedded after another 24 hours (on day 15). FLM images of the middle part of spheroid’s cryosection show the blue emission of DAPI stained cells’ nuclei (left column), the emission of AF488 detected through FITC channel (middle column) and the localization of AF488-labeled archaea in almost the hypoxic center of this spheroid (DAPI and FITC merged channels on the right column). DAPI stained spheroid’s cryosection was imaged at 10X and 20X magnifications (scale bars 100µm and 50µm respectively).

In order to increase the reproducibility of these results, DAPI stained cryosections of two 5K spheroids inoculated with AF labeled archaea were imaged to show the localization of archaea on the surface –and nearly toward the inside- of spheroids inoculated with archaea for 24h (figure 34) and the localization of AF labeled archaea on the surface of DAPI stained cryosections of another two 10K spheroids inoculated with archaea for 24h (figure 35). Besides, the tendency of AF labeled archaea to move toward the center was clearly visible in the second, third and fourth spheroids' middle parts in figure 36, after inoculating them with AF labeled archaea for 120h, as well as, in figures (38-41). Through further inoculating the spheroids with AF labeled archaea for 168h, the archaea were able to move more toward the inside of these spheroids and reach the hypoxic center, especially in the first, second and fourth spheroids from figure 37, also in the spheroids represented in figures (42 and 43).

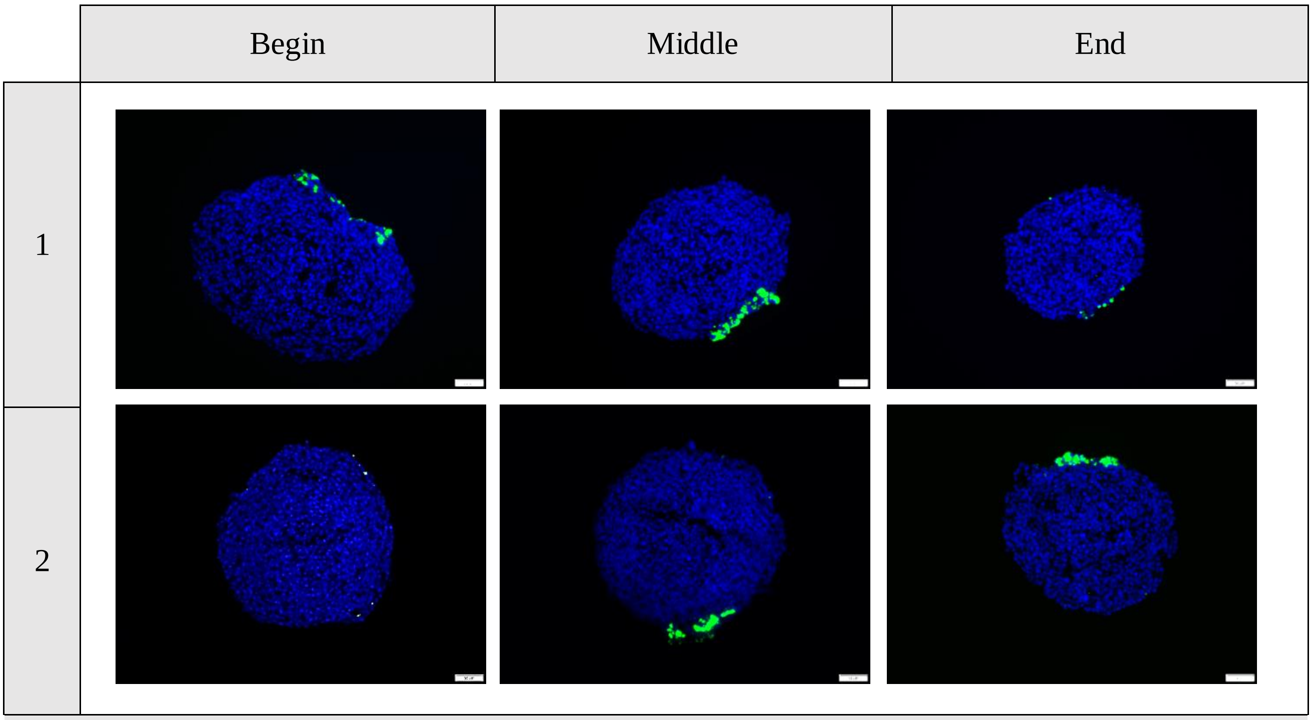

**Figure 34.** Fluorescence microscopy images represent DAPI and FITC merged channels, at 20X magnification (scale bar 50µm), for the beginning (left column), middle (middle column) and end cryosections (right column) of two 5K CT26-Luc derived spheroids, inoculated with AF488-labeled archaea for 24h, illustrate the localization of anaerobic archaea on the surface –and nearly toward the inside- of the middle cryosections and different localizations on other parts.

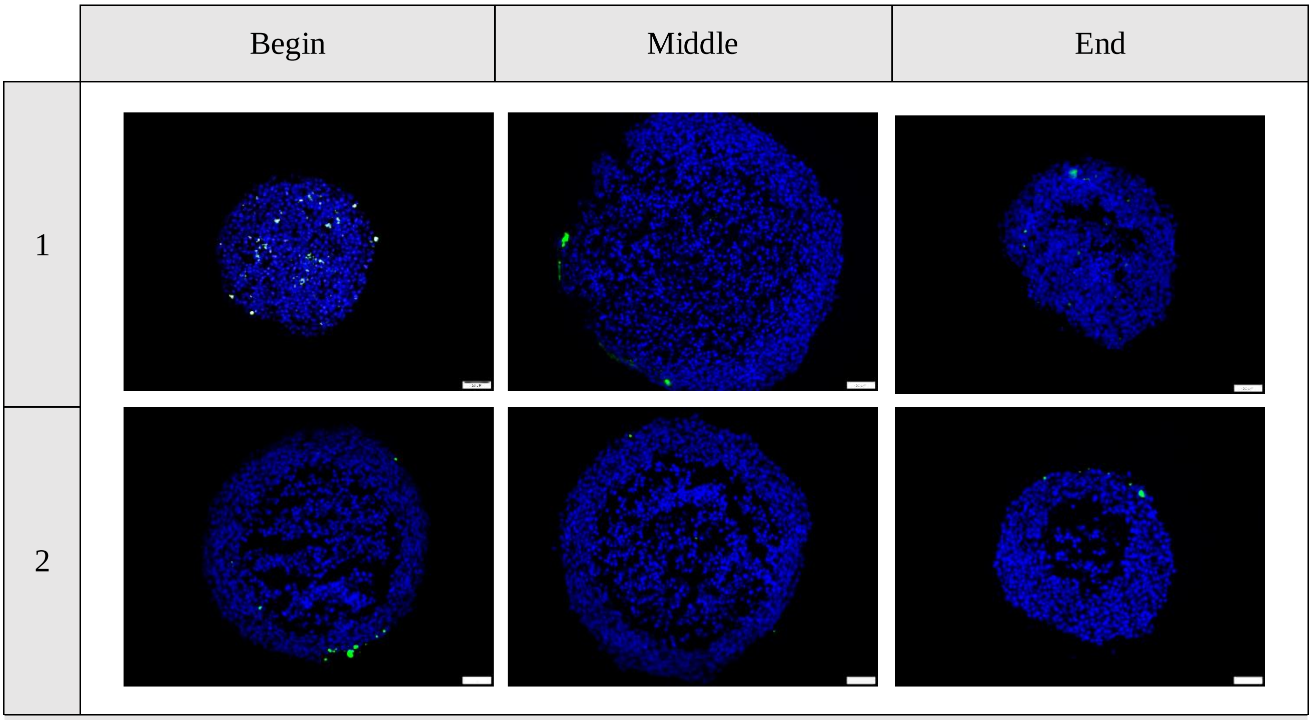

**Figure 35.** Fluorescence microscopy images represent DAPI and FITC merged channels, at 20X magnification (scale bar 50μm), for the beginning (left column), middle (middle column) and end cryosections (right column) of two 10K CT26-Luc derived spheroids inoculated with AF488- labeled archaea for 24h, illustrate the localization of anaerobic archaea on the surface of the middle cryosections and different localizations on other parts.

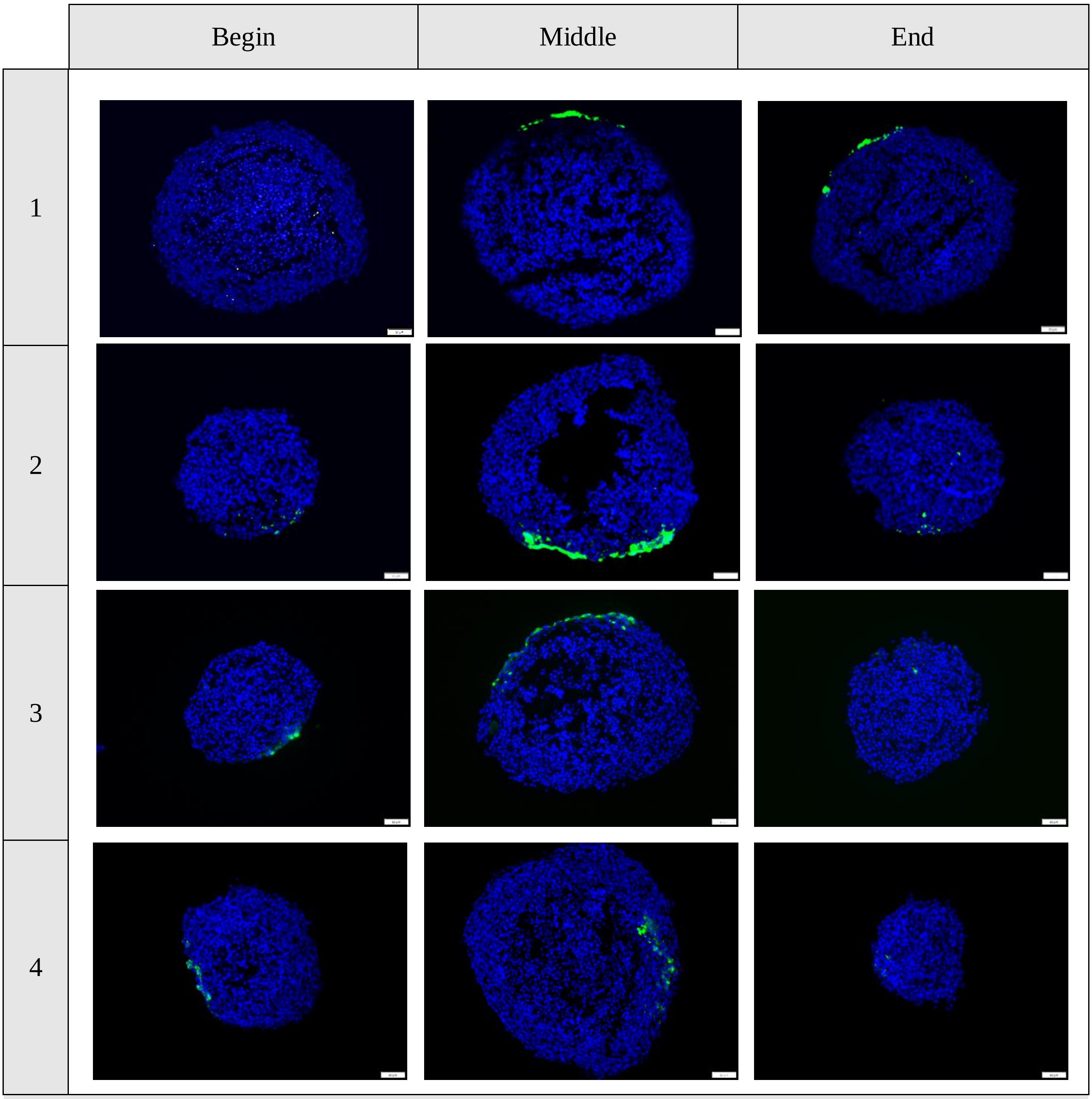

**Figure 36.** Fluorescence microscopy images represent DAPI and FITC merged channels, at 20X magnification (scale bar 50μm), for the beginning (left column), middle (middle column) and end cryosections (right column) of four CT26-Luc derived spheroids inoculated with AF488-labeled archaea for 120h, illustrate the tendency of anaerobic archaea to move toward the hypoxic center of the middle cryosections and different localizations on other parts.

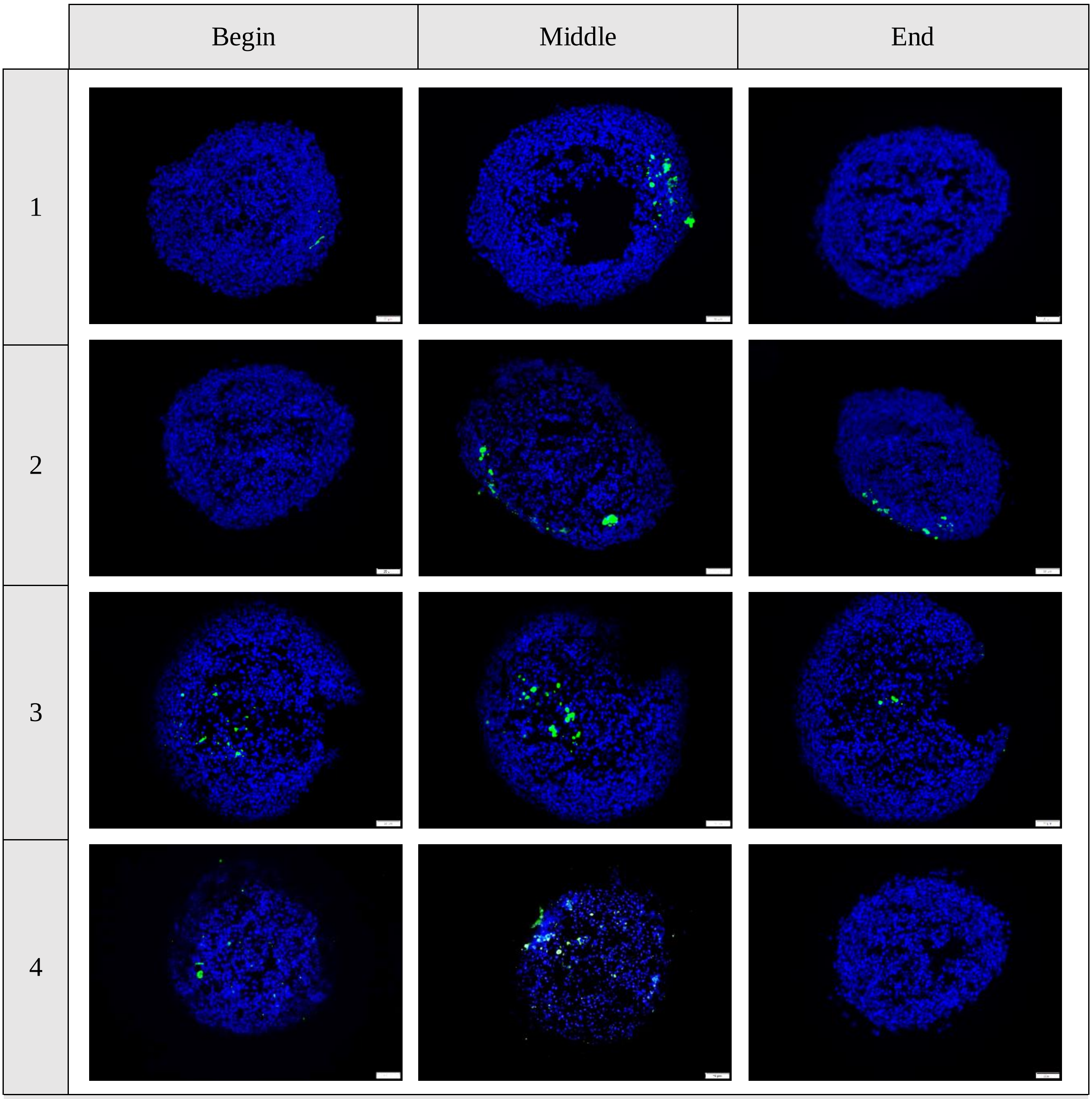

**Figure 37.** Fluorescence microscopy images represent DAPI and FITC merged channels, at 20X magnification (scale bar 50μm), for the beginning (left column), middle (middle column) and end cryosections (right column) of four CT26-Luc derived spheroids inoculated with AF488- labeled archaea for 168h, illustrate the tendency of anaerobic archaea to reach the hypoxic center of the middle cryosections and different localizations on other parts.

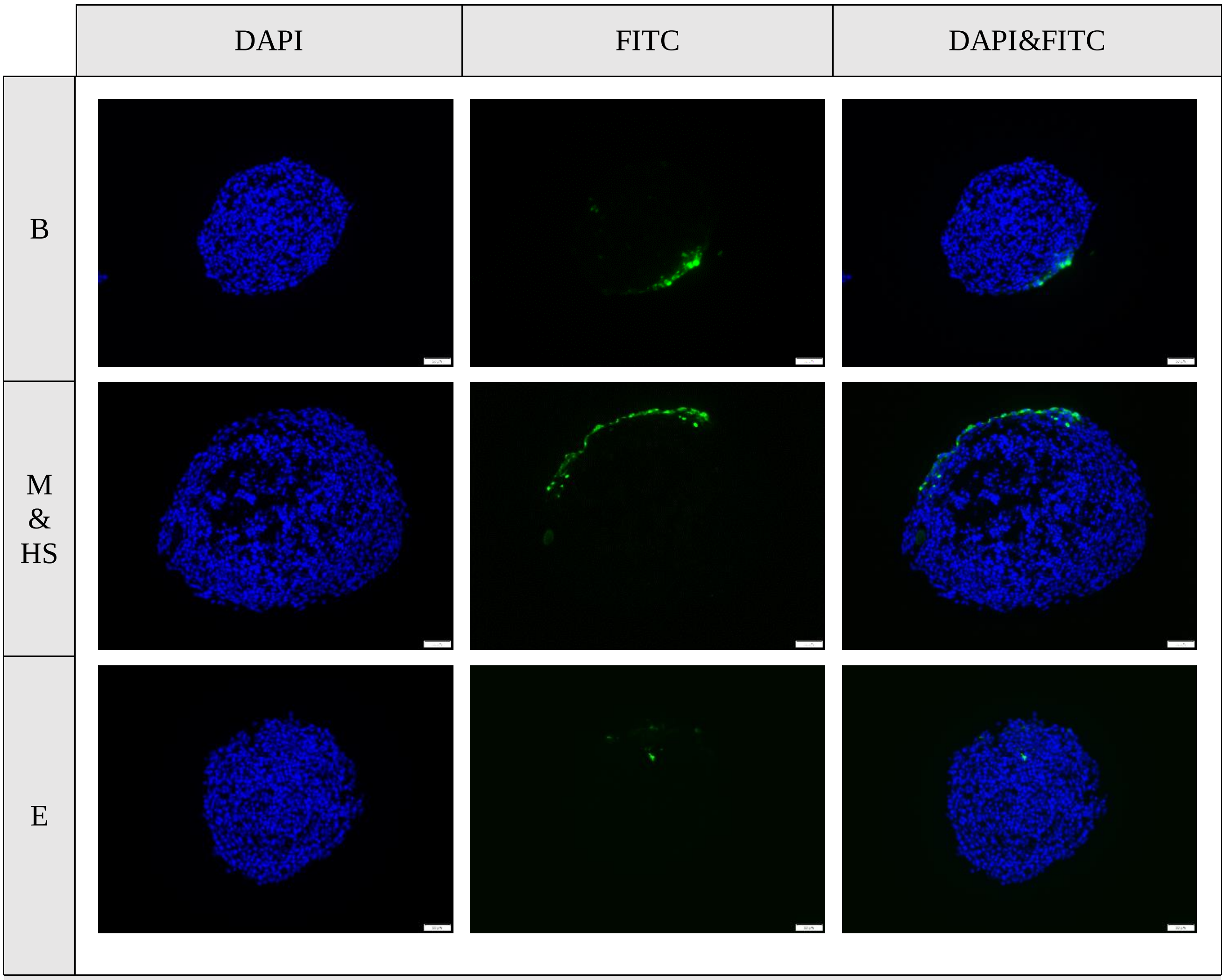

**Figure 38.** Fluorescence microscopy images of the beginning (first row), middle (second row) and end parts (third row) of a DAPI stained CT26-Luc derived spheroid (DAPI channel) inoculated with AF488-labeled archaea (FITC channel) for 120 hours. FLM images illustrate the tendency of archaea to move toward the hypoxic center in the middle part of this spheroid (DAPI and FITC merged channels), which also represent the part of spheroid with the highest signal, at 20X magnification (scale bar 50µm).

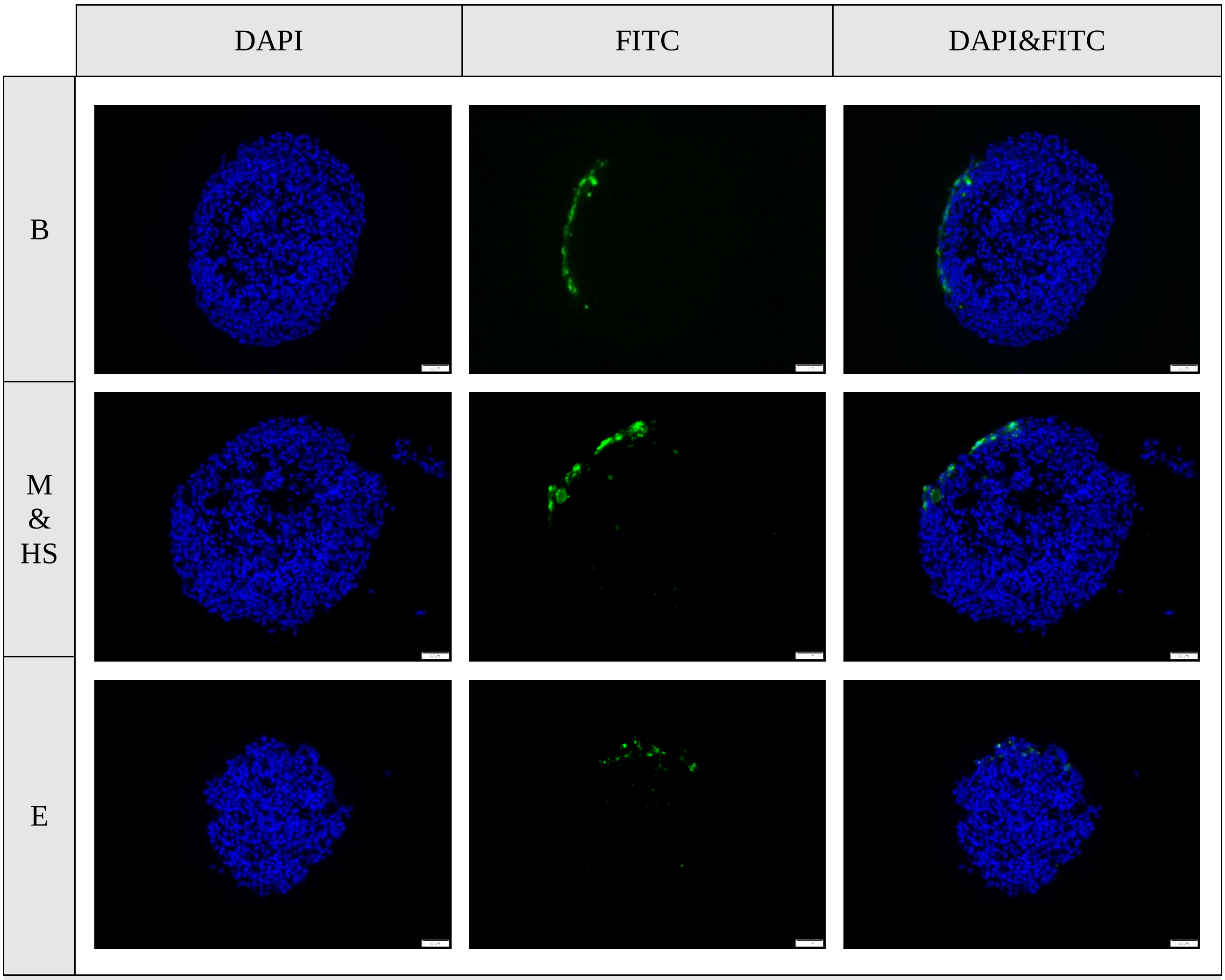

**Figure 39.** Fluorescence microscopy images of the beginning (first row), middle (second row) and end parts (third row) of another DAPI stained CT26-Luc derived spheroid (DAPI channel) inoculated with AF488-labeled archaea (FITC channel) for 120 hours. FLM images illustrate the tendency of archaea to move toward the hypoxic center in the middle part of this spheroid (DAPI and FITC merged channels), which also represent the part of spheroid with the highest signal, at 20X magnification (scale bar 50µm).

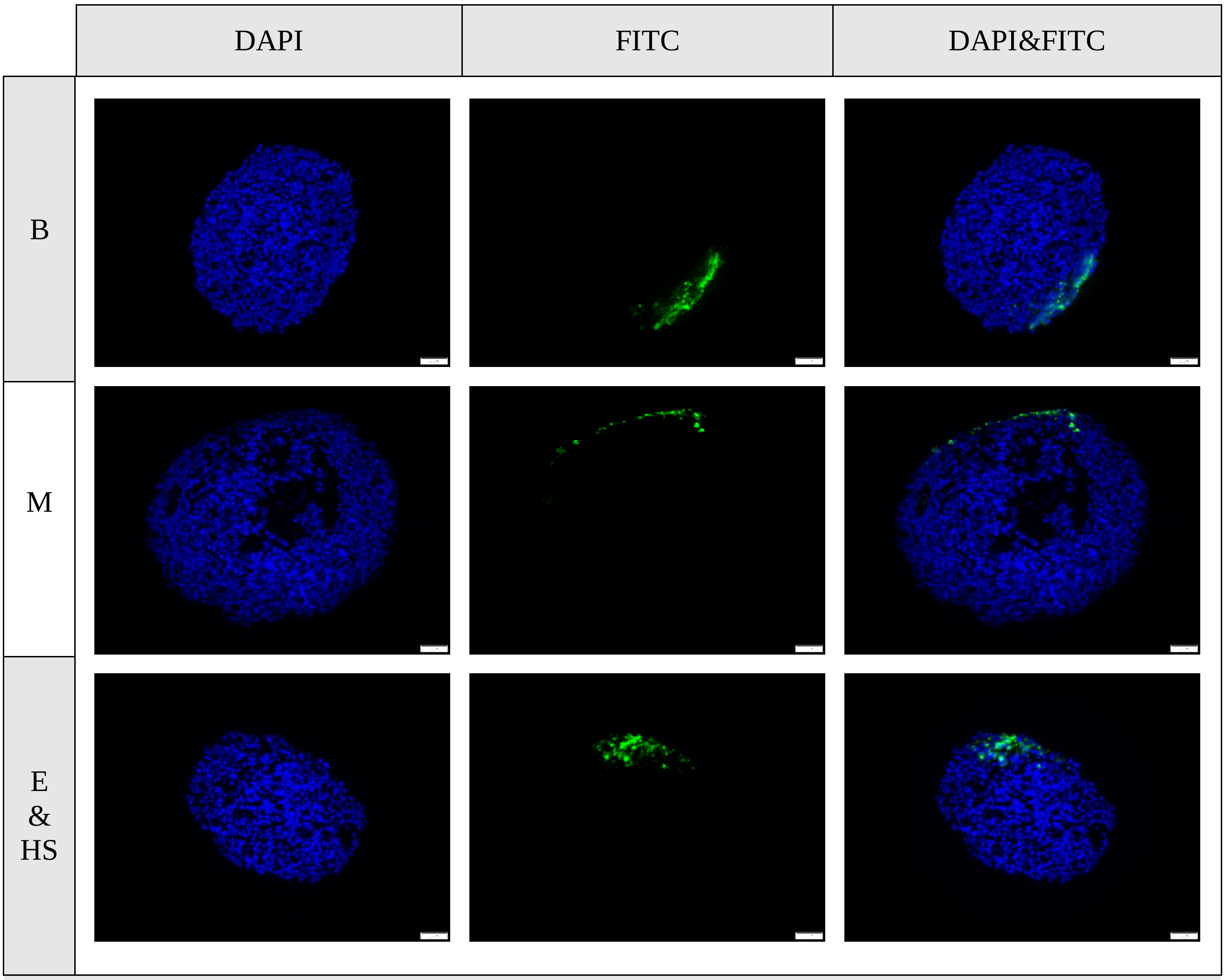

**Figure 40.** Fluorescence microscopy images of the beginning (first row), middle (second row) and end parts (third row) of another DAPI stained CT26-Luc derived spheroid (DAPI channel) inoculated with AF488-labeled archaea (FITC channel) for 120 hours. FLM images illustrate the tendency of archaea to move toward the hypoxic center in the middle part of this spheroid (DAPI and FITC merged channels), which also represent the part of spheroid with the highest signal, at 20X magnification (scale bar 50μm).

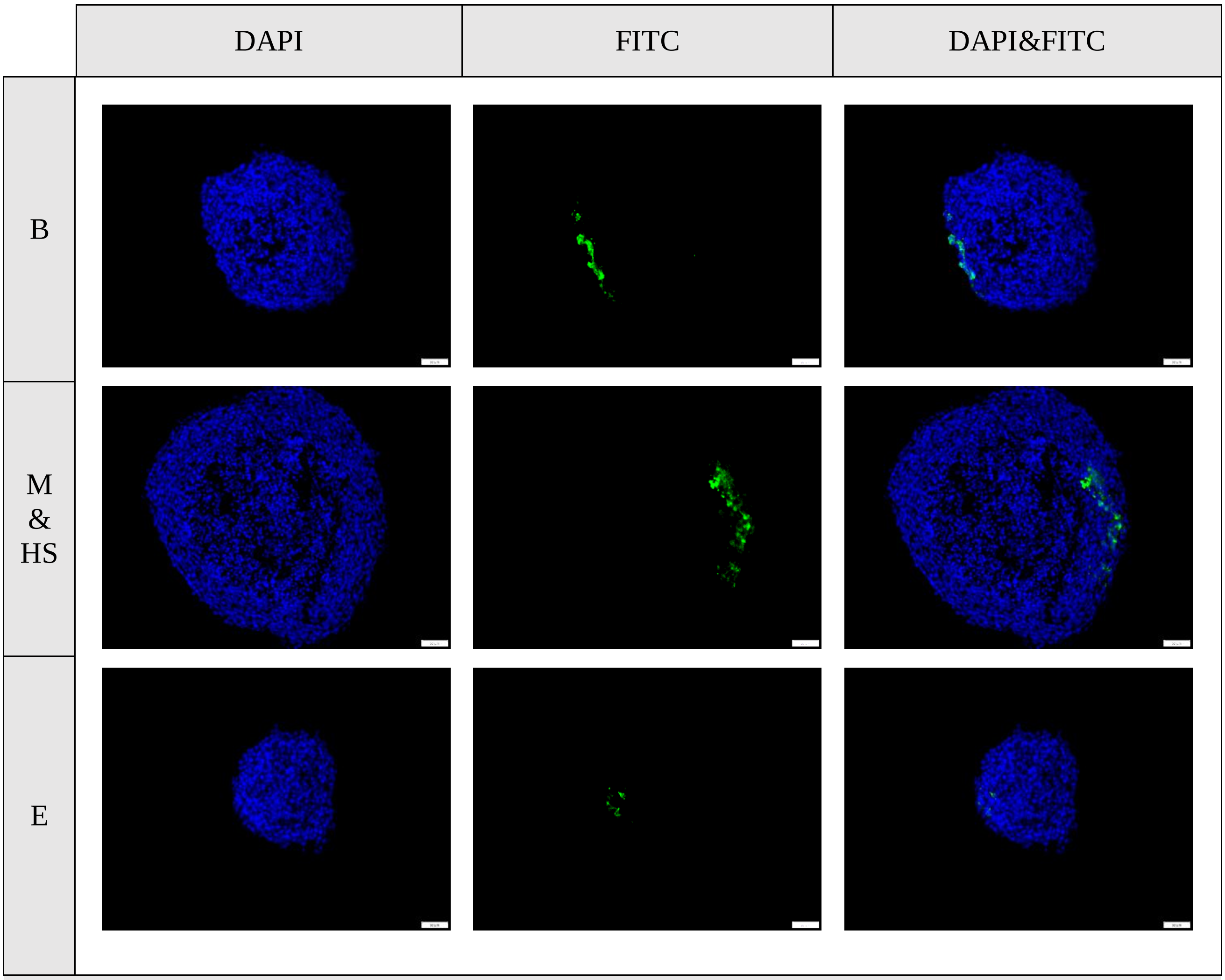

**Figure 41.** Fluorescence microscopy images of the beginning (first row), middle (second row) and end parts (third row) of another DAPI stained CT26-Luc derived spheroid (DAPI channel) inoculated with AF488-labeled archaea (FITC channel) for 120 hours. FLM images illustrate the tendency of archaea to move toward the hypoxic center in the middle part of this spheroid (DAPI and FITC merged channels), which also represent the part of spheroid with the highest signal, at 20X magnification (scale bar 50µm).

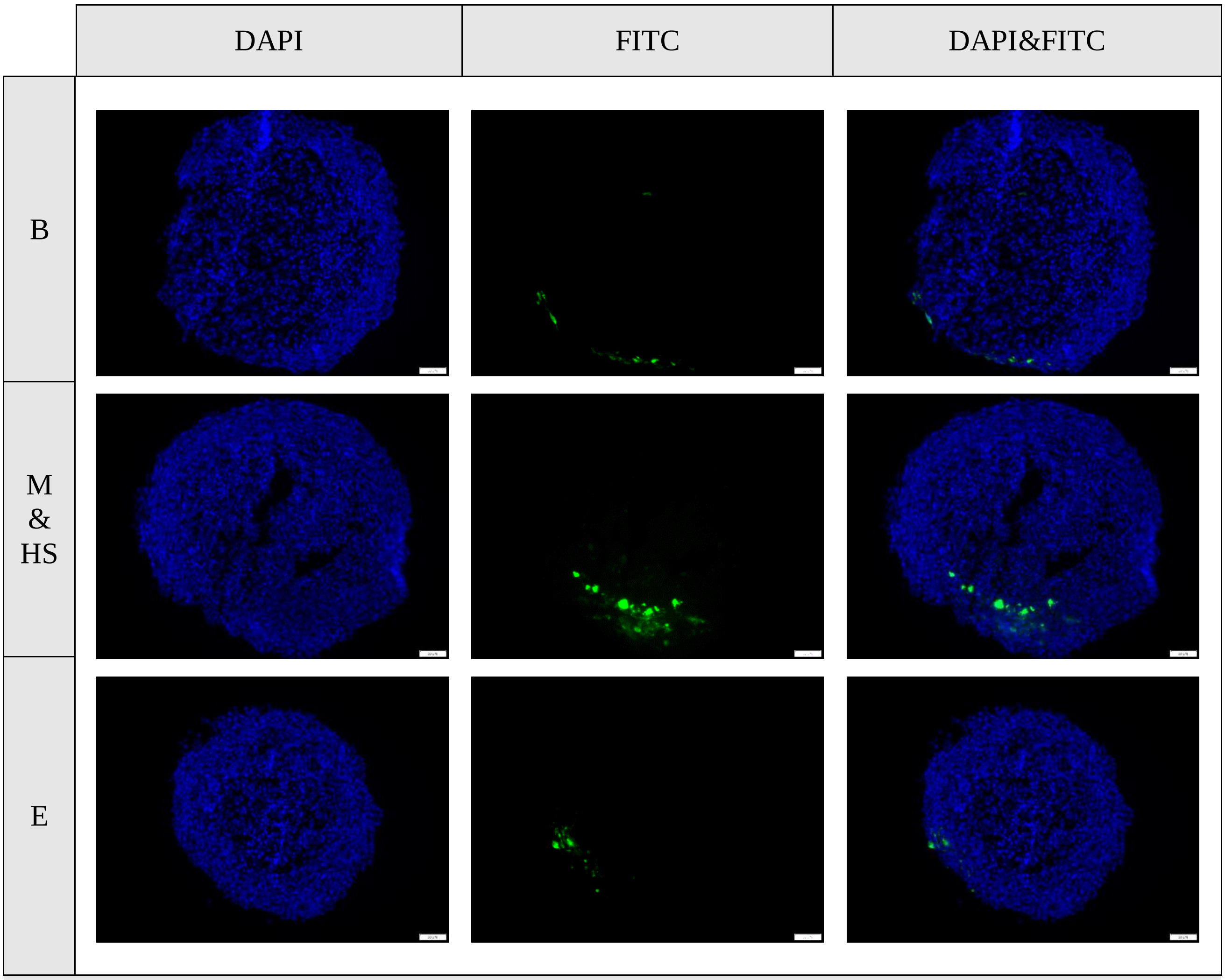

**Figure 42.** Fluorescence microscopy images of the beginning (first row), middle (second row) and end parts (third row) of a DAPI stained CT26-Luc derived spheroid (DAPI channel) inoculated with AF488-labeled archaea (FITC channel) for 168 hours. FLM images illustrate the localization of archaea in almost the hypoxic center from the middle part of this spheroid (DAPI and FITC merged channels), which also represent the part of spheroid with the highest signal, at 20X magnification (scale bar 50μm).

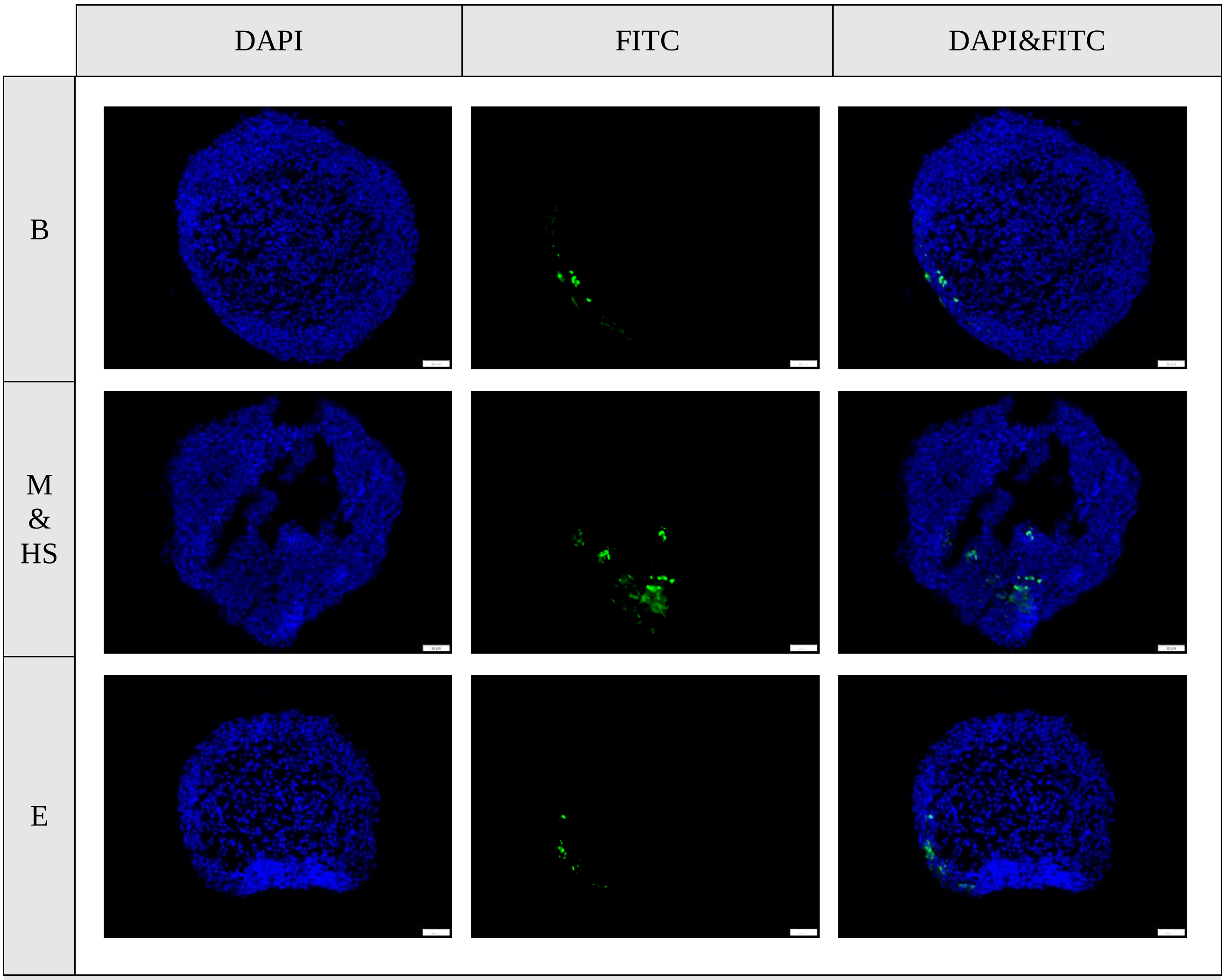

**Figure 43.** Fluorescence microscopy images of the beginning (first row), middle (second row) and end parts (third row) of another DAPI stained CT26-Luc derived spheroid (DAPI channel) inoculated with AF488-labeled archaea (FITC channel) for 168 hours. FLM images illustrate the localization of archaea in almost the hypoxic center from the middle part of this spheroid (DAPI and FITC merged channels), which also represent the part of spheroid with the highest signal, at 20X magnification (scale bar 50μm).

## Discussion

Bacterial ghost's project, which is the first project in this thesis, was firstly an ongoing work for Nadine's thesis, by which 2D fluorescence imaging for some organs, taken out from tumor bearing mice 24 hours after injecting AF750 labeled BGs, showed positive signals regarding the localization of the injected BGs in these organs. In order to confirm the presence of BGs, these organs were cryosectioned and INP immunofluorescence stained. However, INP immunofluorescent imaging of these organs' cryosections illustrated almost no positive signals but just high level of background, which raised the possibility that BGs could be degraded through the host's immune system after 24 hours from injecting them. In order to confirm the tumor association of BGs in the organs taken out from tumor bearing mice after two hours from injecting BGs, the experiment was repeated in the Institute of Cancer Research, and the organs of these mice were taken out after two hours from intraperitoneally injecting AF750 labeled BGs and embedded immediately in pre-labeled cryomolds filled with Tissue Tek® O.C.T™ Compound, without being imaged. 2D fluorescence imaging was essential on this step, in order to initially determine the biodistribution of BGs, which could be later confirmed using fluorescent microscopy techniques. Although there were no evidence on the specific localization of BGs, AF750 labeled BGs were found to be associated with the pancreas and pancreatic tumor in three mice treated with BGs, after INP immunofluorescence imaging of the stained organs' cryosections. The conformation of the results was based on the complete overlapping between Cy7 (which detects AF750 labeled BGs) and FITC (observes firstly the areas where Anti-rabbit-IgG-FITC-antibodies bind, mainly to primary antibodies bound to bacterial Ice Nucleation Protein) channels especially at 10X magnification and exposure time 1.5-2 s. However, INP immunofluorescence staining was not always optimal, as the mice were not under low fluorescent diet and the primary antibodies used to stain the organs' cryosections were polyclonal sera and not monoclonal sera, which led sometimes to nonspecific binding of antibodies, and in turn, increased the background in some tissue sections.

As a result, the existence of AF750 labeled BGs was found to be highly associated with the pancreas and pancreatic tumor in tumor bearing mice after 2 hours from intraperitoneally injecting them, as they imaged at 60X magnification to be almost intact in these organs. However, the results obtained from imaging the INP immunofluorescence stained cryosections of organs taken out after 24 hours from injecting BGs showed almost no positive signals. That is why it is ideal to repeat the experiment, with respect to the previous points, and taking out the mice organs after 4 and 6 hours from injecting BGs, in order to determine the time needed by the host's immune system to degrade the injected BGs.

Archaea infiltration project aimed to study the *in vivo* localization of the nonpathogenic, strictly anaerobic archaea, Methanococcus maripaludis S0001, in 3D MCTS from CT26-Luc cells, which resemble the properties of real tumors and could in turn give a prediction to the in vivo behavior of these archaea in cancerous tissues. Archaea were labeled with AF488, and the spheroids were inoculated with these archaea for 24, 120 and 168 hours. Fluorescent imaging for the DAPI stained spheroids' cryosections illustrated the localization of AF labeled archaea on the surface of spheroids inoculated with archaea for 24h, and the tendency of archaea to move toward the center after 120 hours from inoculating the spheroids. Finally, DAPI and FITC merged channels for the cryosections of spheroids inoculated with AF labeled archaea for 168 hours were a proof on the localization of anaerobic archaea in the hypoxic centers of these spheroids, which could predict in turn their selectivity of these microorganisms for in vivo targeting the hypoxic centers of cancerous tissues. As our results were based on imaging the spheroids' cryosections at 10X and 20X magnifications, further fluorescent imaging for the middle parts of these spheroids at 40X and 60X magnifications might better illustrate their shape and localization in spheroids' hypoxic centers, and studies on the viability of these archaea inside these hypoxic areas might be essential to support their clinical use in cancer treatment.

## References

Aranda, F.; Bloy, N.; Pesquet, J.; Petit, B.; Chaba, K.; Sauvat, A.; Kepp, O.; Khadra, N.; Enot, D.; Pfirschke, C.; et al. Immune-dependent antineoplastic effects of cisplatin plus pyridoxine in non-small-cell lung cancer. Oncogene 2015, 34, 3053–3062.

Aso, Y.; Akazan, H. Prophylactic effect of a Lactobacillus casei preparation on the recurrence of superficial bladder cancer. BLP Study Group. Urol. Int. 1992, 49, 125–129.

Bang C, Vierbuchen T, GutsmannT, Heine H, SchmitzRA. Immunogenicproperties of the human gut-associated archaeon Methanomassiliicoccus luminyensis and its susceptibility to antimicrobial peptides. 2017; PLoS ONE 12(10): e0185919

Bang C, Weidenbach K, Gutsmann T, Heine H, Schmitz R. The Intestinal Archaea Methanosphaera stadtmanae and Methanobrevibacter smithii Activate Human Dendritic Cells. 2014; PLOS ONE 9: e99411.

Basuki JS, Duong HTT, Macmillan A, Erlich RB, Esser L, Akerfeldt MC, Whan RM, Kavallaris M, Boyer C, Davis TP. Using fluorescence lifetime imaging microscopy to monitor theranostic nanoparticle uptake and intracellular doxorubicin release, ACS Nano. 2013;7:10175–10189.

Bhang, H.E.; Ruddy, D.A.; Krishnamurthy Radhakrishna, V.; Caushi, J.X.; Zhao, R.; Hims, M.M.; Singh, A.P.; Kao, I.; Rakiec, D.; Shaw, P.; et al. Studying clonal dynamics in response to cancer therapy using high-complexity barcoding. Nat. Med. 2015, 21, 440–448.

Bhatt, A.P.; Redinbo, M.R.; Bultman, S.J. The role of the microbiome in cancer development and therapy. CA Cancer J. Clin. 2017, 67, 326–344.

Blais-Lecours P, Duchaine C, Taillefer M, Tremblay C, Veillette M, et al. Immunogenic properties of archaeal species found in bioaerosols. 2011; PLOS ONE 6: e23326–e23326.

Blais-Lecours P, Marsolais D, Cormier Y, Berberi M, Hache C, et al. Increased Prevalence of Methanosphaera stadtmanae in Inflammatory Bowel Diseases. 2014; PLOS ONE 9: e87734.

Brugere JF, Borrel G, Gaci N, Tottey W, O' Toole PW, et al. Archaebiotics: proposed therapeutic use of archaea to prevent trimethylaminuria and cardiovascular disease. Gut Microbes. 2014;5:5–10.

Buckley KJ, Hayashi M. Lytic activity localized to membrane-spanning region of phi X174 E protein. Mol Gen Genet. 1986;204:120–5.

Carding, S.; Verbeke, K.; Vipond, D.T.; Corfe, B.M.; Owen, L.J. Dysbiosis of the gut microbiota in disease. Microb. Ecol. Health Dis. 2015, 26, 26191.

Chang CW, Lai YS, Westin E, Khodadadi-Jamayran A, Pawlik KM, Lamb LS Jr, Goldman FD, Townes TM. Modeling human severe combined immunodeficiency and correction by CRISPR/Cas9-enhanced gene targeting. Cell Rep. 2015;12:1668–1677

Chen MCW, Gupta M, Cheung KC. Alginate-based microfluidic system for tumor spheroid formation and anticancer agent screening, Biomed. Microdevices. 2010;12:647–654.

Conway de Macario E, König H, Macario AJ, Kandler O. Six antigenic determinants in the surface layer of the archaebacterium Methanococcus vannielii revealed by monoclonal antibodies. The Journal of Immunology. 1984;132: 883–887. 2

Conway de Macario E, Macario AJL. Methanogenic archaea in health and disease: a novel paradigm of microbial pathogenesis. International Journal of Medical Microbiology. 2009;299: 99–108.

Dagogo-Jack, I.; Shaw, A.T. Tumour heterogeneity and resistance to cancer therapies. Nat. Rev. Clin. Oncol. 2018, 15, 81–94.

DesRochers TM, Palma E, Kaplan DL. Tissue-engineered kidney disease models, Adv. Drug Deliv. Rev. 2014;69–80.

Diaz LA, Cheong I, Foss CA, Zhang X, Peters BA, Agrawal N, Bettegowda C, Karim B, Liu G, Khan K, Huang X, Kohli M, Dang LH, Hwang P, Vogelstein A, Garrett-Mayer E, Kobrin B, Pomper M, Zhou S, Kinzler KW, Vogelstein B, Huso DL. Pharmacologic and toxicologic evaluation of C. novyi-NT spores. Toxicol Sci. 2005;88:562–75.

Dridi B, Fardeau ML, Ollivier B, Raoult D, Drancourt M. Methanomassiliicoccus luminyensis gen. nov., sp. nov., a methanogenic archaeon isolated from human faeces. International Journal of Systematic and Evolutionary Microbiology. 2012;62: 1902–1907.

Dridi B, Henry M, El Khechine A, Raoult D, Drancourt M. High prevalence of Methanobrevibacter smithii and Methanosphaera stadtmanae detected in the human gut using an improved DNA detection protocol. 2009; PLOS ONE 4: e7063.

Dürr UHN, Sudheendra US, Ramamoorthy A. LL-37, the only human member of the cathelicidin family of antimicrobial peptides. Biochimica et Biophysica Acta. 2006;1758: 1408–1425.

Dzutsev A, Badger JH, Perez-Chanona E, Roy S, Salcedo R, Smith CK,Trinchieri G. Microbes and cancer. Annu Rev Immunol. 2017;35:199–228.

Eko FO, Schukovskaya T, Lotzmanova EY, Firstova VV, Emalyanova NV, Klueva SN, et al. Evaluation of the protective efficacy of Vibrio cholerae ghost (VCG) candidate vaccines in rabbits. Vaccine. 2003;21:3663–74.

Eko FO, Witte A, Huter V, Kuen B, Fürst-Ladani S, Haslberger A, et al. New strategies for combination vaccines based on the extended recombinant bacterial ghost system. Vaccine. 1999;17:1643–9.

Felgner, S.; Kocijancic, D.; Frahm, M.; Weiss, S. Bacteria in Cancer Therapy: Renaissance of an Old Concept. Int. J. Microbiol. 2016, 2016, 8451728.

Felnerova D, Kudela P, Bizik J, Haslberger A, Hensel A, Saalmuller A, et al. T cell-specific immune response induced by bacterial ghosts. Med Sci Monit. 2004;10:BR362–70.

Fessler, J.L.; Gajewski, T.F. The Microbiota: A New Variable Impacting Cancer Treatment Outcomes. Clin. Cancer Res. 2017, 23, 3229–3231.

Fineran PC, Dy RL. Gene regulation by engineered CRISPR-Cas systems. Curr Opin Microbiol. 2014;18:83–89

Fitzgerald KA, Malhotra M, Curtin CM, O’Brien FJ, O’Driscoll CM. Life in 3D is never flat: 3D models to optimise drug delivery, J. Control. Release. 2015;215: 39–54.

Fuge O, Vasdev N, Allchorne P, Green JS. Immunotherapy for bladdercancer. Res Rep Urol. 2015;7:65–79.

Fulbright, L.E.; Ellermann, M.; Arthur, J.C. The microbiome and the hallmarks of cancer. PLoSPathog. 2017, 13, e1006480.

Goodman TT, Ng CP, Pun SH. 3-D tissue culture systems for the evaluation and optimization of nanoparticle-based drug carriers, Bioconjug. Chem. 2008;19:1951–1959.

Goodrich JK, Waters JL, Poole AC, Sutter JL, Koren O, et al. Human genetics shape the gut microbiome.Cell. 2014;159:789–799.

Gordon S. Pattern recognition receptors: doubling up for the innate immune response. Cell. 2002; 111 (7):927–30.

Griffith LG, Swartz MA. Capturing complex 3D tissue physiology in vitro, Nat. Rev. Mol. Cell Biol. 2006;7:211–224.

Gröger M, Holnthoner W, Maurer D, Lechleitner S, Wolff K, Mayr BB, et al. Dermal microvascular endothelial cells express the 180-kDa macrophage mannose receptor in situ and in vitro. J Immunol. 2000;165:5428–34.

Groza D, Gehrig S, Kudela P, et al. Bacterial ghosts as adjuvant to oxaliplatin chemotherapy in colorectal carcinomatosis. Oncoimmunology. 2018;7(5):e1424676.

Hajam I, Dar P, Won G, Lee JH. Bacterial ghosts as adjuvants: Mechanisms and potential. Vet Res. 2017; 48: 37.

Han C, Takayama S, Park J. Formation and manipulation of cell spheroids using a density adjusted PEG/DEX aqueous two phase system, Sci. Rep. 2015;5:1–12.

Haque U, Rahman A, Haque A, Sarker AK, Islam A. Antimicrobial and anticancer activities of Ethyl acetate extract of co culture of Streptomyces sp ANAM-5 and AIAH-10 isolated from Mangrove forest of Sundarbans. Bangladesh. J. Appl. Pharm. Sci. 2016;6:51–5.

He H, Li Y, Jia XR, Du J, Ying X, Lu XL, Lou JN, Wei Y. PEGylated Poly (amidoamine) dendrimer-based dual-targeting carrier for treating brain tumors, Biomaterials. 2011;32:478–487.

Hegazy GE, Abu-Serie MM, Abo-Elela GM, et al. In vitro dual (anticancer and antiviral) activity of the carotenoids produced by haloalkaliphilic archaeon Natrialba sp. M6. Sci Rep. 2020;10(1):5986.

Heldin CH, Rubin K, Pietras K, Östman A. High interstitial fluid pressure — an obstacle in cancer therapy, Nat. Rev. Cancer 4. 2004;4:806–813.

Hirschhaeuser F, Menne H, Dittfeld C, West J, Mueller-Klieser W, KunzSchughart LA. Multicellular tumor spheroids: an underestimated tool is catching up again. J Biotechnol. 2010;148:3–15.

Hou J, Cui HL. In-vitro antioxidant, antihemolytic, and anticancer activity of the carotenoids from Halophilic archaea. Curr. Microbiol. 2018;75:266–71.

Hsiao AY, Tung YC, Kuo CH, Mosadegh B, Bedenis R, Pienta KJ, Takayama S. Micro-ring structures stabilize microdroplets to enable long term spheroid culture in 384 hanging drop array plates. Biomed. Microdevices. 2012;14:313–323.

Hu B, Kou L, Li C, Zhu L-P, Fan Y-R, Wu Z-W, Wang J-J, Xu G-X. Bifidobacterium longum as a delivery system of TRAIL and endostatin cooperates with chemotherapeutic drugs to inhibit hypoxic tumor growth. Cancer Gene Ther. 2009;16:655–63.

Huang K, Boerhan R, Liu C, Jiang G. Nanoparticles Penetrate Into the Multicellular Spheroid-on-Chip: Effect of Surface Charge, Protein Corona and Exterior flow, J. Accepted (2017), http://dx.doi.org/10.1021/acs.molpharmaceut. 7b00726.

Huter V, Szostak MP, Gampfer J, Prethaler S, Wanner G, Gabor F, et al. Bacterial ghosts as drug carrier and targeting vehicles. J Control Release. 1999;61:51–63.

Hutmacher DW, Horch RE, Loessner D, Rizzi S, Sieh S, Reichert JC, Clements JA, Beier JP, Arkudas A, Bleiziffer O, Kneser U, Translating tissue engineering technology platforms into cancer research, J. Cell. Mol. Med. 2009;13:1417–1427.

Iida N, Dzutsev A, Stewart CA, Smith L, Bouladoux N, Weingarten RA, Molina DA, Salcedo R, Back T, Cramer S, et al. Commensal bacteria control cancer response to therapy by modulating the tumor microenvironment. Science. 2013;342:967– 70.

Ivascu A, Kubbies M. Rapid generation of single-tumor spheroids for high throughput cell function and toxicity analysis, J. Biomol. Screen. 2006;11:922–932.

Jan, G.; Belzacq, A.S.; Haouzi, D.; Rouault, A.; Métivier, D.; Kroemer, G.; Brenner, C. Propionibacteria induce apoptosis of colorectal carcinoma cells via short-chain fatty acids acting on mitochondria. CellDeathDiffer. 2002, 9, 179–188.

Jayakumar S, Kunwar A, Sandur SK, Pandey BN, Chaubey RC. Differential response of DU145 and PC3 prostate cancer cells to ionizing radiation: role of reactive oxygen species, GSH and Nrf2 in radiosensitivity. Biochim. Biophys. Acta . 2014;1840:485–94.

Jechlinger W, Haller C, Resch S, Hofmann A, Szostak MP, Lubitz W. Comparative immunogenicity of the hepatitis B virus core 149 antigen displayed on the inner and outer membrane of bacterial ghosts. Vaccine. 2005;23:3609–17.

Jechlinger W, Szostak MP, Lubitz W. Cold-sensitive E-lysis systems. Gene.1998;218:1–7.

Jiang S-N, Phan TX, Nam T-K, Nguyen VH, Kim H-S, Bom H-S, Choy HE, Hong Y, Min J-J. Inhibition of tumor growth and metastasis by a combination of Escherichia coli-mediated cytolytic therapy and radiotherapy. Mol Ther J Am Soc Gene Ther. 2010;18:635–42.

Jones WJ, Paynter MJB, Gupta R. Characterization of Methanococcus maripaludis sp. nov., a new methanogen isolated from salt marsh sediment. Arch Microbiol. 1983;135:91–7.

Kang HY, Curtiss R., 3rd Immune responses dependent on antigen location in recombinant attenuated Salmonella typhimurium vaccines following oral immunization. FEMS Immunol Med Microbiol. 2003;37:99–104.

Khailova, L.; Baird, C.H.; Rush, A.A.; Barnes, C.; Wischmeyer, P.E. Lactobacillus rhamnosus GG treatment improves intestinal permeability and modulates inflammatory response and homeostasis of spleen and colon in experimental model of Pseudomonas aeruginosa pneumonia. Clin. Nutr. 2017, 36, 1549–1557.

Koeth RA, WangZ, Levison BS,Buffa JA, OrgE, et al. Intestinal microbiota metabolism of L carnitine, a nutrient in red meat, promotes atherosclerosis. NatMed. 2013;19:576–585.

König H. Prokaryotic Cell Wall Compounds. Berlin, Heidelberg: Springer Berlin Heidelberg. 2010;159–162 .

Konishi, H.; Fujiya, M.; Tanaka, H.; Ueno, N.; Moriichi, K.; Sasajima, J.; Ikuta, K.; Akutsu, H.; Tanabe, H.; Kohgo, Y. Probiotic-derived ferrichrome inhibits colon cancer progression via JNK-mediated apoptosis. Nat. Commun. 2016, 7, 12365.

Kramer, M.G.; Masner, M.; Ferreira, F.A.; Hoffman, R.M. Bacterial Therapy of Cancer: Promises, Limitations, and Insights for Future Directions. Front. Microbiol. 2018, 9, 16.

Kroemer G, Galluzzi L, Kepp O, Zitvogel L. Immunogenic cell deathin cancer therapy. Ann Rev Immunol. 2013;31:51–72.

Kudela P, Koller VJ, Lubitz W. Bacterial ghosts (BGs)—Advanced antigen and drug delivery system. Vaccine. 2010;28:5760-5767.

Kudela P, Koller VJ, Mayr UB, Nepp J, Lubitz W, Barisani-Asenbauer T. Bacterial Ghosts as antigen and drug delivery system for ocular surface diseases: Effective internalization of Bacterial Ghosts by human conjunctival epithelial cells. J Biotechnol. 2011;153:167–75.

Kudela P, Paukner S, Mayr UB, Cholujova D, Kohl G, Schwarczova Z, et al. Effective gene transfer to melanoma cells using bacterial ghosts. Cancer Lett. 2008;262:54–63.

LaBarbera DV, Reid BG, Yoo BH. The multicellular tumor spheroid model for high-throughput cancer drug discovery, Expert Opin. Drug Discovery .2012;7:819–830.

Lamichhane SP, Arya N, Kohler E, Xiang S, Christensen J, Shastri VP. Recapitulating epithelial tumor microenvironment in vitro using three dimensional tri-culture of human epithelial, endothelial, and mesenchymal cells, BMC Cancer. 2016;16:581.

Lee J, Cuddihy MJ, Cater GM, Kotov NA. Engineering liver tissue spheroids with inverted colloidal crystal scaffolds, Biomaterials. 2009;30:4687–4694.

Li Z, Fallon J, Mandeli J, Wetmur J, Woo SLC. A genetically enhanced anaerobic bacterium for oncopathic therapy of pancreatic cancer. J Natl Cancer Inst 2008; 100:1389-400..

Lin F, Lin P, Zhao D, Chen Y, Xiao L, Qin W, Li D, Chen H, Zhao B, Zou H, Zheng X. Sox2 targets cyclin E, p27 and survivin to regulate androgen-independent human prostate cancer cell proliferation and apoptosis. Cell Proliferat. 2012;45:207–16.

Liu C, Kelnar K, Liu B, Chen X, Calhoun-Davis T, Li H, Patrawala L, Yan H, Jeter C, Honorio S, Wiggins JF. The microRNA miR-34a inhibits prostate cancer stem cells and metastasis by directly repressing CD44. Nat. Med. 2011;17:211–22.

Lubitz P., Mayr U.B., Lubitz W. Applications of Bacterial Ghosts in Biomedicine. In: Guzmán C.A., Feuerstein G.Z. (eds) Pharmaceutical Biotechnology. Advances in Experimental Medicine and Biology. Springer, New York, NY. 2009; 655.

Lubitz W. Bacterial ghosts as carrier and targeting systems. Expert Opin Biol Ther. 2001;1:765–71.

Lurie-Weinberger MN, Peeri M, Gophna U. Contribution of lateral gene transfer to the gene repertoire of a gut-adapted methanogen. Genomics. 2012;99:52–58.

Lynch, S.V.; Pedersen, O. The Human Intestinal Microbiome in Health and Disease. N.Engl. J.Med. 2016, 375, 2369–2379.

Maeder ML, Gersbach CA. Genome-editing Technologies for gene and cell therapy. Mol Ther. 2016;24:430–446

Mayrhofer P, Tabrizi CA, Walcher P, Haidinger W, Jechlinger W, Lubitz W. Immobilization of plasmid DNA in bacterial ghosts. J Control Release. 2005;102:725–35.

Medina E, Guzman CA. Use of live bacterial vaccine vectors for antigen delivery: Potential and limitations. Vaccine. 2001;19:1573–80.

Mehta G, Hsiao AY, Ingram M, Luker GD, Takayama S. Opportunities and challenges for use of tumor spheroids as models to test drug delivery and efficacy, J. Control. Release.2012;164:192–204.

Melichar B, Freedman RS. Immunology of the peritoneal cavity: rele-vance for host-tumor relation. Int J Gynecol Cancer. 2002;12:3–17.

Michel D, Mohammed-Saeid W, Getson H, Roy C, Poorghorban M, Chitanda JM, Verrall R, Badea I. Evaluation of β-cyclodextrin-modified gemini surfactant-based delivery systems in melanoma models, Int. J. Nanomedicine. 2016;11:6703–6712.

Mollanoori, H., Teimourian, S. Therapeutic applications of CRISPR/Cas9 system in gene therapy. Biotechnol Lett. 2018;40: 907–914.

Nauts, H.C.; Swift, W.E.; Coley, B.L. The treatment of malignant tumors by bacterial toxins as developed by the late William B. Coley, M.D., reviewed in the light of modern research. Cancer Res. 1946, 6, 205–216.

Osswald A, Sun Z, Grimm V, et al. Three-dimensional tumor spheroids for in vitro analysis of bacteria as gene delivery vectors in tumor therapy. Microb Cell Fact. 2015;14:199

Oxley AP, Lanfranconi MP, Wurdemann D, Ott S, Schreiber S, et al. Halophilic archaea in the human intestinal mucosa. Environ Microbiol. 2010 12:2398–2410.

Parthasarathy R, Sacks PG, Harris D, Brock H, Mehta K. Interaction of liposome-associated all-trans-retinoic acid with squamous carcinoma cells, Cancer Chemother. Pharmacol. 1994;34:527–534.

Paukner S, Kudela P, Kohl G, Schlapp T, Friedrichs S, Lubitz W. DNA-loaded bacterial ghosts efficiently mediate reporter gene transfer and expression in macrophages. Mol Ther. 2005;11:215-23.

Paulos, C.M.; Wrzesinski, C.; Kaiser, A.; Hinrichs, C.S.; Chieppa, M.; Cassard, L.; Palmer, D.C.; Boni, A.; Muranski, P.; Yu, Z.; et al. Microbial translocation augments the function of adoptively transferred self/tumor-specific CD8+ T cells via TLR4 signaling. J. Clin. Investig. 2007, 117, 2197–2204.

Perche F, Patel NR, Torchilin VP. Accumulation and toxicity of antibody-targeted doxorubicin-loaded PEG-PE micelles in ovarian cancer cell spheroid model, J. Control. Release. 2012;164:95–102.

Pimente lM, Gunsalus RP, Rao SS, Zhang H. Methanogens in Human Health and Disease. Am J Gastroenterol Suppl. 2012;6:28–33.

Rea, D.; Coppola, G.; Palma, G.; Barbieri, A.; Luciano, A.; Del Prete, P.; Rossetti, S.; Berretta, M.; Facchini, G.; Perdonà, S.; et al. Microbiota effects on cancer: From risks to therapies. Oncotarget 2018, 9, 17915–17927.

Rescigno M. Intestinal dendritic cells. Advances in Immunology. 2010;107: 109–138.

Riedmann EM, Kyd JM, Cripps AW, Lubitz W. Bacterial ghosts as adjuvant particles. Expert Rev Vaccines. 2007;6:241–53.

Riehl,T.E.;Alvarado,D.;Ee,X.;Zuckerman,A.;Foster,L.;Kapoor,V.;Thotala,D.;Ciorba,M.A.;Stenson,W.F. GG protects the intestinal epithelium from radiation injury through release of lipoteichoic acid, macrophage activation and the migration of mesenchymal stem cells. Gut 2018.

Roomi MW, Ivanov V, Kalinovsky T, Niedzwiecki A, Rath M. In-vivo antitumor effect of ascorbic acid, lysine, proline and green tea extract on human prostate cancer PC-3 xenografts in nude mice: evaluation of tumor growth and immunohistochemistry. In-Vivo . 2005;19:179–83.

Rothschild, D.; Weissbrod, O.; Barkan, E.; Kurilshikov, A.; Korem, T.; Zeevi, D.; Costea, P.I.; Godneva, A.; Kalka, I.N.; Bar, N.; et al. Environment dominates over host genetics in shaping human gut microbiota. Nature 2018, 555, 210–215.

Ruan S, Cao X, Cun X, Hu G, Zhou Y, Zhang Y, Lu L, He Q, Gao H. Matrix metalloproteinase-sensitive size-shrinkable nanoparticles for deep tumor penetration and pH triggered doxorubicin release, Biomaterials. 2015;60:100–110.

Safarpour A, Ebrahimi M, Shahzadeh Fazeli SA, Amoozegar MA. Supernatant Metabolites from Halophilic Archaea to Reduce Tumorigenesis in Prostate Cancer In-vitro and In-vivo. Iran J Pharm Res. 2019;18(1):241–253.

Sagnella SM, McCarroll JA, Kavallaris M. Drug delivery: beyond active tumour targeting, Nanomed. Nanotechnol. Biol. Med. 2014;10:1131–1137.

Samuel BS, Hansen EE, Manchester JK, Coutinho PM, Henrissat B, et al. Genomic and metabolic adaptations of Methanobrevibacter smithii to the human gut. Proceedings of the National Academy of Sciences of the United States of America. 2007;104: 10643–10648.

Sandrini, S.; Aldriwesh, M.; Alruways, M.; Freestone, P. Microbial endocrinology: Host-bacteria communication within the gut microbiome. J. Endocrinol. 2015, 225, R21–R34.

Sarvari S, Seyedjafari E, Amoozgar MA, Bakhshandeh B. The effect of moderately halophilic bacteria supernatant on proliferation and apoptosis of cancer cells and mesenchymal stem cells. Cell. Mol. Biol. 2015;61:30–4.

Scanlan PD, Shanahan F, Marchesi JR. Human methanogen diversity and incidence in healthy and diseased colonic groups using mcrA gene analysis. BMC Microbiology. 2008;8: 79–79.

Schön P, Schrot G, Wanner G, Lubitz W, Witte A. Two-stage model for integration of the lysis protein E of phiX174 into the cell envelope of Escherichia coli. FEMS Microbiol Rev. 1995;17:207–212.

Sesardic D, Dobbelaer R. European union regulatory developments for new vaccine adjuvants and delivery systems. Vaccine. 2004;22:2452–6.

Shin CS, Kwak B, Han B, Park K. Development of an In Vitro 3D Tumor Model to Study Therapeutic Efficiency of an Anticancer Drug, Mol. Pharm. 2013;10:2167–2175.

Szostak MP, Mader H, Truppe M, Kamal M, Eko FO, Huter V, et al. Bacterial ghosts as multifunctional vaccine particles. Behring Inst Mitt. 1997:191–6.

Tabrizi CA, Walcher P, Mayr UB, Stiedl T, Binder M, McGrath J, et al. Bacterial ghosts-biological particles as delivery systems for antigens, nucleic acids and drugs. Curr Opin Biotechnol. 2004;15:530–7.

Takeda K, Akira S. Toll-like receptors in innate immunity. International Immunology. 2005;17: 1–14.

Tang L, Yang X, Yin Q, Cai K, Wang H, Chaudhury I, Yao C, Zhou Q, Kwon M, Hartman JA, Dobrucki IT, Dobrucki LW, Borst LB, Lezmi S, Helferich WG, Ferguson AL, Fan TM, Cheng J. Investigating the optimal size of anticancer nanomedicine, Proc. Natl. Acad. Sci. 2014;111:15344–15349.

Tangney M, Gahan CG. Editorial hot topic: bacterial vectors for gene & cell therapy. Curr Gene Ther 2010; 10:1-2.

Teimourian S, Abdollahzadeh R. Technology developments in biological tools for targeted genome surgery. Biotechnol Lett. 2015;37:29–39

Tesniere A, Schlemmer F, Boige V, Kepp O, Martins I, Ghiringhelli F,Aymeric L, Michaud M, Apetoh L, Barault L, et al. Immunogenicdeath of colon cancer cells treated with oxaliplatin. Oncogene.2010;29:482–91.

Thorsson, V.; Gibbs, D.L.; Brown, S.D.; Wolf, D.; Bortone, D.S.; Ou Yang, T.H.; Porta-Pardo, E.; Gao, G.F.; Plaisier, C.L.; Eddy, J.A.; et al. The Immune Landscape of Cancer. Immunity 2018, 48, 812–830.

Toh, H.C. Cancer immunotherapy-the end of the beginning. Chin. Clin. Oncol. 2018, 7, 12.

Trombetta ES, Ebersold M, Garrett W, Pypaert M, Mellman I. Activation of lysosomal function during dendritic cell maturation. Science. 2003;299:1400–3.

Tung YC, Hsiao AY, Allen SG, Torisawa Y, Ho M, Takayama S. High throughput 3D spheroid culture and drug testing using a 384 hanging drop array, Analyst. 2011;136:473–478.

Van Mellaert L, Barbé S, Anné J. Clostridium spores as anti-tumour agents. Trends Microbiol. 2006;14:190–6.

VanDen Brand D, Massuger LF, Brock R, Verdurmen WPR. Mimicking tumors: toward more predictive in vitro models for peptide- and protein-conjugated drugs, Bioconjug. Chem. 2017;28:846–856.

Vinci M, Gowan S, Boxall F, Patterson L, Zimmermann M, Court W, Lomas C, Mendiola M, Hardisson D, Eccles SA. Advances in establishment and analysis of three-dimensional tumor spheroid-based functional assays for target validation and drug evaluation, BMC Biol. 2012;10:29.

Walcher P, Mayr UB, Azimpour-Tabrizi C, Eko FO, Jechlinger W, Mayrhofer P, et al. Antigen discovery and delivery of subunit vaccines by nonliving bacterial ghost vectors. Expert Rev Vaccines. 2004;3:681–91.

Wei MQ, Mengesha A, Good D, Anné J. Bacterial targeted tumour therapy-dawn of a new era. Cancer Lett. 2008;259:16–27.

Wei, W.; Sun, W.; Yu, S.; Yang, Y.; Ai, L. Butyrate production from high-fiber diet protects against lymphoma tumor. Leuk. Lymphoma 2016, 57, 2401–2408.

Witte A, Wanner G, Blasi U, Halfmann G, Szostak M, Lubitz W. Endogenous transmembrane tunnel formation mediated by phi X174 lysis protein E. J Bacteriol. 1990;172:4109–14.

Witte A, Wanner G, Lubitz W, Holtje JV. Effect of phi x174 E-mediated lysis on murein composition of Escherichia coli. FEMS Microbiol Lett. 1998;164:149–57.

Wu LY, Di Carlo D, Lee LP. Microfluidic self-assembly of tumor spheroids for anticancer drug discovery. Biomed Microdevices. 2008;10:197–202.

Xu X, Sabanayagam CR, Harrington DA, Farach-Carson MC, Jia X. A hydrogel-based tumor model for the evaluation of nanoparticle-based cancer therapeutics, Biomaterial. 2014;35:3319–3330.

Young EWK, Cells, tissues, and organs on chips: challenges and opportunities for the cancer tumor microenvironment, Integr. Biol. 2013;5:1096–1109.

Yuhas JM, Li AP, Martinez AO, Ladman AJ. A simplified method for production and growth of multicellular tumor spheroids, Cancer Res. 1977;37:3639–3643

Zanoni M, Piccinini F, Arienti C, Zamagni A, Santi S, Polico R, Bevilacqua A, Tesei A. 3D tumor spheroid models for in vitro therapeutic screening: asystematic approach to enhance the biological relevance of data obtained, Sci. Rep. 2016;6:19103.

Zbar, B.; Bernstein, I.; Tanaka, T.; Rapp, H.J. Tumor immunity produced by the intradermal inoculation of living tumor cells and living Mycobacteriumbovis (strain BCG). Science 1970, 170, 1217–1218.

Zhang L, Wang Y, Xia T, Yu Q, Zhang Q, Yang Y, Cun X, Lu L, Gao H, Zhang Z, He Q. Suppression for lung metastasis by depletion of collagen I and lysyl oxidase via losartan assisted with paclitaxel-loaded pH-sensitive liposomes in breast cancer, Drug Deliv. 2016;23: 2970–2979.

Zhernakova A, Kurilshikov A, Bonder MJ, Tigchelaar EF, Schirmer M, Vatanen T, Mujagic Z, Vila AV, Falony G, Vieira-Silva S. Population-based metagenomics analysis reveals markers for gut microbiomecompositionanddiversity. Science. 2016;352(6285):565–569.

Zitvogel, L.; Daillère, R.; Roberti, M.P.; Routy, B.; Kroemer, G. Anticancer effects of the microbiome and its products. Nat. Rev. Microbiol. 2017, 15, 465–478.

Zych AO, Bajor M, Zagozdzon R. Application of genome editing techniques in immunology. Arch Immunol Ther Exp (Warsz) 2018.